5-7-2011

Serial Sectioning using Focused Ion Beam for Three Dimensional Tomographic Reconstruction of Microstructural Development in Forged Al-Ni-Y-Co alloys

Mauricio A. Gordillo
maugor@yahoo.com

Serial Sectioning using Focused Ion Beam for Three Dimensional Tomographic Reconstruction of Microstructural Development in Forged Al-Ni-Y-Co alloys

Mauricio Andres Gordillo

B.S., Florida Atlantic University, 2006

A Thesis
Submitted in Partial Fulfillment of the
Requirements for the Degree of
Master of Science
at the
University of Connecticut
2011

APPROVAL PAGE

Master of Science Thesis

Serial Sectioning using Focused Ion Beam for Three Dimensional Tomographic Reconstruction of Microstructural Development in Forged Al-Ni-Y-Co alloys

Presented by

Mauricio Andres Gordillo, B.S.

Major Advisor _____

Dr. Mark Aindow

Associate Advisor _____

Dr. Harold Brody

Associate Advisor _____

Dr. Leon Shaw

University of Connecticut

2011

Acknowledgments

Firstly, I would like to thank Dr. Mark Aindow for his support as my major advisor and mentor. I owe the completion of this thesis mainly to his patience, and the confidence he had in me. I also want to give my appreciation to Dr. Harold Brody and Dr. Leon Shaw for being on my advisory committee.

Thanks are given to Dr. Roger Ristau and Dr. Lichun Zhang for their assistance on the characterization instruments and all the helpful discussions. In addition, special thanks is given to Lichun for giving me permission to use XRD and TEM data that he obtained on the alloys in this study prior to me starting at UConn.

I want to give special thanks to Dr. Gary Salivar at Florida Atlantic University for being the person who first introduced me to the world of materials engineering. Also, special thanks are given to Dr. Thomas O'Connell at HEICO Aerospace who served as a colleague, mentor, but most importantly as a friend. Thank you both for all the helpful discussions and the encouragement to apply to graduate school.

I also want to thank all of my group members and all the friends I have made while at UConn for their support.

Finally, I want to thank everyone I know back home for their love and support through this experience, especially my family: Mami, Alejandro, Jessica, Wita, and James because without you guys I would not be where I am today. Thanks.

Table of Contents

Abstract

There has been significant interest in the use of metastable vitreous intermediates in the development of new high strength Al alloys. Such intermediates have much higher solubility limits than traditional Al alloys. Thus, by careful control of alloy composition and thermal history during devitrification, one can obtain fine-grained microstructures with higher volume fractions of precipitates than can be achieved in traditional Al Alloys. Aluminum-Rare Earth-Transition Metal alloys are materials that can be produced in the amorphous state by gas atomization. For this study, an Al-11Ni-13Y-1Co wt% (Al-6.0Ni-4.7Y-0.5Co at%) alloy was investigated. During consolidation and extrusion of the amorphous powder, the material devitrified giving a microstructure consisting of a FCC Al matrix with laths of an $Al_{19}Ni_5Y_3$ phase. The objective of this study was to investigate the microstructural evolution of these materials after subsequent forging upsets of 43%, 64% and 84%. Conventional characterization tools, such as XRD, SEM and TEM, were used to study these materials. Data obtained from these techniques revealed that the $Al_{19}Ni_5Y_3$ precipitates did not break up as one might expect, but instead rotated during forging. However, the morphological data is limited and the rotation of the particles could only be inferred. Therefore, FIB tomography was used to further study the microstructural development after processing. Data sets consisting of 200 images for each material were obtained from serial sectioning experiments. The appropriate post-processing steps were performed followed by segmentation, and three-dimensional reconstructions of the $Al_{19}Ni_5Y_3$ precipitates were obtained. These reconstructions along with the data obtained from XRD, SEM and TEM revealed the way in which the $Al_{19}Ni_5Y_3$ rotated with the plastically flowing Al matrix during forging.

Chapter 1: Introduction

1.1 **Advantages of Al alloys**

1.2 **Disadvantages of Al alloys**

1.3 **New high strength Al alloys**

1.4 **Objectives and Approach of this study**

1.5 **Structure of this Thesis**

Chapter 1: Introduction

One of the main concerns in modern aerospace technology is the current levels of efficiency are not consistent with increasingly severe economic and environmental constraints. There are several ways in which this issue could be addressed, but by far the most direct is to reduce the weight of the aircraft and thereby to increase the performance. As a result, there has been a trend towards more extensive use of low density metals such as Ti, Mg, and Al, in addition to even lighter materials such as polymers and composites. While the use of these latter non-metallic materials offer very significant potential weight savings, there are still many components for which the use of metals is essential. For example, Ti is used extensively in gas turbine engines because of its good elevated temperature strength and oxidation resistance. Mg is another low density metal that shows good strength and fatigue properties, and can be aged hardenable. Unfortunately, Ti has an extremely high production cost, and Mg can have issues relating to its corrosion and oxidation resistance, and there are some difficulties in obtaining good quality castings. Al costs much less to produce than Ti, has better oxidation and corrosion resistance that Mg, and can be easily processed by a wide range of techniques. Unfortunately, the maximum strength of Al alloys is rather limited. As a result, there has been extensive research focused on improving the mechanical properties of Al, with the objective of expanding the range of applications for which such alloys can be used. The purpose of this chapter is to introduce: the advantages and disadvantages of Al as an aerospace material; the two main methods used to develop new high strength Al alloys; and the structure and objectives of the thesis.

1.1 Advantages of Al alloys

Density - One of the most notable properties of Al is its low density of 2.70 g cm^{-3}. For comparison, the densities of Fe and Ti are 7.87 g cm^{-3} and 4.5 g cm^{-3}, respectively. Thus, the weight of a component manufactured from Al would be approximately 1/3 and 1/2 of those for components of the same geometry produced from Fe and Ti, respectively.

Processing – Another key advantage of Al is the ability to manufacture a variety of products by different processing techniques. Al is very easily cast because of its low melting temperature. The direct chill casting method can be used to produce Al bar stock in a range of sizes. Additionally, Al can be cast into more complex shapes by sand, investment, and die casting. In terms of wrought product, Al's high ductility makes it very malleable, allowing for processing by extrusion into billets or rolling into sheet and plate; both processes can be done at either ambient or elevated temperatures. Moreover, Al alloys can be heat-treated to alter strength levels. Work hardened material can be softened by annealing treatments; other alloys can be precipitation strengthened by artificial or natural aging. This wide range of capabilities allows Al to be made into components such as housings, rivets, sheet skin, and structural beams.

Oxidation Resistance - Another important property of Al is that it readily reacts with oxygen in the atmosphere producing a thin layer of aluminum oxide. Because this oxide layer is impervious, it will protect the material underneath from further oxidation. However, if further oxidation resistance is required, the oxide layer can be further enhanced by a chemical treatment called anodizing. This is an electrolytic passivation

process (using sulfuric or chromic acids) that causes an increase in the native oxide thickness. This enhances corrosion and wear resistance and the adhesion of paints and primers. In addition, chromate conversion coatings can be applied for added protection on top of the anodized layer. Moreover, some anodizing layers are porous allowing dyes to be absorbed to add color for aesthetic purposes

1.2 **Disadvantages of Al alloys**

Limited strength at room and elevated temperatures – A major limitation of Al is that its ambient temperature strength is lower than that of other aerospace metals. Al alloys have tensile strengths ranging from 90 MPa for fully annealed alloys and up to 600 MPa for alloys aged hardened to peak strength. These values are significantly lower than those for Ti alloys, which range from 280 – 1200 MPa, or for steels ranging from 330 – 1700 MPa. As such, Al components require larger cross sections to reduce stresses, but size constraints can become an issue in confined spaces. Another limitation is Al's limited strength at elevated temperatures. Because Al has a low melting point, it does suffer softening effects with increasing temperature at an earlier stage than other metals. Most Al alloys are limited to operating conditions of up to 150°C, since prolonged exposure at this and higher temperatures will cause a rapid decline in strength.

Lack of Endurance Limit – Another important drawback of Al is its fatigue behavior. Many materials like Fe and Ni have what is called an "endurance limit." This property is defined as the highest stress that a material can bear under cyclic loading where the probability of failure by fatigue will be zero. This fatigue property is very important

because many components will experience loading and unloading stresses during flight. For example, the deflections of the wings and the vibrations of structural parts near the engines cause stress oscillations. Unfortunately, Al does not have an endurance limit, meaning that Al components will eventually fail due to fatigue even if subjected to very low stress amplitude cyclic loadings. This further restricts the range of applications for which Al can be used in aircraft [3].

1.3 New high strength Al alloys

There have been many attempts to develop new Al alloys with improved properties to further expand their use in aerospace applications. The following section describes two of the methods that have received most attention.

$L1_2$ precipitate strengthening –One approach to improving the properties of Al alloys is the formation of a high volume fraction of fine, coherent precipitate particles adopting the ordered face centered cubic structure $L1_2$ structure. This is analogous to the strengthening of Ni-based superalloys by the gamma prime intermetallic phase, Ni_3Al. The presence of a high volume fraction of this gamma prime phase is one of the main reasons for the exceptional strength in many Ni-based superalloys; therefore, an Al derivative was sought to exploit this strengthening approach. In Al alloys, such a derivative could be produced by additions of Sc and/or Zr. The solutionized alloys could then be aged to form precipitate phases like Al_3Sc or $Al_3(Sc_{1-X}Zr_X)$. These intermetallics have the $L1_2$ crystal structure with lattice parameters similar to that of FCC Al, which would enable these precipitates to be coherent with respect to the matrix. These

microstructural traits would provide hardening mechanisms through coherency strains and anti-phase boundary energies. The first part of the literature review (Chapter 2) will discuss in detail the microstructural characteristics of the Al-Sc and Al-Sc-Zr alloys. The resultant improvements in strength are discussed, together with grain size refinement and recrystallization resistance effects in these alloys [3, 4].

Al-RE-TM – The second approach to the design of new high strength Al alloys is through the formation of a metastable metallic glass, which is then devitrified in a controlled manner leading to the required microstructure. Such Al-based metallic glasses are formed most easily by additions of rare earths (such as: Y, Ce & Gd) and transition metals (such as: Ni, Fe & Co). These additions reduce the critical cooling rate necessary to form a metallic glass. The main advantage of forming an amorphous phase is that it bypasses solubility limitations; in the amorphous state higher concentrations of alloying elements can be accommodated in solution than in crystalline solid solutions. The consequence of this is that a higher volume fraction of precipitates can be formed during subsequent devitrification heat treatments than could be achieved by precipitation from crystalline solid solutions. The main focus of this thesis will be the detailed microstructural analysis of one such devitrified Al-based metallic glass alloy.

1.4 Objectives and Approach of this study

The objective of the work described in this thesis was to perform a detailed study of the microstructural development in a new Al-Y-Ni-based alloy produced by the gas turbine company Pratt & Whitney. To obtain the rapid cooling rates required to form the amorphous phase, stock material was produced through powder metallurgy techniques. First, the amorphous powder was produced by gas atomization. Then the powder was consolidated into Al cans and extruded at elevated temperature, whereupon the alloy devitrified fully. Therefore, the alloy consisted of Al grains with a high volume fraction of complex structured precipitates. This alloy was then subjected to a series of processes (extrusion and different levels of forging) that are common for materials being used for aerospace applications. After each processing stage the microstructure was characterized to reveal any changes in structure, morphology, and orientation. This was accomplished by imaging, diffraction, and spectrometry using the transmission electron microscope (TEM), scanning electron microscope (SEM), and X-Ray diffraction (XRD), and by using the serial sectioning and imaging capabilities of the dual-beam focused ion beam/scanning electron microscope (FIB/SEM). The FIB/SEM allowed stacks of two dimensional images to be acquired. These stacks were then used to reconstruct a three dimensional (3D) model of the alloy precipitates and thus to show in 3D the changes in orientation of the precipitates with processing.

1.5 Structure of this Thesis

This thesis is divided into 6 sections: Introduction (current chapter), Literature Review, Materials and Experimental Methods, Results, Discussion, and Conclusions.

Chapter 2 discusses the research on new high strength Al alloys via two methods, the addition of Sc and Zr to form coherent $L1_2$ precipitates, and the amorphous Al-RE-TM alloys. Chapter 3, the Materials and Experimental Methods includes: the alloy compositions, the processes to which the alloys were subjected (heat treatment, extrusion, forging, etc), and a summary of the specimen preparation and analytical techniques used on the TEM, SEM, XRD and FIB/SEM. Chapter 4 contains the results from XRD, SEM, the TEM experiments (images, diffraction patterns, etc) and the reconstructions of the FIB/SEM image stacks showing the precipitates in 3D. Chapter 5 is a discussion of the experimental results explaining how the microstructural changes arise during processing. Finally, Chapter 6 is a summary of the important points arising from this study.

Chapter 2: Literature Review

2.1 Alloying to form Al_3X

2.1.1 *Binary Al-Sc Alloys*

2.1.2 *Addition of Zr to Al-Sc alloys*

2.1.3 *Other benefits of Al_3Sc phase*

2.1.4 *Limitations of Al_3Sc precipitation*

2.2 Alloying for BMG formation

2.2.1 *General metallic glass formation*

2.2.2 *Amorphous Al alloys*

2.2.3 *Partially devitrified Al amorphous alloys*

2.2.4 *Fully devitrified amorphous Al alloys*

Chapter 2: Literature Review

As discussed in the Introduction, Al alloys provide numerous advantages for the aerospace field, including: low density, excellent corrosion resistance, and the ability to manufacture components via wide variety of processing methods. However, it is desired to further extend the use of Al alloys into environments that are not typically suitable for conventional Al alloys. Several different approaches have been used to improve the mechanical properties of Al alloys, but there are two methods that have received a lot of attention: the development of a fine dispersion of coherent $L1_2$ precipitate particles within the Al matrix, and the formation of a very fine microstructure with a high volume fraction of precipitate particles through the controlled devitrification of a metastable metallic glass. The emphasis of this chapter will be the discussion of these two approaches.

2.1 Alloying to form Al_3X

Coherent $L1_2$ precipitates can be formed in several Al systems, such as Al-Zr, Al-Li, and Al-Sc, of which the latter has received the most attention. Initial research on Al-Sc systems was being performed during the 1960s, but interest grew rapidly after the publication of the 1971 U.S. patent titled "Aluminum Scandium Alloy." The abstract of the patent states: "Aluminum and aluminum alloys of varying binary, ternary, and multicomponent types having from 0.01 to about 5.0 percent by weight of scandium characterized by improved physical properties and methods of thermally treating the same." The patent does not discuss, in any detail, the mechanisms responsible for the improvement in the physical properties [1].

2.1.1 *Binary Al-Sc Alloys*

General Crystallography – Al_3Sc adopts the $L1_2$ crystal structure, which is simple cubic but looks like an ordered face centered cubic lattice. A schematic diagram of the Al_3Sc unit cell is shown in Figure 2.1. The Sc atoms are located at the cube corners, and the Al atoms are in the centers at the cube faces. The pure Al_3Sc stoichiometric compound has a lattice parameter of 0.4105 nm; which is approximately 1.5% larger than that of FCC Al [2, 3]. Because of the low lattice mismatch between the Al_3Sc compound and FCC Al, Al_3Sc precipitates can form coherently with the Al matrix.

Phase Diagram, solubility, and typical compositions – The complete equilibrium Al-Sc phase diagram is shown in Figure 2.2a. It can be seen that several intermetallic compounds form in this system. A partial diagram of the Al-rich end of the Al-Sc phase diagram is shown in Figure 2.2b. This region of the binary phase diagram is dominated by a eutectic reaction between α-Al and Al_3Sc occurring at approximately 660°C and 0.6-wt% Sc [2]. Since the Al-Sc system exhibits an increase in the solid solubility of Sc in α-Al with increasing temperature, these alloys can be solution heat-treated and then quenched to retain the Sc in a super-saturated solid solution (SSSS). Precipitation aging treatments can then be performed on the SSSS to form a fine dispersion of Al_3Sc particles in the matrix. The equilibrium maximum solubility has been reported to be approximately 0.38-wt% Sc at the eutectic temperature of about 660°C; this lies close to the melting point of pure Al at 661°C [3, 4, 5]. However, in practice processes occur under non-equilibrium conditions and concentrations as high as 0.6-wt% of Sc have been retained in solution during continuous casting of ingots [3, 5]. Several different Al-Sc

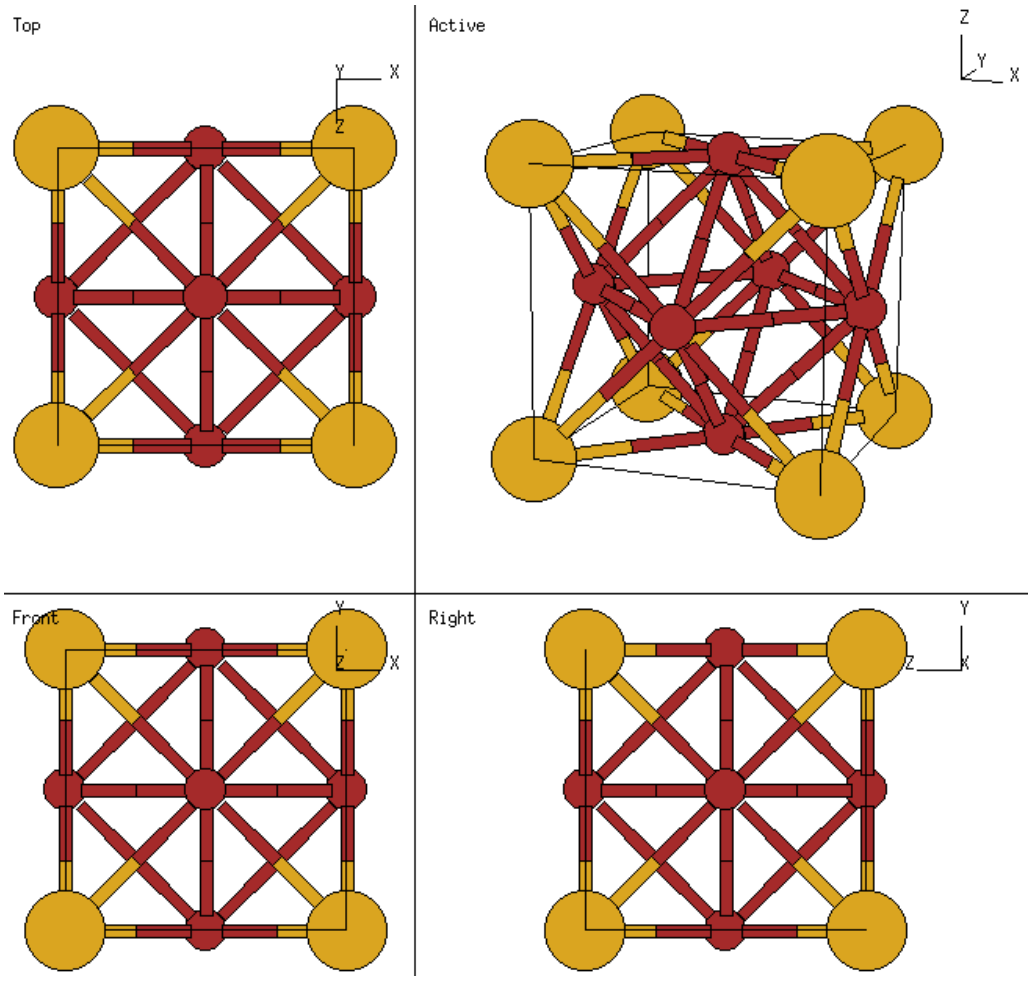

Figure 2.1: Schematic diagram of the $L1_2$ unit cell. For the Al_3Sc compound, the atoms at the cell corners are Sc and those in the centers of the cell faces are Al. Reproduced from ref [39].

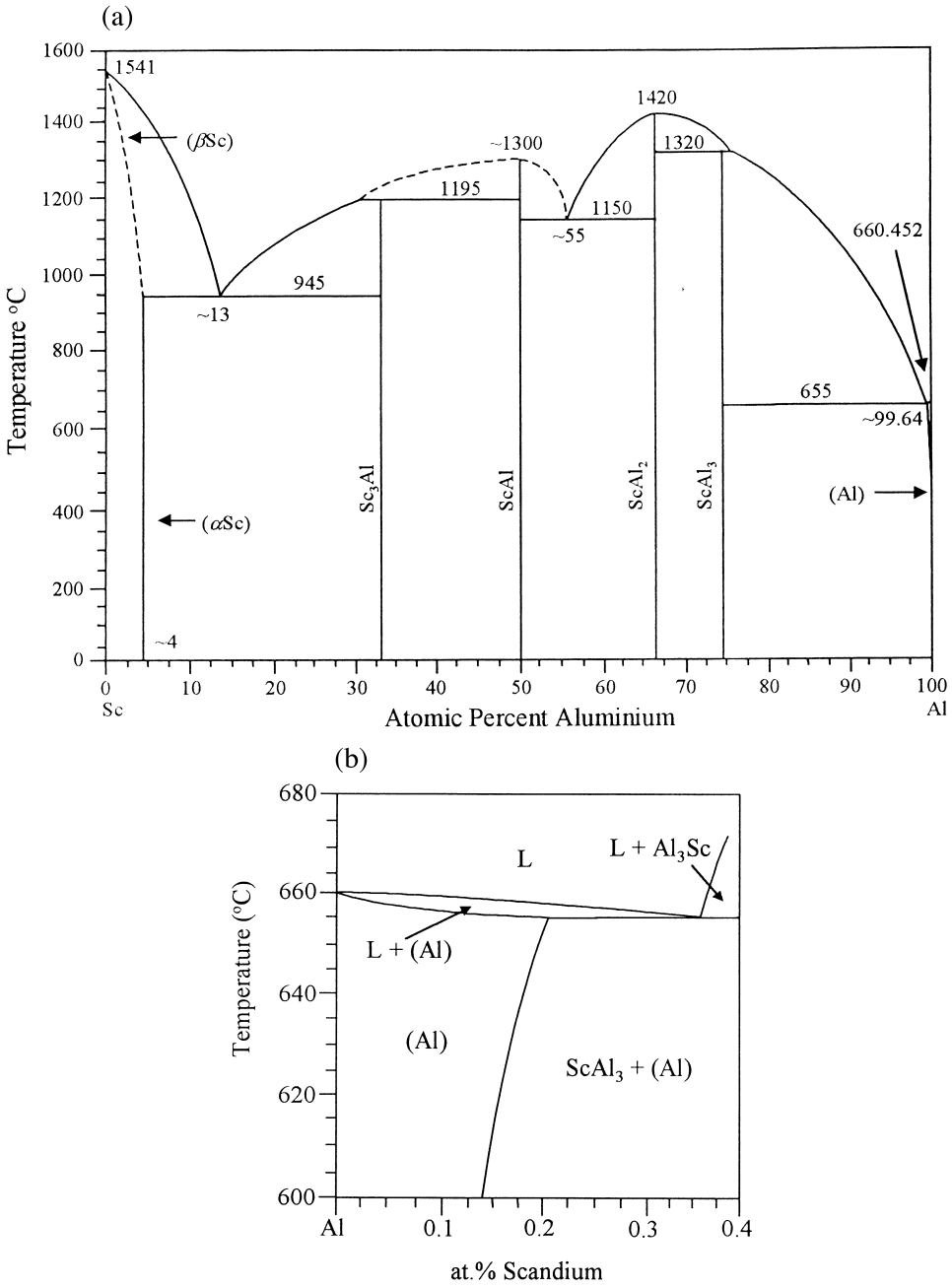

Figure 2.2: Binary Equilibrium Al-Sc phase diagrams. a) Complete phase diagram, b) Partial diagram from the Al rich end of the Al-Sc system. Reproduced from ref [2].

alloys have been studied, ranging from 0.1 up to 1.25-wt% Sc, thus covering a whole range of hypo- and hyper-eutectic systems. Although most of the research has been done on hypoeutectic alloys, there are still some very important uses for hypereutectuc alloys that will be discussed later on.

Many of the precipitation-hardenable Al-Sc alloys are produced using Sc concentrations of up to 0.38-wt% (0.21-at%), such that solution heat treatments can be used to retain all of the Sc into solid solution, and then followed by aging treatments that precipitate the Al_3Sc compound. The temperatures used for precipitation heat treatments range from 250 - 450°C, depending on the rate of precipitation and the particle size distributions desired. Marquis et al conducted heat treatment experiments on a range of binary Al-Sc alloys (0.1 – 0.3-wt% Sc) at various temperatures (250 – 450°C) and showed that the particle size distribution and coarsening was affected by the aging temperature. They showed that increases in aging temperature led to faster precipitation and faster coarsening of precipitates [4, 6].

Coherency and size of Al_3Sc particles – The most notable characteristic of Al_3Sc is that it is coherent with the Al matrix. Since there is a potential for strengthening, several groups have conducted experiments showing that various sizes and distributions of coherent Al_3Sc precipitates do form in Al-Sc systems [2-8]. For example, Marquis et al took a series of Al-Sc alloys containing 0.1 to 0.3-wt% Sc, homogenized them at 648°C, water quenched, and then precipitation hardened them between 275 to 400°C [6]. These treatments resulted in the formation of spherical Al_3Sc precipitates with radii ranging from 1.4 to 9.6 nm. The results of this experiment are displayed in Figure 2.3. Figures

2.3a and 2.3c show the effect of composition on the size and density of Al_3Sc particles in two Al-Sc alloys (0.3 and 0.1 wt% Sc, respectively) that were both heat-treated at 300°C for 72 h. The 0.3 wt% Sc alloy contained a much finer dispersion of the Al_3Sc particles than the 0.1 wt% Sc alloy. The effect of temperature is shown in Figure 2.3b, in which an Al-0.3 wt% Sc alloy was aged at 400°C for 5 h; the particle sizes in Figure 2.3b are similar to those in the 0.1 wt% Sc alloy (Figure 2.3c), but the density of particles is higher in Figure 2.3b. Coherency of the particles was verified by the presence of strain field contrast; one example is shown in Figure 2.3d [6]. However, as these particles grow there is a critical size beyond which it will be energetically more favorable to introduce a dislocation at the particle/matrix interface than to increase the matrix strain. This transition from coherent to semi-coherent particles occurs for diameters greater than 40 nm. Figure 2.4 shows an example of a TEM micrograph of an Al-0.3 wt% Sc alloy aged at 400°C for 120 h where Al_3Sc particles are present with interfacial dislocations [4]. Other groups have described similar results in terms of particle size and coherency [7, 8]. Novotny and Ardell performed a series of heat treatments on Al-Sc alloys at 350°C for various times. A bright field TEM micrograph showing coherency strain contrast at coherent Al_3Sc precipitates is shown in Figure 2.5 for two Al-Sc alloys containing 0.2 and 0.3 wt% Sc, that were aged for 168 and 552 h, respectively. Novotny and Ardell reported that coherency still persisted in a 0.2-wt% Sc alloy aged for 4663 h at 350°C and [7].

Thermal Stability – Another noticeable property of the Al_3Sc compound is its elevated temperature stability. The phase diagram in Figure 2.2a shows that Al_3Sc melts

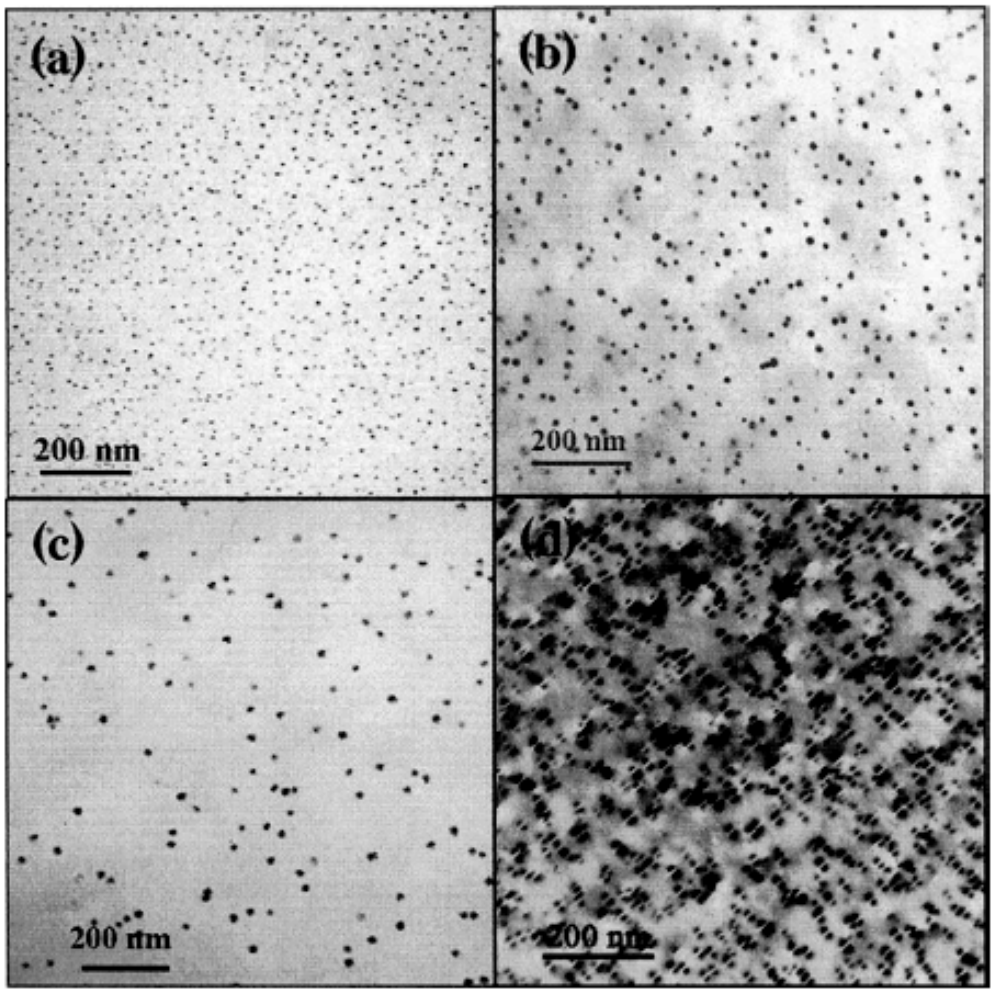

Figure 2.3: Two beam Dark field TEM micrographs: (a) Al-0.3 wt.% Sc alloy aged at 300°C for 72 h; (b) Al-0.3 wt.% Sc alloy aged at 400°C for 5 h; (c) Al-0.1 wt.% Sc alloy aged at 300°C for 72 h; and (d) coherency strain contrast in Al-0.2 wt.% Sc alloy aged at 300°C for 72 h. (a-c) using the (100) reflection and (d) using the (200) reflection. Reproduced from ref [6].

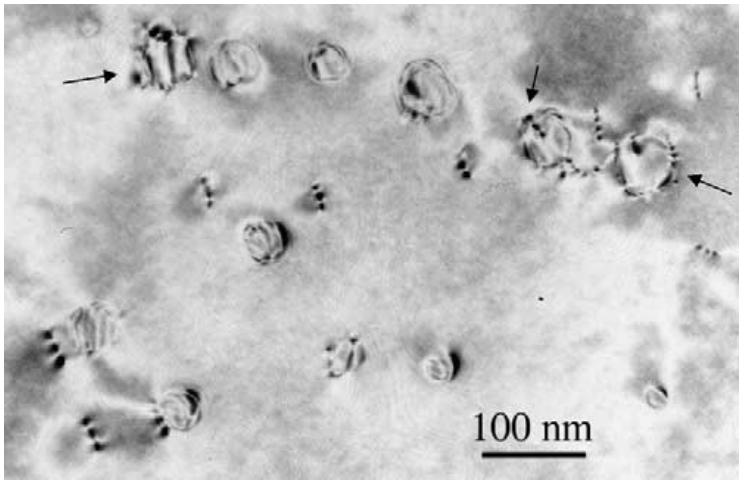

Figure 2.4: Two beam bright field TEM micrograph of interfacial dislocations at Al_3Sc precipitates in Al-0.3 wt% Sc alloy aged at 400°C for 120 h. **g** = [200]. Reproduced from ref [4].

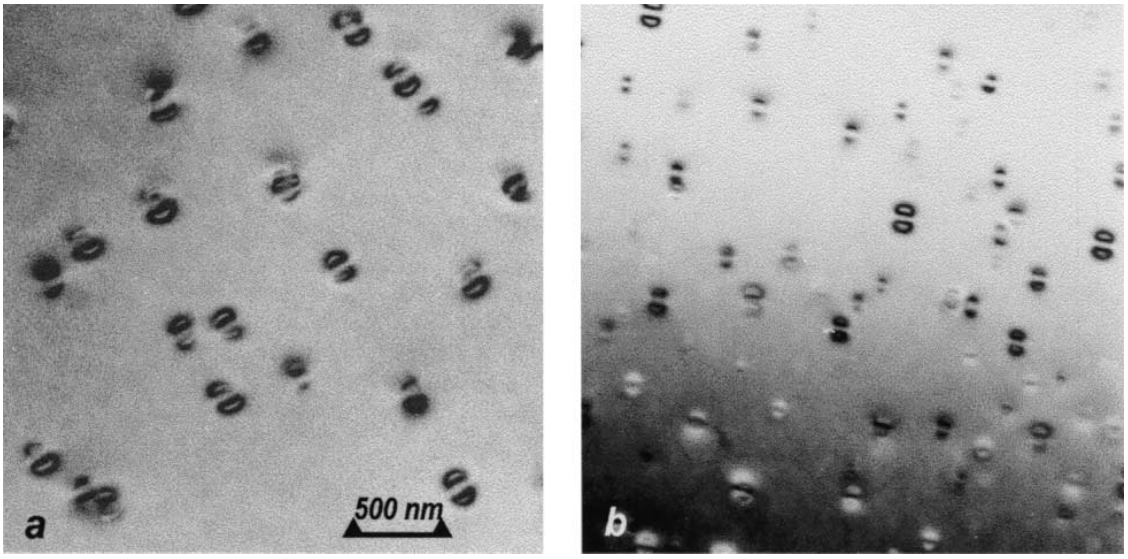

Figure 2.5: Bright field TEM micrographs showing coherency strain contrast at coherent Al_3Sc particles. (a) Al-0.2 wt% Sc alloy aged for 168 h at 350°C and (b) Al-0.3 wt% Sc alloy aged for 552 h at 350°C. Reproduced from ref [7].

peritectically at approximately 1320°C, which makes it a very attractive high temperature material [3]. On the other hand, traditional Al alloys have very low strengths at elevated temperatures because precipitate particles begin to re-dissolve at temperatures above 200°C causing the rapid loss in strength. However, experiments have shown that Al_3Sc is stable at elevated temperatures. Marquis et al performed heat treatments on an alloy containing 0.3-wt% Sc at temperatures ranging from 300 - 450°C for 1 – 350 hours. A plot is shown in Figure 2.6 that summarizes the average precipitate radius as a function of the cube root of aging time at different aging temperatures. The plot shows that the Al_3Sc particles coarsen more slowly at the lower temperatures (300 and 350°C) than at 400 and 450°C. However, it is important to remember that these temperatures exceed the operating temperatures of traditional Al alloys. Others have also shown comparable coarsening results at elevated temperatures. Watanabe et al conducted elevated temperature experiments on a 0.28-wt% Sc alloy at 400 - 450°C for up to 1350 hours [8]. A plot showing the change in average precipitate radius with aging time is shown in Figure 2.7 for the 0.28 wt% Sc alloy aged at 400, 425, and 450 °C (673, 698, and 723 K, respectively). TEM dark field images of this Al- 0.28 wt% Sc alloy aged at different temperatures and times are shown in Figure 2.8. Novotny and Ardell also conducted long-term aging treatments on 0.2 and 0.3 wt % Sc alloys at 350°C. The microstructural evolution of Al-0.2 wt% Sc and Al- 0.3 wt% Sc alloys aged at 350°C for various extended periods of time are shown in Figures 2.9 and 2.10 respectively. The TEM images in Figure 2.9 show that the Al_3Sc particles in the Al-0.2 wt% Sc alloy exhibit only a small change in size at long aging times. In comparison, the TEM images for the Al-

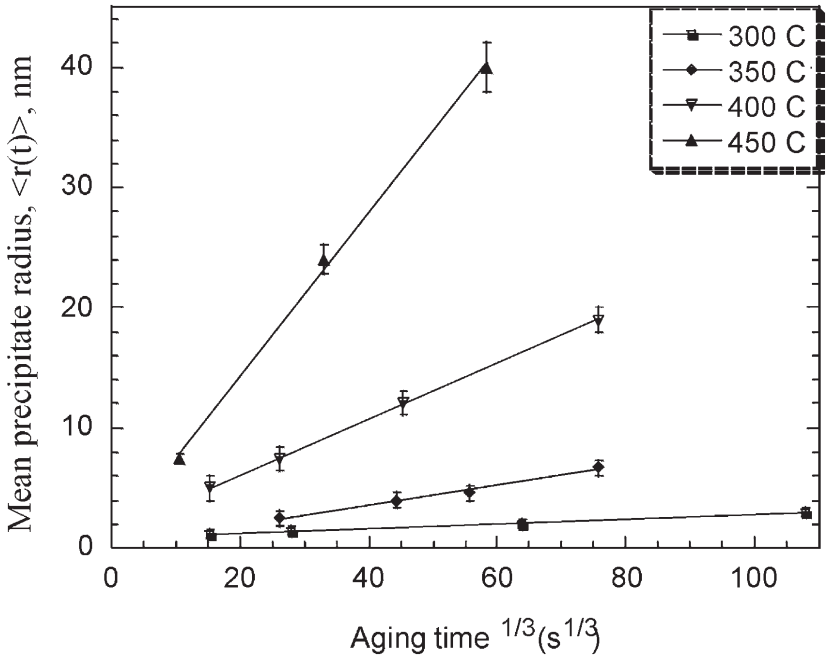

Figure 2.6: Average precipitate radius (nm) in a Al-0.3 wt% Sc alloy as a function of the cube root of the aging time for different aging temperatures. Reproduced from ref [4].

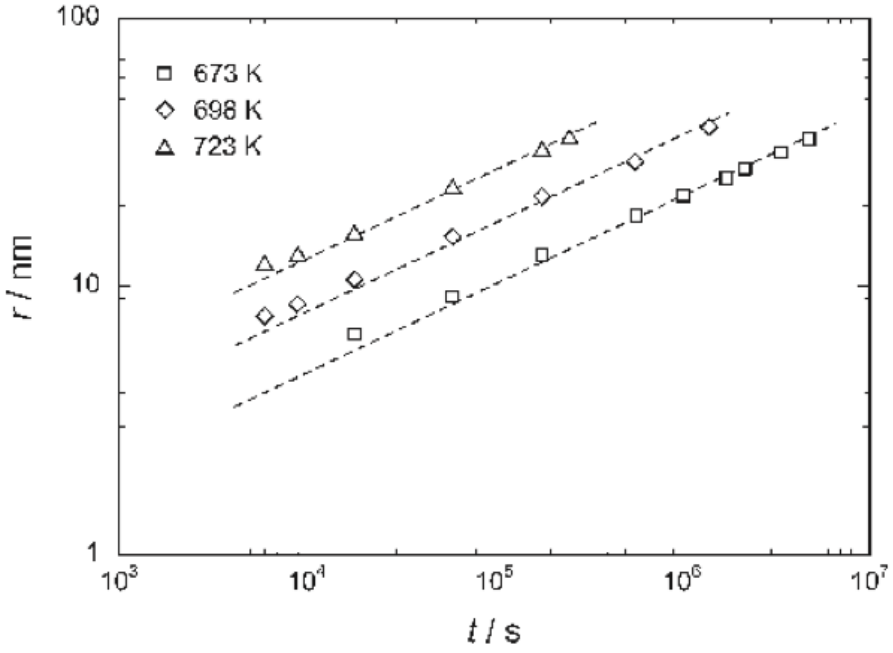

Figure 2.7: Change in average precipitate radius r with aging time t for an Al-0.28 wt% Sc alloy aged at 673, 698, and 723 K. Reproduced from ref [8].

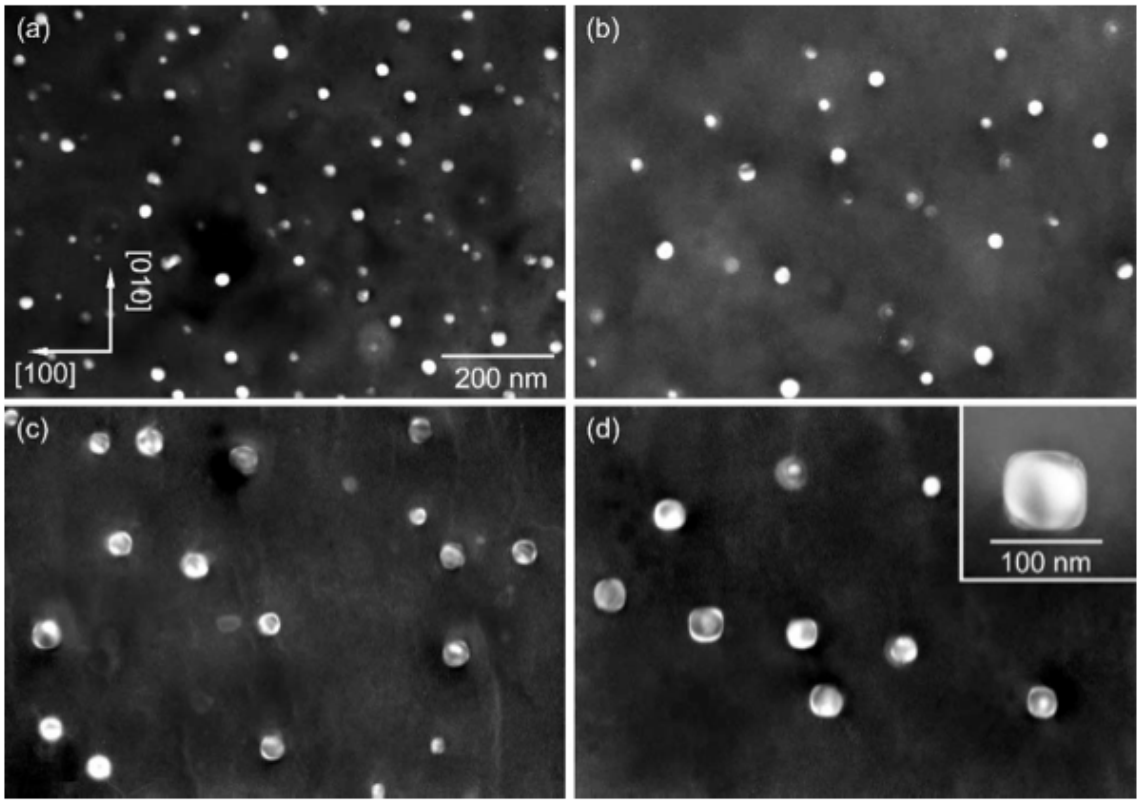

Figure 2.8: Dark field TEM images of Al_3Sc precipitates in an Al-0.28 wt% alloy aged (a) at 673 K for 5 h; (b) at 673 K for 50 h; (c) at 698 K for 50 h; and (d) at 723 K for 50 h. Zone axis: [001]. Reproduced from ref [8].

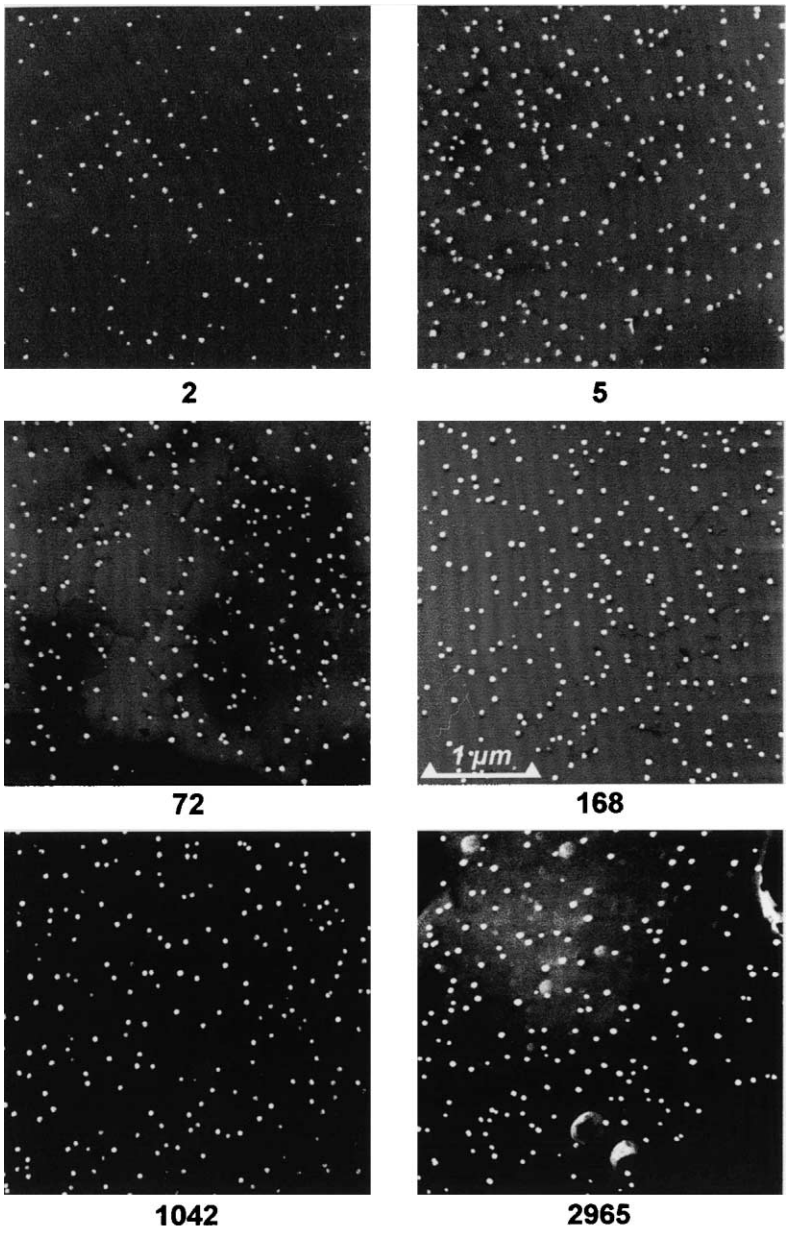

Figure 2.9: Evolution of the Al_3Sc precipitate microstructure in an Al-0.2 wt% Sc alloy aged at 350°C. The number under each figure is the aging time in hours. Reproduced from ref [7].

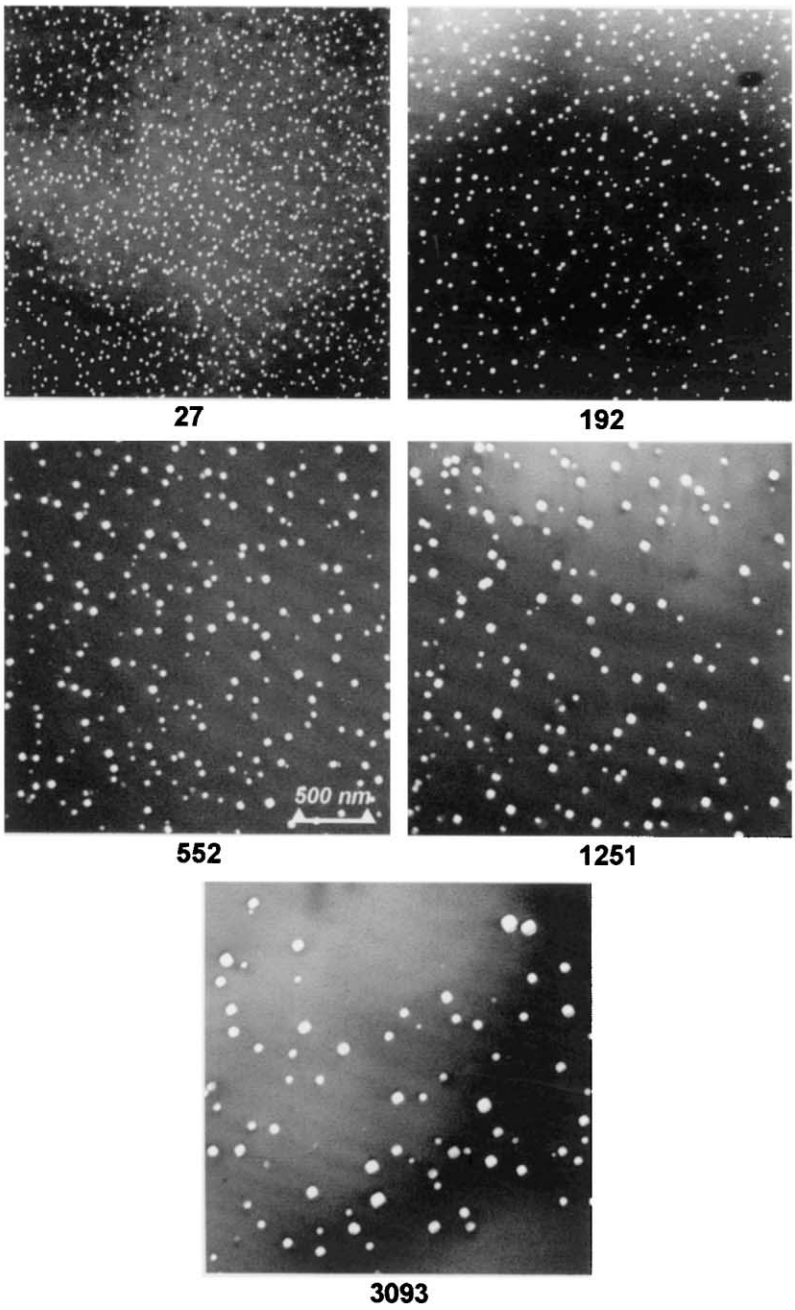

Figure 2.10: Evolution of the Al_3Sc precipitate microstructure in an Al-0.3 wt% Sc alloy aged at 350°C. The number under each figure is the aging time in hours. Reproduced from ref [7].

0.3 wt% Sc alloy in Figure 2.10 show a higher density of finer particles, but the particles become much larger than those in the 0.2 wt% Sc alloy at longer aging times [7].

Effect on Mechanical Properties – The motivation for the formation of the Al_3Sc precipitates is to enhance the mechanical properties of Al alloys. There are been many examples where the yield and ultimate strengths (at room and elevated temperature) of pure Al and its alloys have been improved by the addition of Sc and Zr [3, 5, 6, 11-16]. Marquis et al have done extensive heat treatment experiments on 0.1, 0.2, and 0.3-wt% Sc alloys showing the relationship between aging times at 300°C and precipitate particles size; a plot of the micro-hardness versus aging time for these three different Sc concentrations is shown in Figure 2.11. The results in Figure 2.11 show that the hardness of the alloy increases with the Sc concentration, which matches well with the microstructures shown previously where higher Sc concentrations result in higher volume fractions of much finer precipitates. Marquis et al also plotted the effect of aging temperature on the micro-hardness as a function of aging time in Figure 2.12. The highest strength is achieved at an aging temperature of 275°C, where it eventually plateaus. High aging temperatures give a much more rapid strengthening response, but they also result in a rapid decay in strength as seen for the 400°C curve. To illustrate the remarkable improvements in strength, pure Al in the O temper (annealed) has a yield strength of 30 MPa while a binary Al-0.3 wt% Sc alloy aged at 300°C showed a yield strength of 209 MPa. After a subsequent anneal at 400°C for 7 hours, the yield strength only dropped to 140 MPa. The greatest strength was achieved with precipitate particles measuring 1.4 nm in radius. A TEM micrograph of an Al-0.3 wt% Sc alloy that was

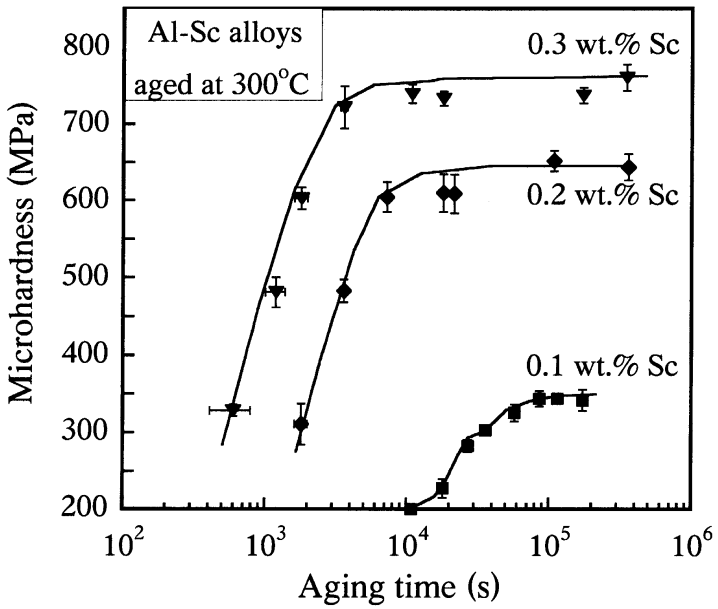

Figure 2.11: Vickers micro-hardness versus aging time (aged at 300°C) for three Al-Sc binary alloys (0.1, 0.2, and 0.3 wt% Sc). Reproduced from ref [6].

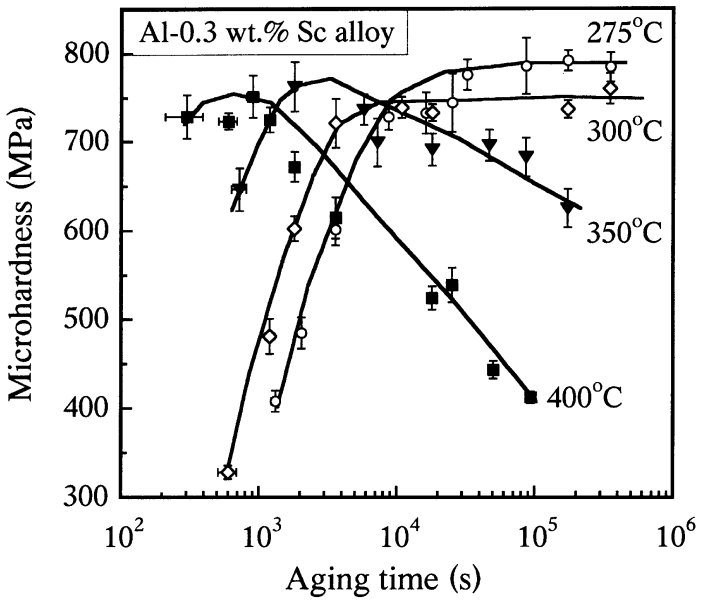

Figure 2.12: Vickers micro-hardness versus aging time for an Al-0.3 wt% Sc alloy at different aging temperatures (275, 300, 350, and 400°C). Reproduced from ref [6].

subjected to an ambient compression test to 20% strain is shown in Figure 2.13a. The microstructure consists of fine Al_3Sc particles with radii of 1.4 nm surrounded by dislocations pairs. The pairing of the dislocations indicates that particle cutting is occurring because dislocations pairs are required to cut through the ordered Al_3Sc crystals in order not to leave an anti-phase boundary. The microstructure of the same alloy that was further heat-treated to coarsen the particles to a radius of approximately 5.9 nm is shown in Figure 2.13b. The particles are too large to be cut and dislocation looping can be seen in the microstructure [6]. Fuller et al also did some extensive heat treatments using Al-Sc-Zr alloys and show comparable results of room and elevated temperature strengths [13]. In addition to these binary Al-Sc alloys, work has also been conducted on commercial Al alloys such as 2000, 3000, and 5000 series alloys with small Sc additions (0.1 – 0.3 wt %). Improvements in properties have been reported but difficulties in finding an appropriate heat treatment for precipitation hardenable Al alloys (such as 2000 and 7000 series) has limited the use of Sc in these systems [3, 14-16].

2.1.2 *Addition of Zr to Al-Sc alloys*

An important development in Al-Sc alloys was the addition of Zr. When Zr is added to Al-Sc alloys, the Zr atoms tend to dissolve into the Al_3Sc compound, substituting up to 50% of the Sc atoms in the crystal, forming the $Al_3(Sc_{1-X}Zr_X)$ compound. This phase still maintains the $L1_2$ structure and remains coherent with the Al matrix. Because of the 50% substitution of the Sc atoms by Zr, higher volume fractions of Al_3Sc precipitates can be formed; another way to view this is that less Sc is required to form a given volume fraction of precipitates, which will help to reduce costs. There has

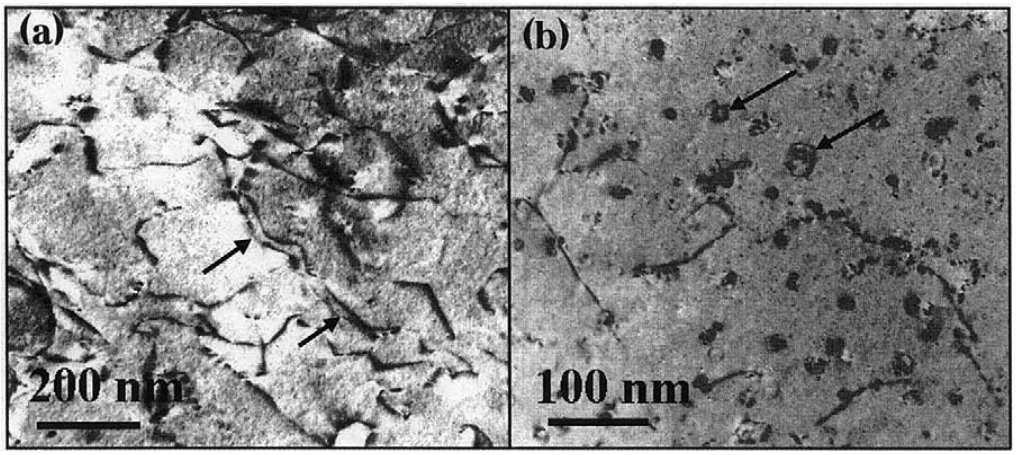

Figure 2.13: TEM micrographs showing dislocation structure of an Al-0.3 wt% Sc alloy subjected to an ambient temperature compression test to 20% strain: (a) alloy aged at 300°C for 5 h with fine precipitates (r=1.4 nm). Dislocation pairs are marked with arrows. (b) alloy aged at 300°C for 5 h and 400°C for 3 h with coarser precipitates (r = 5.9 nm). Dislocation loops around precipitates are marked with arrows. Reproduced from ref [6].

been extensive work performed showing the effects of Zr on Al-Sc alloys in terms of improvements in strength, thermal stability, recrystallization resistance, and grain refinement [2, 3, 5, 9, 10, 13]. An example of the improvement in mechanical properties is shown in Figure 2.14, in which the micro-hardnesses of Al-0.2wt% Sc and Al-0.2wt% Sc-0.15wt% Zr alloys are plotted versus aging time. The alloy containing Zr reaches a higher peak hardness than the alloy without Zr [5]. A more extensive micro-hardness study is shown in Figure 2.15, which shows a more complex effect of the addition of Zr. The alloys with low Al_3Sc volume fractions showed improvements in hardness with the addition of Zr, whereas the alloys with high volume fractions showed slightly lower hardnesses with Zr [13].

Another benefit is that Zr additions increase the thermal stability of the Al_3Sc compound. The coarsening rate of the $Al_3(Sc_{1-X}Zr_X)$ compound is much slower than that of Al_3Sc, which helps Al-Sc-Zr alloys to maintain their strength at elevated temperatures [3, 5]. The thermal stability of the $Al_3(Sc_{1-X}Zr_X)$ compound can also be deduced from the hardness curves in Figure 2.15, where Al-Sc-Zr alloys exhibit less over-aging than Al-Sc alloys. In particular, the high volume fraction compositions show much better stability for the $Al_3(Sc_{1-X}Zr_X)$ compound compared to Al_3Sc.

2.1.3 *Other benefits of Al_3Sc phase*

In addition to the strengthening that the Al_3Sc phase provides to Al alloys, there are two other major uses of this compound: grain refinement and recrystallization resistance.

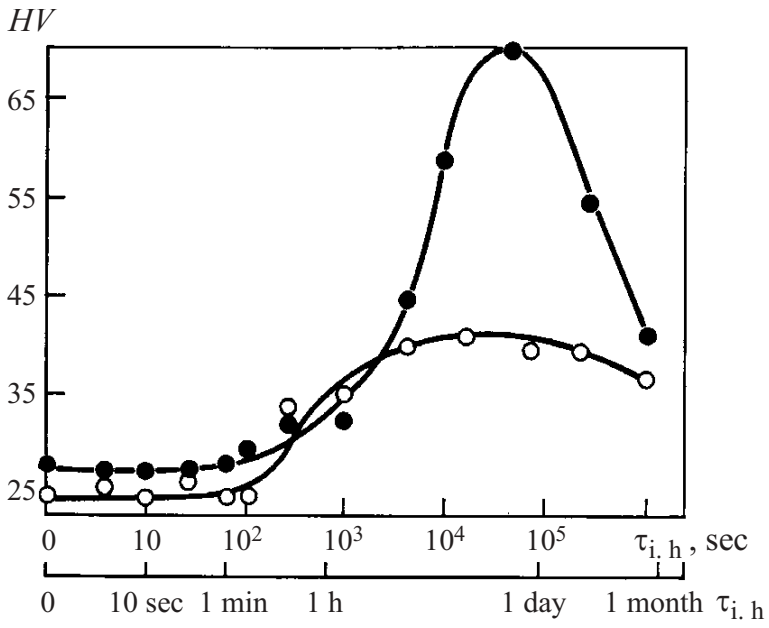

Figure 2.14: Micro hardness of Al-0.2 wt% Sc alloy (open circles) and Al-0.2 wt% Sc-0.15 wt% Zr alloy (dark circles) in continuously cast ingots as a function of isothermal hold at 400°C. Reproduced from ref [5].

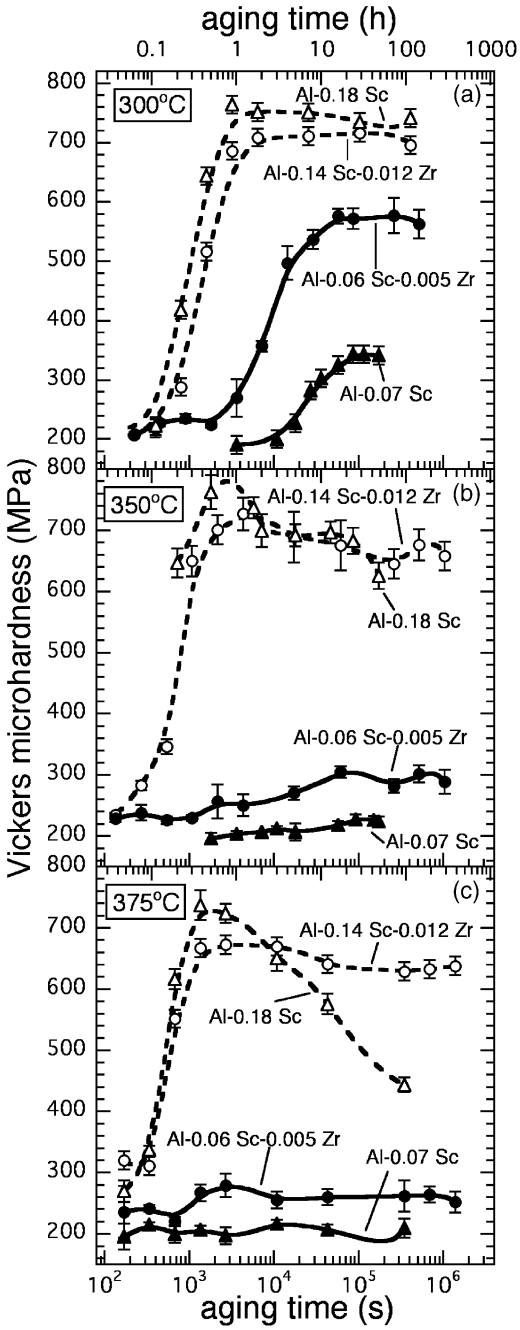

Figure 2.15: Vickers micro hardness vs aging time at 300, 350, and 375°C for two ternary Al-Sc-Zr alloys and two binary Al-Sc alloys. Reproduced from ref [13].

Grain Refinement – As discussed thus far, a lot of work has been performed on the precipitation of Al_3Sc in hypoeutectic Al-Sc alloys. However, there are also significant benefits to using hypereutectic Al-Sc alloys. Looking back to the phase diagram in Figure 2.2, during solidification of hypereutectic Al-Sc alloys, the first phase to form is Al_3Sc. Because the lattice mismatch between the Al_3Sc compound and FCC Al is low, these small particles act as nucleation sites for Al grains to form in a solidifying hypereutectic Al-Sc melt. This results in castings with non-dendritic structures and very fine equiaxed grains. This inoculation effect is shown in Figure 2.16, which shows the grain size of a cast Al-Sc alloys as a function of Sc concentration. At low Sc concentrations, the castings have very large grain sizes (greater than 0.8 mm in diameter), but when the Sc concentration surpasses the eutectic composition of 0.6 wt% Sc the grain size drops rapidly to approximately 0.1 mm in diameter. Moreover, Figure 2.17 shows the effect of adding Zr to an Al-Sc alloy, in which it is shown that the inoculation effect is achieved at even lower Sc concentrations [5]. To illustrate the grain refinement effect of Sc, Figure 2.18 contains images taken from different cast Al alloys with various compositions. The image in Figure 2.18a is the base line microstructure for an Al-4.5 wt% Cu alloy with very large grains ranging from 700 to 1200 μm in size. The images in Figures 2.18b and 2.18c are microstructures of Al-0.2wt% Sc and Al-0.7 wt% Sc alloys respectively. The grain sizes in the hypoeutectic alloy (Figure 2.18b) are comparable to those in Figure 2.18a showing no grain refinement, but the grains in the hypereutectic alloy (Figure 2.18c) have become very fine ranging from 25 to 70 μm in size. The images in Figures 2.18d and 2.18e show the effect of adding Zr, which is a typical grain-refining element in commercial Al alloys. The microstructure in Figure 2.18f consists of

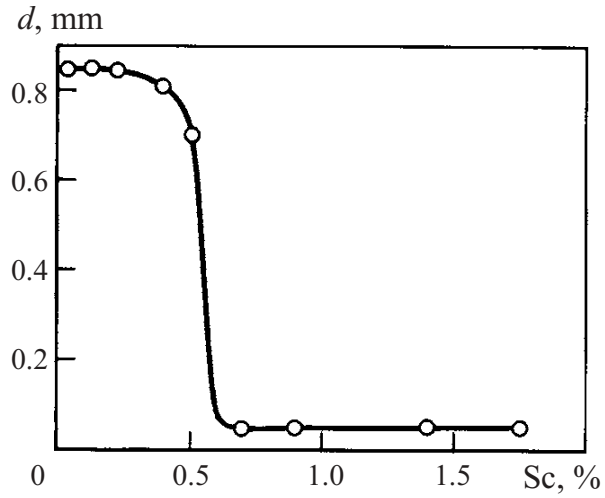

Figure 2.16: Grain size in a cast Al-Sc alloy as a function of Sc concentration. Reproduced from ref [5].

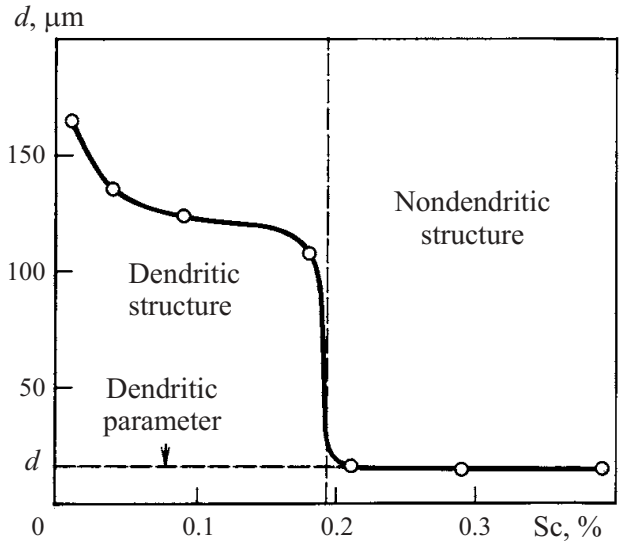

Figure 2.17: Grain size in a cast ternary Al-Sc-Zr alloy as a function of Sc concentration. Note that the addition of Zr produces a finer grain structure at a lower Sc concentration compared to Figure 2.14. Reproduced from ref [5].

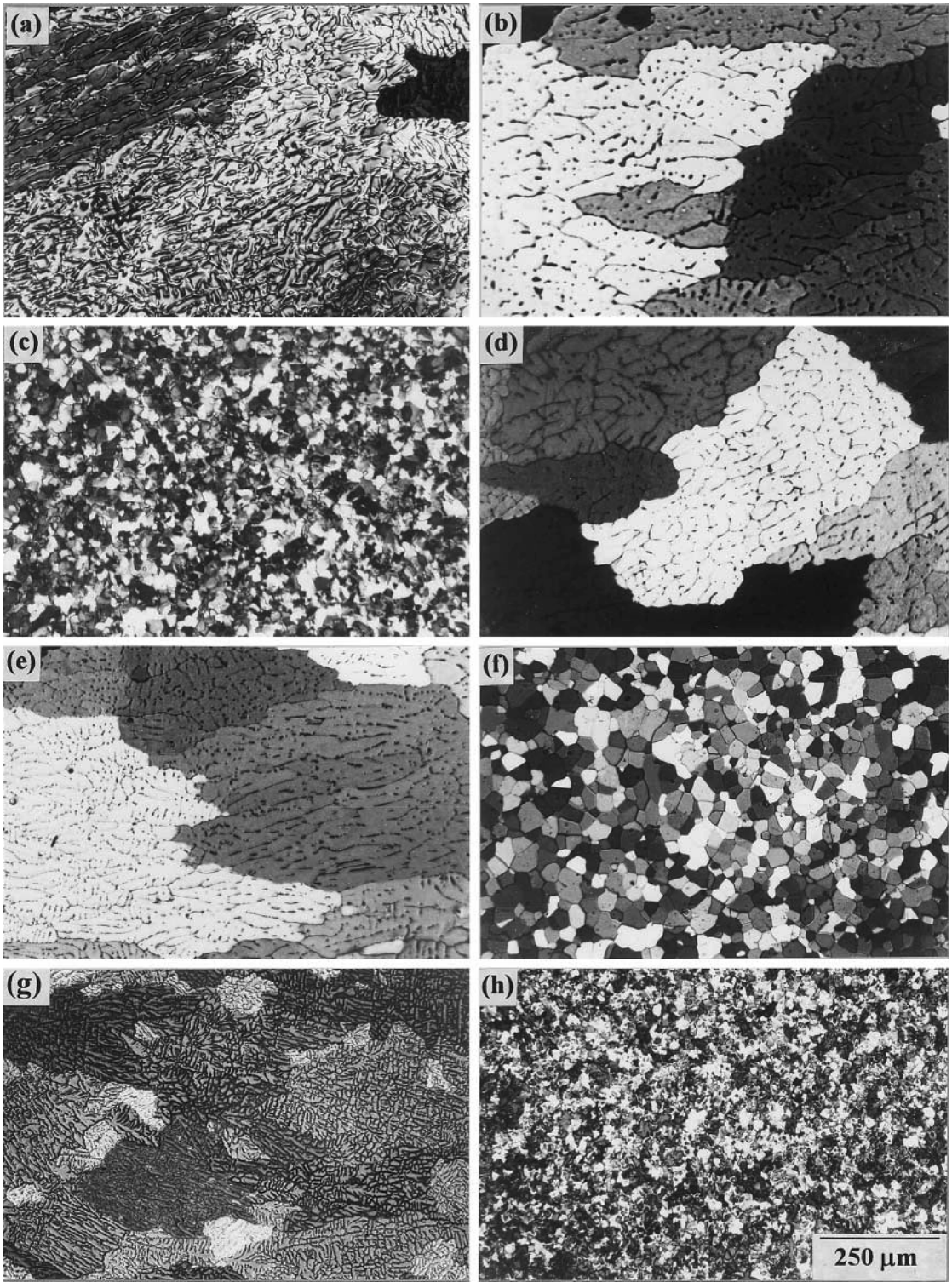

Figure 2.18: Examples of solidification microstructures taken from cast Al alloys (all in wt%): (a) Al-4.5 Cu; (b) Al-0.2 Sc; (c) Al-0.7 Sc; (d) Al-0.5 Zr; (e) Al-0.2 Zr; (f) Al-0.25 Sc-0.25 Zr; (g) Al-4.5 Cu-0.3 Sc; (h) Al-4.5 Cu-0.8 Sc. Reproduced from ref [2].

very fine equiaxed grains in an Al-0.25 Sc-0.25 Zr wt% alloy, which further demonstrates the benefit of adding Zr to Al-Sc alloys. The final two images, Figures 2.18g and 2.18h, are the microstructures of an Al-4.5 Cu-0.3 Sc wt% and Al-4.5 Cu-0.8 Sc wt% alloy, where the hypereutectic alloy has a much finer microstructure.

Recrystallization resistance – Another benefit of Al_3Sc is that it increases the recrystallization resistance of wrought products. Particles of Al_3Sc are very effective at pinning grain boundaries and preventing plastically deformed materials from going through the recrystallization process. Ocenasek and Slamova performed annealing treatments on cold worked Al-Mg alloys, some of which contained Sc and Zr. The Al alloys were cold rolled to 56% reduction in thickness before final annealing. Microstructures obtained after annealing at 360°C for 12 min are shown in Figure 2.19. The microstructure in Figure 2.19a is for an Al-Mg-Mn-Cr alloy, which has been fully recrystallized. However, Figures 2.19b and 2.19c are the microstructures for an Al-Mg-Mn-Cr-Sc-Zr and Al-Mg-Sc-Zr, which still retain the plastically deformed grain structure with no evidence of recrystallization. The same alloys were subjected to an annealing treatment at 520°C for 6 h, and the corresponding microstructures are shown in Figure 2.20. The Al-Mg-Mn-Cr microstructure in Figure 2.20a has been fully recrystallized, while the structures for the Al-Mg-Mn-Cr-Sc-Zr (Figure 2.20b) and Al-Mg-Sc-Zr (Figure 2.20c) have only gone through the recovery process.

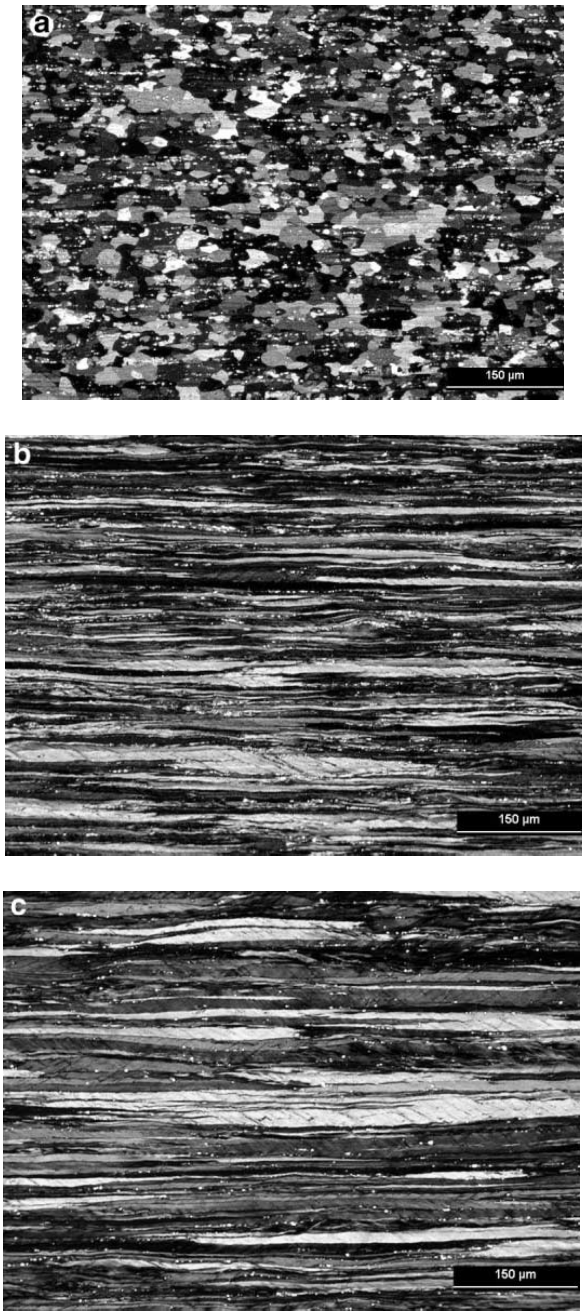

Figure 2.19: Comparison of the microstructure of three Al alloys annealed at 360°C for 12 min: (a) Al-Mg-Mn-Cr; (b) Al-Mg-Mn-Cr-Sc-Zr; (c) Al-Mg-Sc-Zr. Reproduced from ref [9].

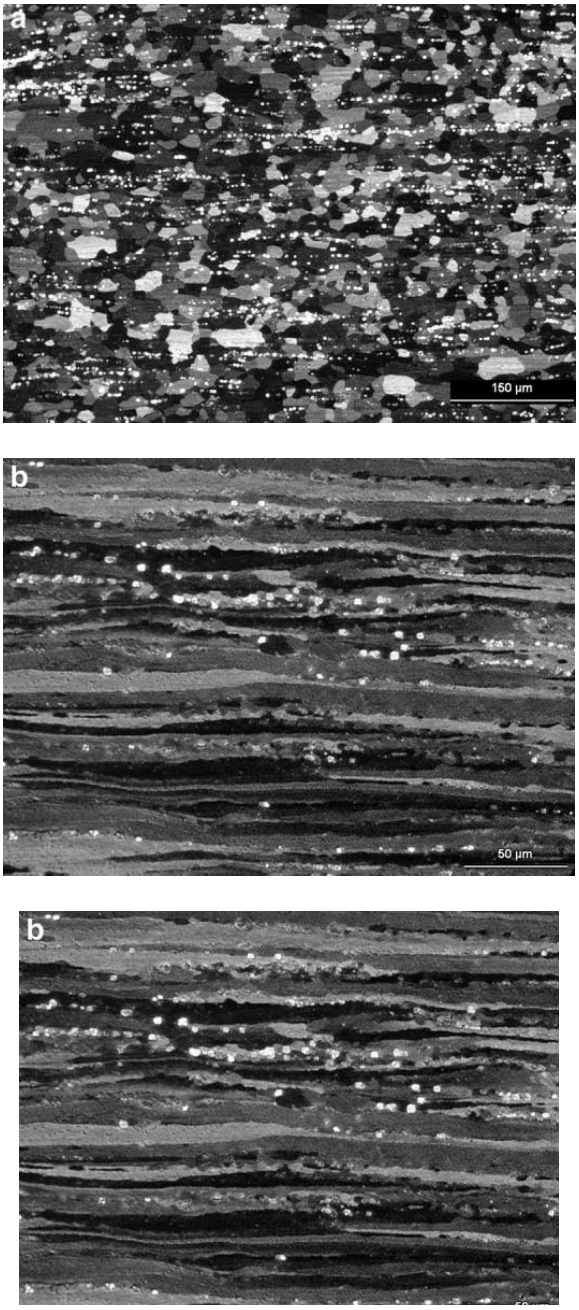

Figure 2.20: Comparison of the microstructure of three Al alloys annealed at 520°C for 6 h: (a) Al-Mg-Mn-Cr; (b) Al-Mg-Mn-Cr-Sc-Zr; (c) Al-Mg-Sc-Zr. Reproduced from ref [9].

2.1.4 *Limitations of Al_3Sc precipitation*

Although there are many benefits to the use of the Al_3Sc intermetallic compound as a hardener in Al alloys, there are some important limitations to this strengthening method.

Cost – The first major limitation is the cost because Sc is very expensive. In 2005, the Al-Sc master alloys used for the production of Sc bearing alloys were available at a price of $2000 per kg of Sc. This means that if 0.2-wt% Sc is desired in a particular alloy (which is a typical amount in many precipitation-hardened alloys) the increase in price is $4 per kg of alloy. Depending on the Al alloy, this translates to a tripling or quadrupling in price [3].

Limited Solubility – Another limitation is linked to solubility limits. The maximum solubility is only approximately 0.38-wt% Sc. This will limit the number of particles that can be formed during precipitation heat treatments, with volume fractions ranging from 0.24 – 0.71% for 0.1 – 0.3-wt% Sc bearing alloys [2]. Although Sc is said to one of the greatest strengtheners per atomic percentage, these low volume fractions do not provide to same total strengthening as other typical Al alloys precipitates [3].

Thermal Treatments – The third limitation is the processing restrictions imposed by the Al_3Sc precipitates. As mentioned in the previous section, the typical temperatures required to precipitate this compound are is in the range of 250 – 300°C. However, this becomes a major issue because traditional precipitation hardenable Al alloys are heat

treated between 150 and 200°C. A problem arises in trying to accommodate precipitation of the Al_3Sc phase and the other phases used in Al alloys such as Al_2Cu in Al-Cu alloys and Mg_2Si in Al-Mg-Si alloys [3]. The high precipitation temperature for the Al_3Sc phase will cause these other phases to over-coarsen, hence reducing their effectiveness. However, the low-temperature heat treatments used to precipitate phases like Al_2Cu and Mg_2Si is not high enough to properly disperse the Al_3Sc phase. This problem renders the use of Al_3Sc in precipitation hardenable alloys almost pointless; most commercial Sc bearing alloys are used as binary alloys or in non-precipitation hardenable systems such as Al-Mg and Al-Mn alloys.

2.2 **Alloying for BMG formation**

2.2.1 *General metallic glass formation*

The formation of a bulk metallic glass (BMG) is accomplished by suppressing the nucleation of the crystalline phase as a liquid metal is being cooled below its melting temperature. The driving force for the nucleation of the crystalline phase is a reduction in the free energy of the system, which is caused by the reduction in volume on going from the liquid to the solid state. However, metallic glasses have a lower driving force for crystalline nucleation because their change in volume from the liquid to solid state is much lower than that for other metals. The smaller change in free energy helps in the suppression of the crystalline phase and results in an amorphous metal.

Many groups have studied BMGs, but the most successful group is that led by Inoue in Japan. They have developed three empirical rules for alloys that form bulk metallic glasses; these alloys should:

1) Be multicomponent systems consisting of more than three elements.
2) Have significant differences in the atomic size ratios (above about 12%) between the main constituent elements.
3) Exhibit negative heats of mixing for the main constituent elements.

These rules are viewed as a general guide for the formation of metallic glasses and alloys produced using these three rules resulted in BMGs with high glass formability. A flow chart summarizing the key factors and mechanisms for high glass formability is shown in Figure 2.21. The idea behind these three rules is to chemically frustrate the system by: increasing the solid/liquid interfacial energy, which suppresses the nucleation of the crystalline phase; increasing the difficulty of atomic rearrangement by decreasing the diffusivity; and creating large, complex unit cells which necessitates long scale atomic rearrangement for their crystallization leading to the suppression of the crystalline phase growth [25].

Preparation Techniques – During the early development of metallic glasses, the cooling rates required to suppress the formation of the crystalline phase were so high (on the order of 10^6 K/s) that traditional casting techniques could not be used. Instead, other techniques, such as splat quenching, melt spinning and gas atomization had to be employed because these methods provided the necessary cooling rates. The experimental setup for splat quenching consisted of a cooled, curved Cu block, where droplets of the melt were dropped onto the block. This technique was later modified into a piston-anvil method, where the droplets are squeezed between a rapidly moving piston and anvil. Since the piston-anvil method provides heat extraction from two surfaces at once, the

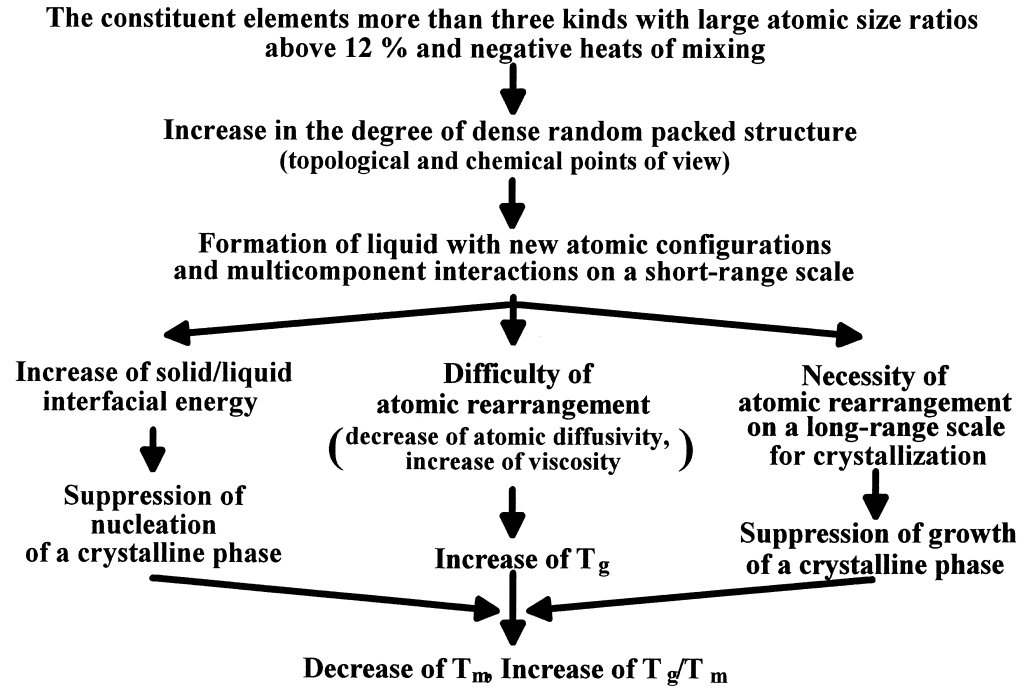

Figure 2.21: Flow chart outlining the conditions and mechanisms necessary for the development of alloys with high glass formability. Reproduced from ref [25].

critical cooling rate could be obtained in much thicker specimens. Schematic diagrams of these two techniques are shown in Figure 2.22. The melt spinning technique is different from the previous two techniques in that a cooled, large, rotating Cu disk is used as the cooling medium. The melt is held above the disk in a crucible and is ejected onto the spinning disk by a high-pressure jet of gas. A schematic diagram of the melt spinning technique is shown in Figure 2.23. The result is a continuous strip of quenched material typically a few millimeters in width and tens of microns in thickness. In gas atomization, the melt is gravity feed down through a nozzle into a chamber. At the nozzle's exit, the liquid stream is broken apart into droplets and cooled rapidly by high-pressure jets of inert gas. As the droplets cool into powder particles, they are collected at the bottom of the chamber. A schematic diagram of the gas atomization process is shown in Figure 2.24. However, for practical structural applications, components used are manufactured in sizes that far exceed the micron-sized specimens produced from the above-described techniques. The processing size limitation of BMGs has been reduced slightly over time as more complex alloys were developed that required relatively less critical cooling rates. These BMGs could be processed using the more traditional casting techniques used for crystalline metals, but the sizes of cast BMG bars obtained only ranged up to 10 cm.

Thermal treatments on these amorphous alloys resulted in very intriguing microstructures along with further improvements in properties such as tensile strength. Inoue's group published an illustrated summary, shown in Figure 2.25, of the different microstructures and associated mechanical properties for different Al alloys developed by their group. Although some of the microstructures do not contain any amorphous phases, all of these microstructures used the amorphous phase as a precursor, and the final

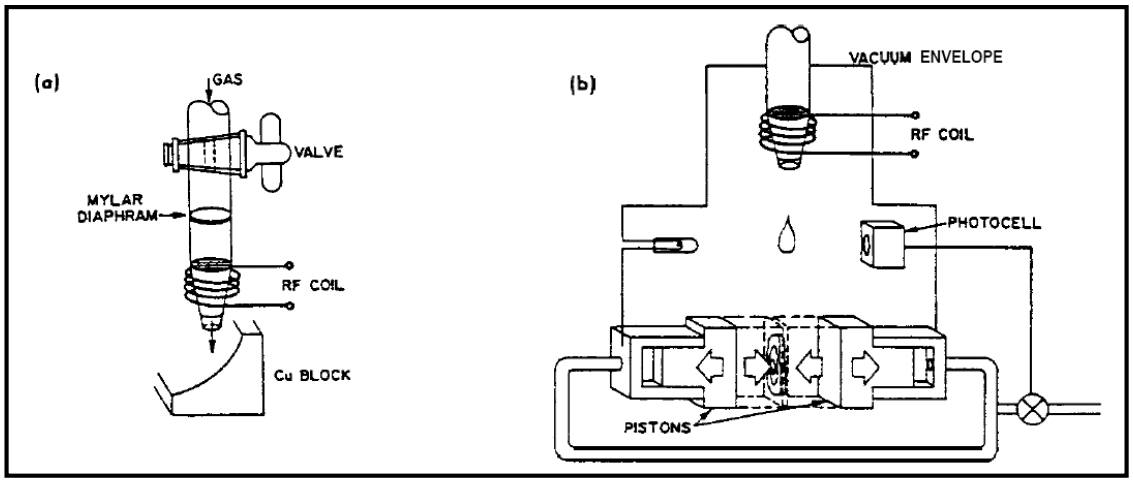

Figure 2.22: Schematic diagrams of two splat quenching arrangements: (a) molten droplets falling on to a cooled, curved Cu block; (b) molten droplets squeezed between two moving pistons. Reproduced from ref [27].

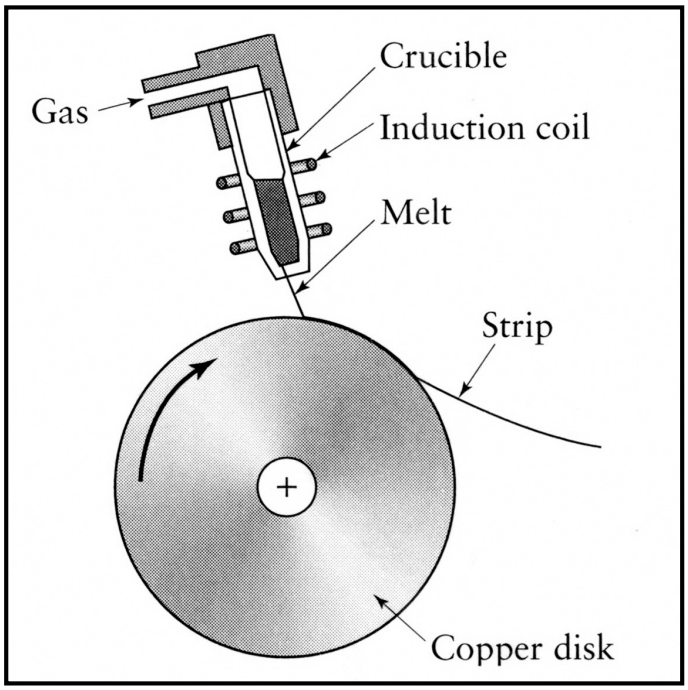

Figure 2.23: Schematic diagram of the melt spinning technique. Molten material is ejected onto a rotating, cooled Cu disk that produces a constant strip of material. Reproduced from ref [28].

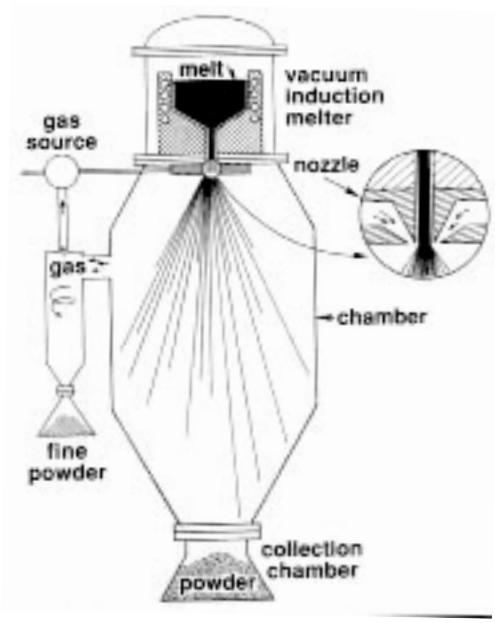

Figure 2.24: Schematic diagram of the gas atomization process. The molten material is gravity fed through a nozzle into a chamber. At the nozzle's exit jets of high pressure inert gas break up the stream into droplets that cool rapidly into powders and are collected at the bottom. Reproduced from ref [29].

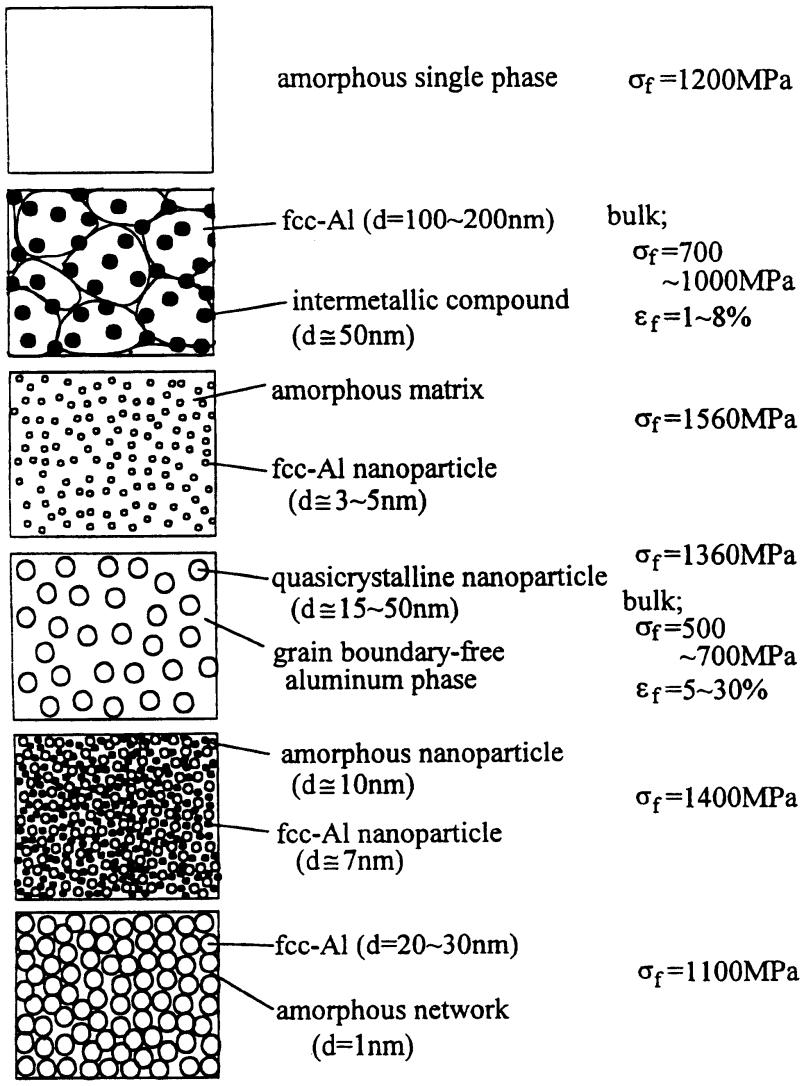

Figure 2.25: Representative images of the different types of microstructures and their corresponding mechanical properties for different Al alloys developed using the amorphous phase as a precursor. Reproduced from ref [18].

structures were obtained by controlled heat treatments. Some of these structures will be discussed in more detail.

2.2.2 *Amorphous Al alloys*

The development of amorphous Al alloys began during the mid 20th century. The first series of amorphous alloys were developed from binary alloys consisting of Al- (Si, Ge, Cu, Ni, Cr, or Pd) during the 1960s and 70s. However, these binary systems were not fully amorphous and consisted of a mixed structure of amorphous and crystalline phases. In the early 1980s fully amorphous Al alloys were produced from Al-(Fe or Co)-B and Al-Fe-(Si or Ge) ternary systems, but these alloys were extremely brittle and were not suitable for structural applications [17]. Then in the late 1980s Inoue's group began producing higher strength amorphous Al alloys such as Al-Ni-(Si or Ge), Al-Cu-V, and Al-Ni-Zr [17, 19]. These amorphous alloys exhibited tensile strengths and hardnesses as high as 800 MPa and 320 DPN, respectively which are approximately twice as high as the values achieved for conventional crystalline Al alloys aged to peak strength [17].

There are many different Al systems that have high glass formability, but the systems that have received most attention are those that are alloyed with transition metals (TM) such as: Ni, Fe & Co, and rare earths (RE) such as: Y, Ce & Gd. Such Al-TM-RE alloys can have tensile strengths as high as 1250 MPa in the amorphous state [18]. However, these amorphous materials are still very brittle with elongations to failure of approximately 1 to 2 %.

2.2.3 *Partially devitrified Al amorphous alloys*

The major advantage that amorphous Al alloys provide over conventional Al alloys is higher tensile strengths. However, further improvements were sought (especially in ductility), and it was found that partially devitrified Al amorphous alloys exhibited further improvements in mechanical properties such as tensile strength, ductility, fatigue, and wear resistance. These improvements were found to be associated with the formation of nano-scale fcc-Al particles in the amorphous matrix.

Crystallization of Amorphous alloys – There are two approaches that can be used to obtain a mixed crystalline-amorphous structure. One approach used is the precipitation of small crystals of fcc-Al in the supercooled liquid. Then the remaining liquid solidifies into the amorphous matrix. This process requires the careful control of the cooling rate during processing. Melt spinning is the method typically used for this approach. However, this process is not very reproducible because many parameters have to be controlled, such as disk rotation speed and liquid flow rate. Another approach used is to first form a fully amorphous material, and then precipitate the fcc-Al crystals in the amorphous matrix by controlled heat treatments [19]. This second approach gives much better control and reproducibility over the precipitation of the nano-crystals and is the most widely used.

The crystallization of amorphous alloys occurs in several stages. Initial crystallization stages typically include the formation of fcc-Al nano-crystals within the amorphous matrix. The intermediate crystallization stages include the formation of several different stable and metastable intermetallic phases, along with coarsening of the

fcc-Al crystals. Complete crystallization of the amorphous structure is seen after the last stage, which consists of fcc-Al grains, the stable intermetallics formed in previous stages, and a new intermetallic phase that forms during the last stage. For example, for Al-Ni-Y alloys, the first transformation to take place is the formation of nano-particles of fcc-Al. With continued heating, stable (and metastable) binary intermetallics form during the intermediate stages, and the final stage results in a fully crystalline microstructure consisting mainly of fcc-Al grains and a ternary intermetallic phase, while the binary intermetallic is the minority phase. Other alloys have shown other trends, such as $Al_{87}Ni_7La_6$ and $Al_{87}Ni_7Ce_6$, which do not form nano fcc-Al particles but rather form metastable intermetallics during the crystallization stages [20]. The next two sections will discuss the effects of these mixed structures on the mechanical properties.

Effects of nano-scale particles on Mechanical Properties – The formation of these nano-scale fcc-Al particles has been shown to have a positive effect on the mechanical properties of amorphous materials. Fully amorphous alloys have tensile strengths as high as 1250 MPa. However, the precipitation of these nano-scale particles inside an amorphous matrix further increases their strengths. Choi et al produced partially devitrified $Al_{88}Ni_{10}Nd_2$, $Al_{88}Ni_9Nd_2Fe_1$, $Al_{88}Ni_{10}Gd_2$, and $Al_{88}Ni_9Gd_2Fe_1$ alloys with tensile strengths greater than 1500 MPa, where $Al_{88}Ni_{10}Nd_2$ achieved a maximum strength of 1980 MPa [21]. A plot of the effect of aging temperature on the tensile strength and elongation at fracture is shown in Figure 2.26. The microstructures of all four alloys contained fcc-Al particles approximately 10 nm in diameter. It is clear that there was a vast improvement in strength at an aging temperature between 400 and 480

K. For $Al_{88}Ni_{10}Nd_2$ alloy, plots of the micro-hardness, fracture strength, and fracture elongation versus volume fraction of fcc-Al particles are shown in Figure 2.27. This figure shows that peak strength and ductility was achieved with a volume fraction of 18%, while the hardness continues to increase with volume fraction. The other three alloys also exhibited peak properties at volume fractions of 18%. In addition, fracture elongation improved with the precipitation of these particles, where a 50% improvement in ductility can be seen in Figure 2.26 at the peak aging temperature [21].

Other studies also showed improvements in the hardness of partially devitrified alloys with increasing volume fractions of the fcc-Al particles. Rizzi and Battezzati performed microhardness measurements on three different alloys, $Al_{87}Ni_7Nd_6$, $Al_{87}Ni_7La_6$, and $Al_{87}Ni_7Ce_6$, aged at different temperatures up to 550°. The changes in microhardness as a function of aging temperature for these three alloys is shown in Figure 2.28. As these alloys are aged, crystalline phases begin to form in the amorphous matrix, and these plots show that a general increase in hardness is achieved with an amorphous-crystalline mixed structure [20]. Also, the $Al_{87}Ni_7Nd_6$ alloy shows the greatest improvement in micro-hardness. Recall that the partially devitrified microstructures of $Al_{87}Ni_7La_6$, and $Al_{87}Ni_7Ce_6$ alloys do not contain nano fcc-Al particles but rather contain metastable intermetallics. On the other hand, the $Al_{87}Ni_7Nd_6$ alloy does contain nano fcc-Al particles, which is linked to the difference in hardness. (Proposed mechanisms for improvements are discussed in the next section.)

Inoue et al have shown that materials with this mixed microstructure have better elevated temperature tensile strength than fully amorphous alloys. For example, Figure 2.29 shows plots of the tensile strength and fracture elongation versus testing temperature

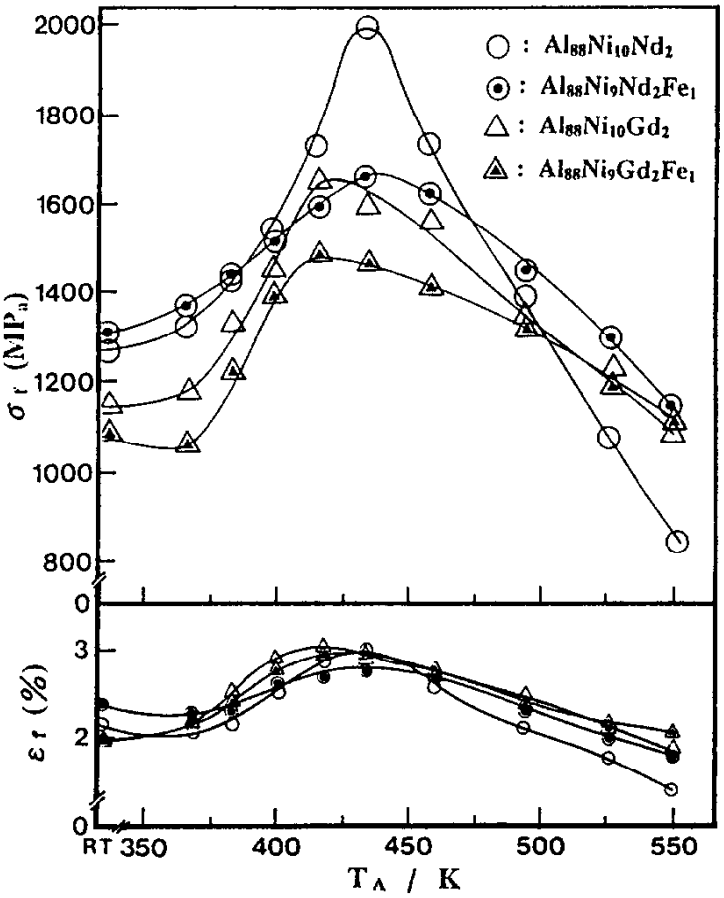

Figure 2.26: Aging temperature dependence of tensile fracture strength and fracture elongation in partially devitrified Al alloys. Reproduced from ref [21].

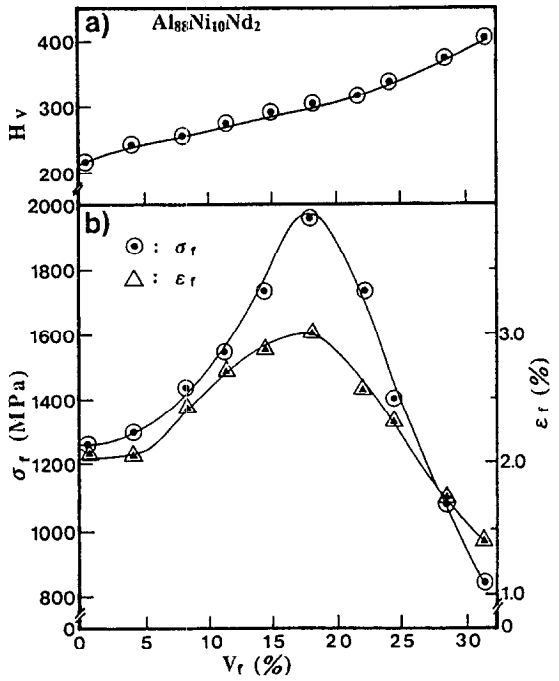

Figure 2.27: Changes in (a) micro hardness and (b) fracture strength and fracture elongation as a function of volume fraction of nano fcc particles in $AlNi_{10}Nd_2$. Reproduced from ref [21].

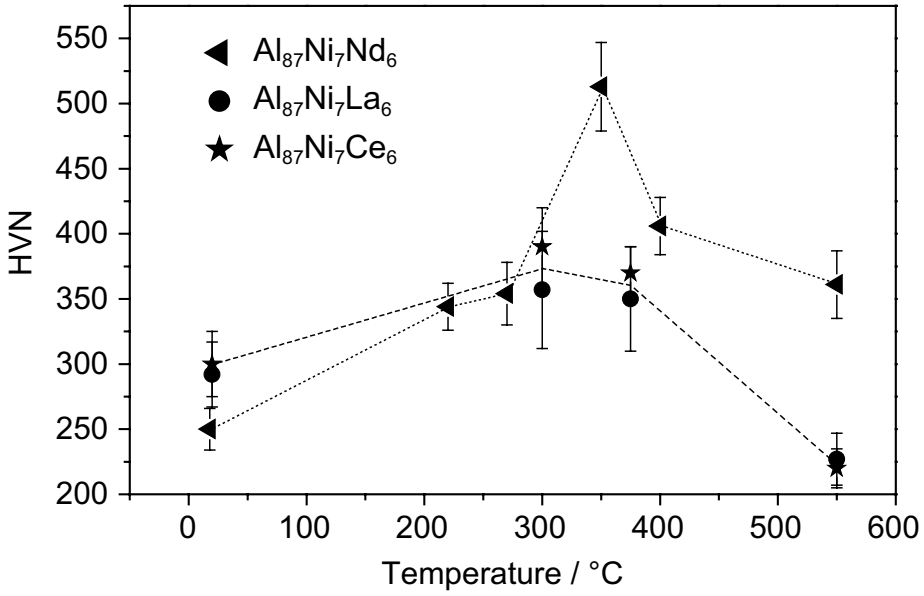

Figure 2.28: Changes in micro hardness as a function of aging temperature for three alloys: $Al_{87}Ni_7Nd_6$, $Al_{87}Ni_7La_6$, and $Al_{87}Ni_7Ce_6$. Reproduced from ref [20].

for an $Al_{88}Ni_{10}Nd_2$ alloy in the amorphous state and with 8% volume fraction of fcc-Al nano-particles [21]. The fully amorphous alloy exhibits an interesting variation in strength. It has a sharp decrease from 1200 MPa to 960 MPa at 390 K, followed by a sharp increase, and then gradually decreases with temperature. The crystallization temperature of the alloy is 403 K, which is close to the temperature where the strength irregularity occurs. The authors explain that the decrease in strength is due to a weakening in the bonding force among the atoms before crystallization. The increase in strength that follows is due to the dispersion of the fcc-Al particles. On the other hand, the same alloy with an 8% volume fraction of the fcc-Al phase exhibited better properties with a continuous decrease in strength from 1450 MPa at 400 K to 960 MPa at 600 K [21]. Another alloy developed by Inoue's group that exhibited enhanced elevated temperature strength was $Al_{88}Ni_9Ce_2Fe_1$, which had a 20% volume fraction of fcc-Al particles and maintained a tensile strength of 960 MPa at 600 K [24]. The elevated temperature strength of these amorphous alloys is 15 times greater than those exhibited by conventional, precipitation hardened Al alloys.

These mixed structures also have other improved properties such as compressive strength and wear resistance. A plot of wear resistance versus micro-hardness is shown in Figure 2.30, where different Al alloys are compared. The data shows that the hardness and wear resistance of the mixed amorphous-crystalline materials (labeled as nanophase composites) are superior to those of conventionally hardened Al alloys and early fully amorphous Al alloys [22].

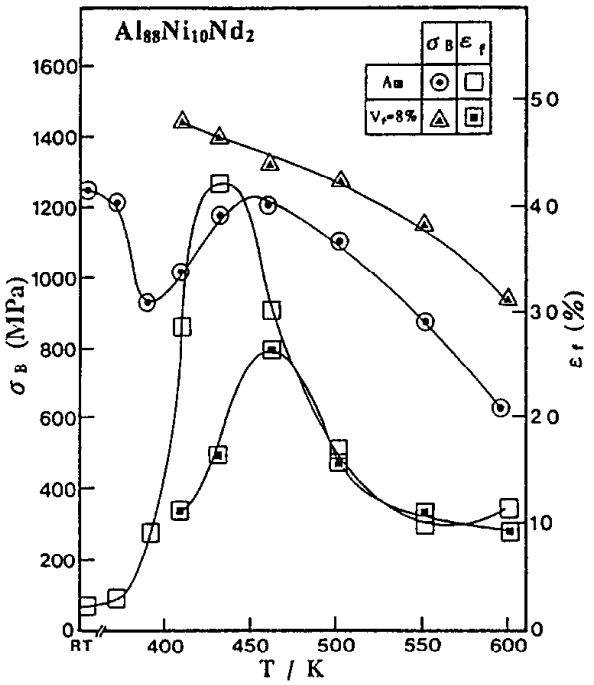

Figure 2.29: Tensile strength and fracture elongation as a function of testing temperature for an $Al_{88}Ni_{10}Nd_2$ alloy in the amorphous state and with 8% v_f of fcc-Al nano-particles. Reproduced from ref [21].

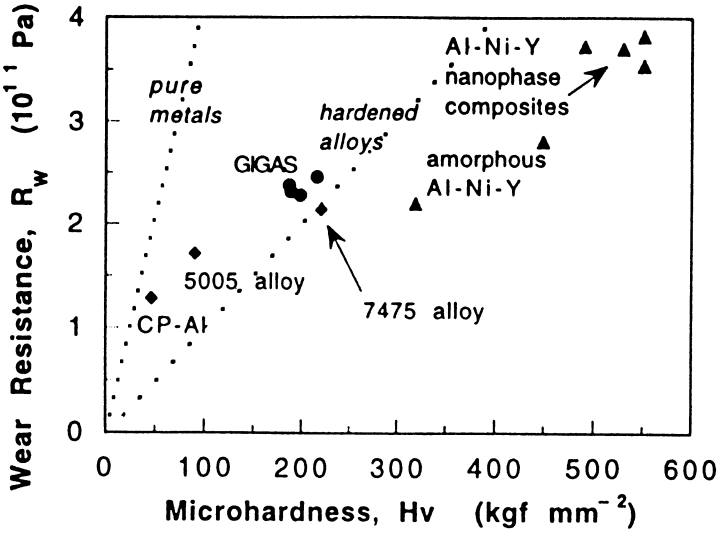

Figure 2.30: Plot of the wear resistance as function of micro-hardness of various Al alloys. Reproduced from ref [22].

Proposed mechanisms for improved mechanical properties – One proposed mechanism was that since the fcc-Al particles were so small that they were defect free and extremely strong. Therefore, these hard particles would act as strong barriers to deformation in the material. However, this is not believed to be the dominant mechanism because optimum strengths are obtained for particles coarsened to about 10-15 nm in diameter at a volume fraction of 20%. In addition, if these defect free particles were the main cause of strengthening, then a higher volume fraction should result in higher strengths, but the opposite trend is seen where volume fractions greater than 20% actually result in lower strengths and much more brittle materials. Kim et al proposed another strengthening mechanism using the Al-Ni-Y system as a model, which is the minority element enrichment of the amorphous matrix. As the fcc-Al particles form, the other elements are rejected into the surrounding amorphous matrix. As the fcc nano-particles form and reject Ni and Y, the Ni atoms diffuse very rapidly and are distributed homogenously in the amorphous matrix whereas the Y atoms diffuse much more slowly and tend to accumulate near the particle-matrix interface. As the local concentration of Ni and Y exceeds 20% these regions become brittle and act as nucleation sites for cracks. These results are in good agreement with results obtained for fully amorphous alloys wherein if the bulk minority elements composition exceeds 20% the materials become very brittle [23].

Although these partially devitrified alloys exhibit enhanced mechanical properties in comparison to traditional Al alloys, the biggest drawback is their extremely low ductility. Even though the precipitation of fcc-Al particles helps to improve ductility, these alloys only have elongations to fracture of 3%. Also, these materials require such

high cooling rates that the maximum thickness of samples produced with an amorphous structure is limited to a few millimeters. These sizes are not suitable for practical structural applications. However, a compromise between strength and ductility was found by subsequent heat treatments to fully convert the material from the amorphous state to crystalline.

2.2.4 *Fully devitrified amorphous Al alloys*

With sufficient heating, amorphous Al alloys can be fully devitrified into a crystalline material. In the crystalline state, these alloys exhibited much higher fracture elongations, but at the cost of slightly lower strengths. However, their strengths are still better than conventional Al alloys. A schematic microstructure of a devitrified alloy is shown in Figure 2.25. These structures consist of fine fcc-Al grains and a high volume fraction of intermetallic compounds.

The development of high strength Al alloys through the devitrification of the amorphous state has been the focus of a Defense Advanced Research Projects Agency (DARPA) funded project called the Structural Amorphous Materials (SAM) program. The gas turbine engine company Pratt & Whitney is leading the SAM program. The alloys of interest have been Al-RE-TM systems. The processing approach used to produce these materials is powder metallurgy. The powder is formed using gas atomization, which provides the necessary cooling rates to form fully amorphous powder. Subsequent canning and extrusion consolidates the powder and fully devitrifies the amorphous structure into a bulk crystalline material. (A more detailed description of the processing of these alloys is given in Chapter 3).

Al-RE-TM microstructures – In these Al alloys, Rare earth metals like Y and Gd were used, and Transition metals used were Ni, Fe, and Co. Al-RE-TM alloys with compositions such as Al-Y-Ni, Al-Gd-Ni, Al-Y-Gd-Ni-Fe-Co, and Al-Ni-Y-(Fe, Co) were studied by Vasiliev et al [30-33]. The microstructures that form after full devitrification of these alloys are generally similar to one another and are composed of three main features: fcc-Al grains, binary phase, and a ternary phase; representative TEM images are shown in Figure 2.31. The matrix consists of fcc-Al grains with sizes ranging from 100 to 600 nm in diameter [30]. The binary phase typically has an equiaxed morphology and its size ranges from 50 to 500 nm. The binary phase that forms is dependent on alloy composition. Vasiliev et al studied four Al-Y-Ni alloys: Al-2.6Y-9.5Ni, Al-4.5Y-10.1Ni, Al-1.7Y-6.4Ni, and Al-4.3Y-3.5Ni (all in at%), and reported that the binary phase in the first three alloys was the Al_3Ni with the Fe_3C (Pnma) structure while the fourth alloy contained the Al_3Y phase which adopted the Pb_3Ba ($R\bar{3}m$) structure. TEM image, EDS, and diffraction analyses on the Al_3Ni and Al_3Y particles are shown in Figures 2.32 and 2.33, respectively [30]. However, the binary phases were the minority microstructural feature.

From the overall microstructures shown in the Figure 2.31, the majority of the particles are the ternary phase. The ternary phase appears to exhibit two different morphologies: equiaxed and rod-like, as shown in Figure 2.34. However, the ternary particles are actually plate shaped, so if they are viewed from the top the particles appear equiaxed and when viewed edge-on they appear as rods. The ternary phase was initially reported to be the $Al_{16}Ni_3Y$ by Rykhal and Zarechnyuk, with other groups also claiming to have observed this phase [34-37]. However, only the symmetry and lattice parameters

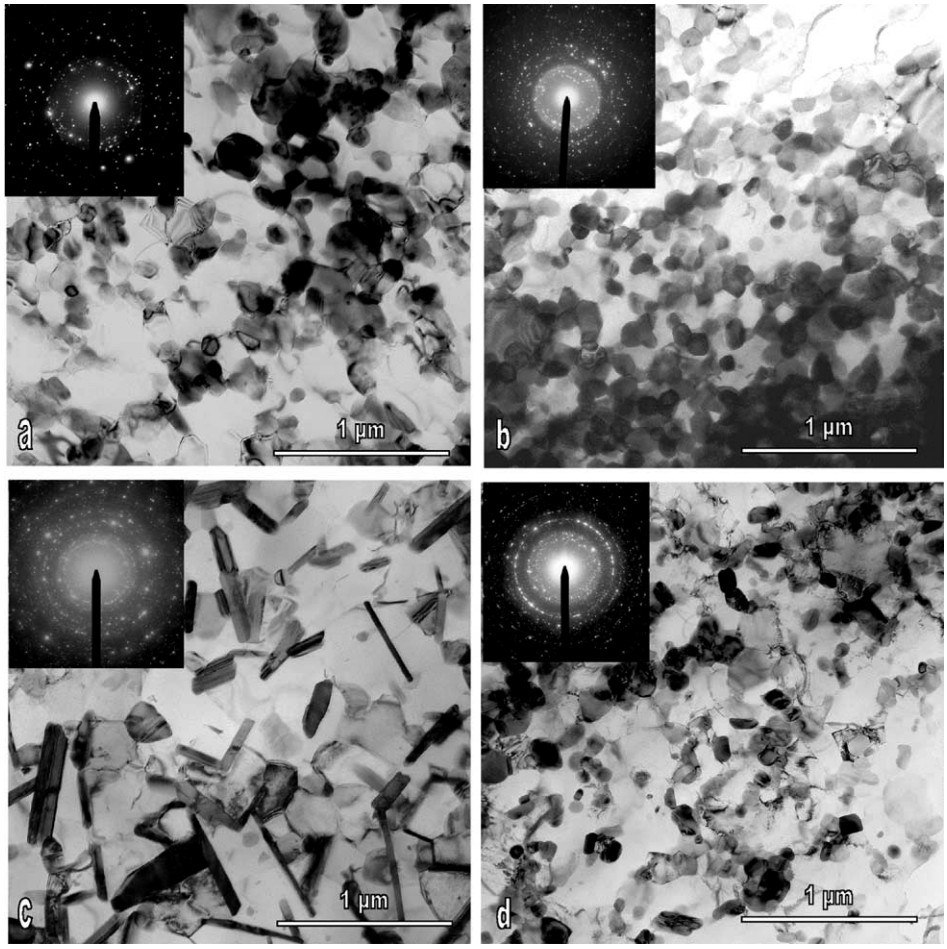

Figure 2.31: Bright field TEM images with inset SADPs showing the overall microstructures for: (a) Al-2.6Y-9.5Ni; (b) Al-4.5Y-10.1Ni; (c) Al-4.3Y-3.5Ni; and (d) Al-1.7Y-6.4Ni (all in at %). Reproduced from ref [30].

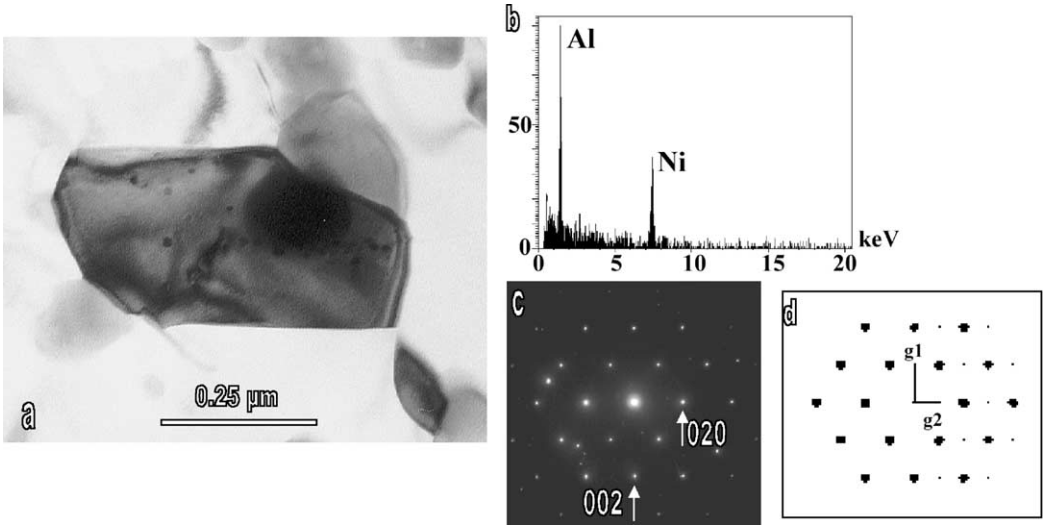

Figure 2.32: Analysis of an Al_3Ni particle: (a) bright field TEM image, (b) EDS spectrum, (c) SADP obtained at the [001] zone axis, and (d) simulation of diffraction pattern at the same orientation. Reproduced from ref [30].

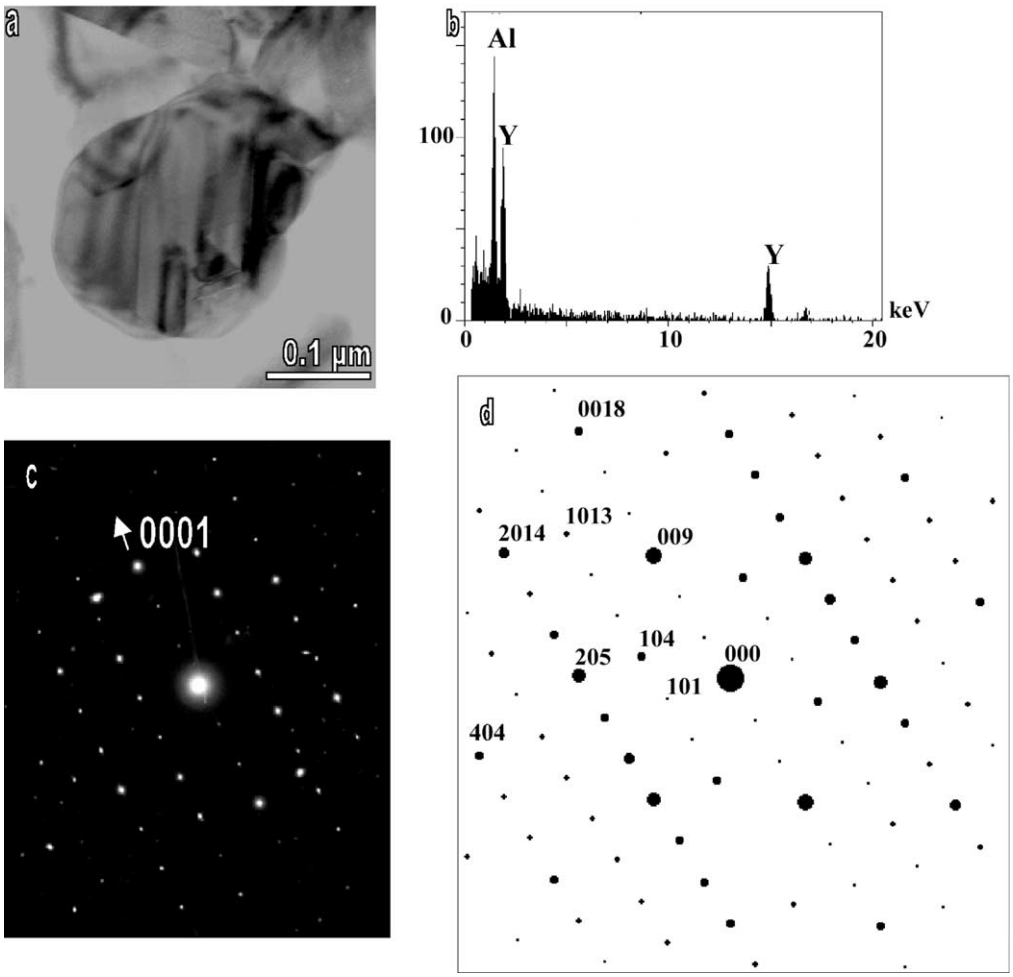

Figure 2.33: Analysis of an Al_3Y particle: (a) bright field TEM image, (b) EDS spectrum, (c) SADP obtained at the [-1-120] zone axis, and (d) simulation of diffraction pattern at the same orientation. Reproduced from ref [30].

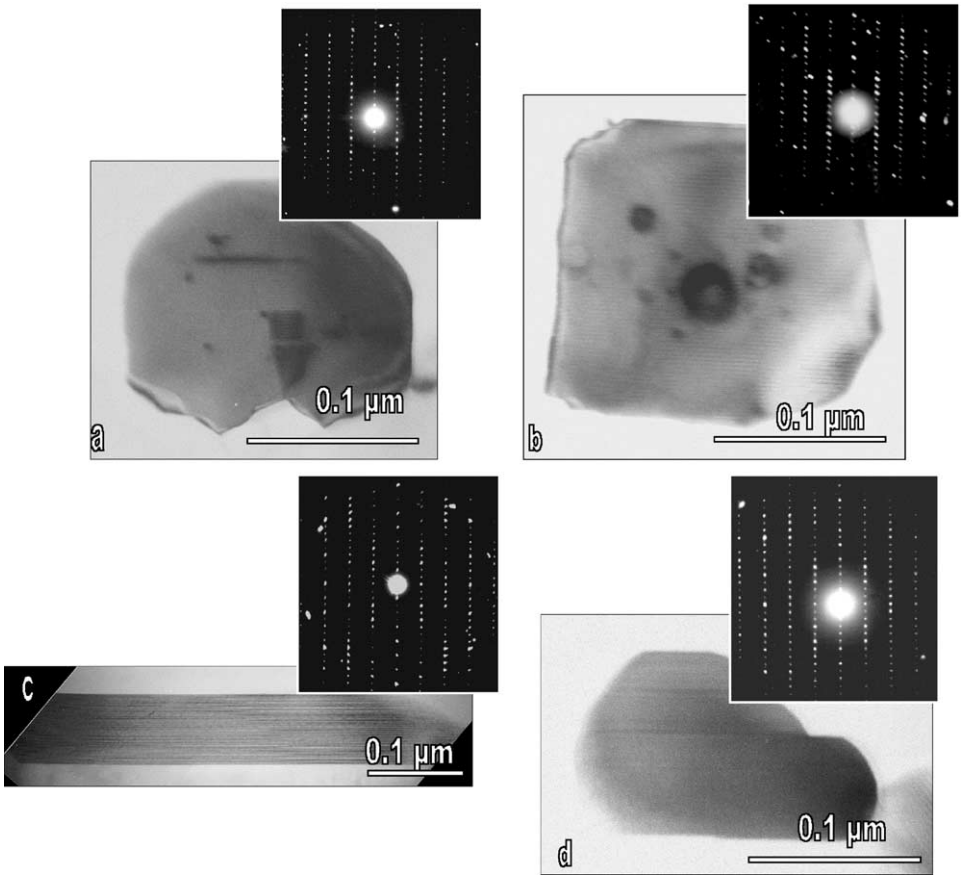

Figure 2.34: Bright field TEM micrographs with inset SADPs obtained of the ternary phase present in: (a) Al-2.6Y-9.5Ni; (b) Al-4.5Y-10.1Ni; (c) Al-4.3Y-3.5Ni; and (d) Al-1.7Y-6.4Ni (all in at %). Reproduced from ref [30].

were reported. Raggio et al performed an extensive study on the phases formed in a series of ternary Al alloys subjected to long-term heat treatments and compared their data to the results reported by others in the literature. They did not observe the $Al_{16}Ni_3Y$ phase in any of their experiments and discounted it as an equilibrium compound [38]. Vasiliev et al performed a detailed TEM analysis on the ternary phase. Using diffraction data, HRTEM, and computer simulations they determined that the ternary phase did not correspond to any known equilibrium phases, but instead was $Al_{19}Ni_5Y_3$, which adopted the orthorhombic $Al_{19}Ni_5Gd_3$ type structure [30].

Similar results were also obtained from an Al-8Ni-7Gd (in at%) alloy [31]. In this case, the rare earth element Y was replaced with Gd, but the microstructure and the phases present are analogous to those observed in Al-Ni-Y systems. The bright field TEM image in Figure 2.35 shows the microstructure the Al-8Ni-7Gd alloy: fcc-Al grains, the equiaxed binary phase Al_3Gd, and the plate-shaped ternary phase [31].

Microstructural stability – The microstructures of these alloys appear to be very stable. Magdefrau et al studied the effect of heat treatment on the microstructure of an Al-3Y-3Gd-5Ni-1Fe-1Co (at%) alloy [32]. Figure 2.36 is a bright field TEM image of the initial microstructure which exhibits the same features as the other alloys: fcc-Al grains, binary particles of $Al_3(Y,Gd)$ and ternary particles of $Al_{19}(Ni,Fe)_5(Y,Gd)_3$. The heat-treated samples contained the same phases and morphologies and were only coarsened versions of the initial microstructure. TEM images of this alloy heat-treated for 5 h at 450°C and 550°C are shown in Figure 2.37 [32]. A summary of the particle dimensions in the as extruded and heat treated samples is shown in Table 2.1. Taking into consideration the

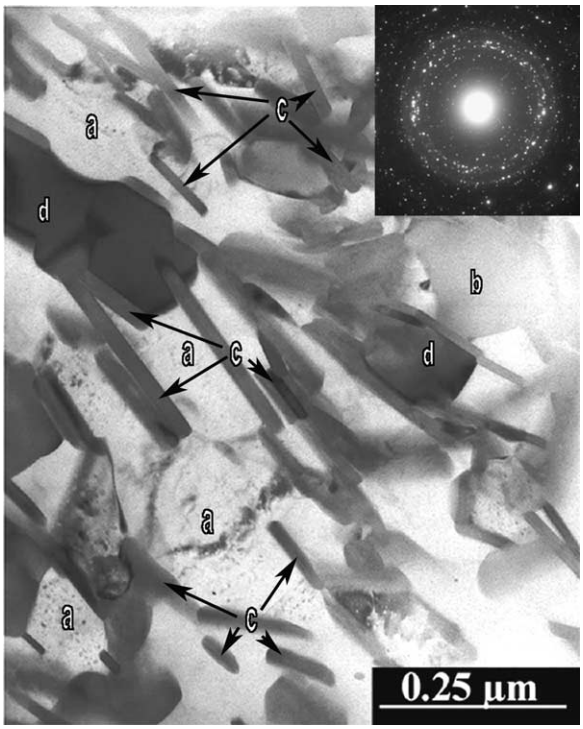

Figure 2.35: Bright field TEM image of the overall microstructure in an Al-Ni-Gd alloy with examples of phases indicated: (a) fcc-Al grains; (b) equiaxed Al_3Gd particles; (c) rod-like ternary particles; (d) equiaxed ternary particles. Reproduced from ref [31].

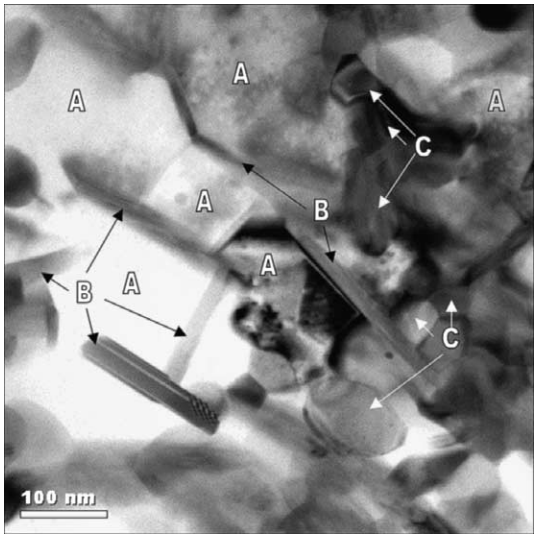

Figure 2.36: Bright field TEM image of the initial microstructure in an Al-3Y-3Gd-5Ni-1Fe-1Co (at%) alloy with the three main phases indicated: (a) fcc-Al grains; (b) ternary particles $Al_{19}(Ni,Fe)_5(Y,Gd)_3$; (c) binary particles $Al_3(Y,Gd)$. Reproduced from ref [32].

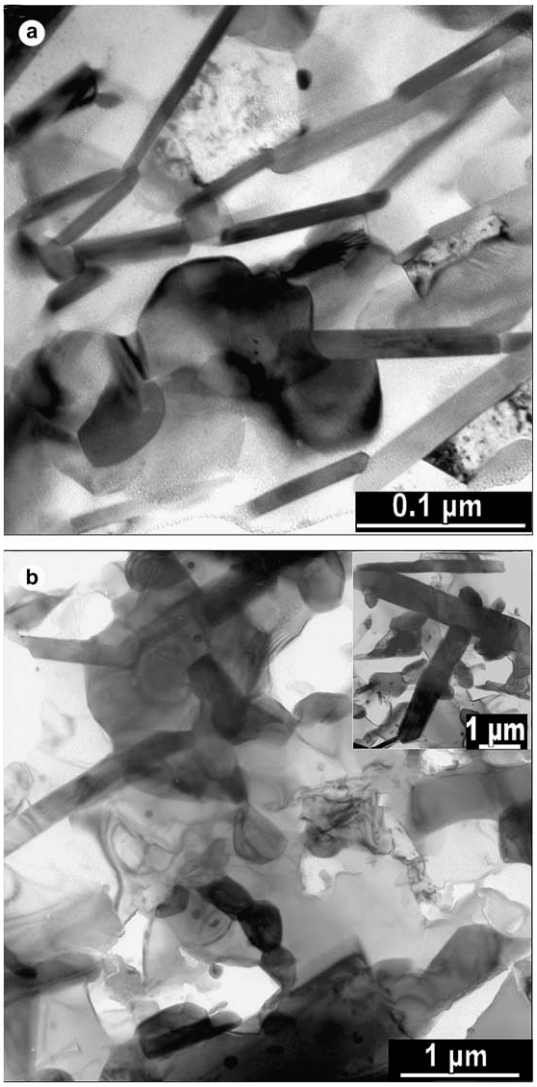

Figure 2.37: Bright field TEM images of the microstructures exhibited by Al-3Y-3Gd-5Ni-1Fe-1Co (at. %) samples heat-treated for 5 h at: (a) 450 °C; (b) 550 °C. Reproduced from ref [32].

high homologous temperatures used for heat-treating, the particles coarsen very slowly. In addition, Table 2.2 shows the results of a detailed statistical analysis performed on the variation of the lengths and widths of the rod-like ternary phase in samples heat-treated at various temperatures between 400 and 550°C for 5 h. Although the sizes of the rod increase by an order of magnitude after the 550°C heat treatment, the aspect ratio for the rods remains constant at ~6 in all the samples studied. These results suggest that this is the equilibrium morphology for these particles [32].

Microstructure/Mechanical Properties relation – Magdefrau et al also studied the effect of these heat-treatments on the material's micro-hardness [32]. The initial hardness for the as-extruded sample was 303 H_V. They then obtained micro-hardness measurements from samples heat-treated between 400 and 550°C for 0.5, 2.5 and 5 h. A plot of the variation of hardness with temperature and time is shown in Figure 3.28 [32]. The plots show that there was an initial sharp decrease at each temperature, followed by a gradual decrease with prolonged exposure. In addition, they looked at the relationship between the hardness and ternary phase particle size and found that there is a strong linear correlation, which is shown in Figure 2.39. For typical metals the movement of dislocations causes plastic deformation. However, if dislocations come across any obstacles (e.g. precipitate particles) they will be forced to either cut through or loop around the particles. This disruption to dislocation movement leads to strengthening/hardening of metals by mechanisms such as Orowan or Hall-Petch type strengthening. For a constant volume fraction and fixed aspect ratio of particles, the inter-particle separation, λ, is directly proportional to the particle dimensions. In Orowan

Phase	Morphology	Particle dimensions (nm)		
		AR	400 °C	550 °C
Al/FCC	Equi-axed	100–500	100–500	200–2000
$Al_{19}(Ni,Fe)_5(Y,Gd)_3$/$Al_{19}Ni_5Gd_3$-type	Rod-like	100–500 (*L*) 20–80 (*W*)	100–500 (*L*) 20–50 (*W*)	300–3000 (*L*) 100–300 (*W*)
$Al_3(Y,Gd)$/Ni_3Sn-type	Equi-axed	20–100	50–200	50–600

Table 2.1: Summary of the dimensions of the three main phases present in an Al-3Y-3Gd-5Ni-1Fe-1Co (at%) alloy in the as-extruded sample and in samples heat treated for 5 h at 400 and 550°C. Reproduced from ref [32].

T (°C)	400	450	475	500	525	550
L (nm)	299	491	967	1709	1628	2179
W (nm)	39	85	165	263	272	368

Table 2.2: Summary of the lengths and widths of the rod-like ternary phase, $Al_{19}(Ni,Fe)_5(Y,Gd)_3$, in Al-3Y-3Gd-5Ni-1Fe-1Co (at%) samples heat treated for 5 h between 400 and 550°C. Reproduced from ref [32].

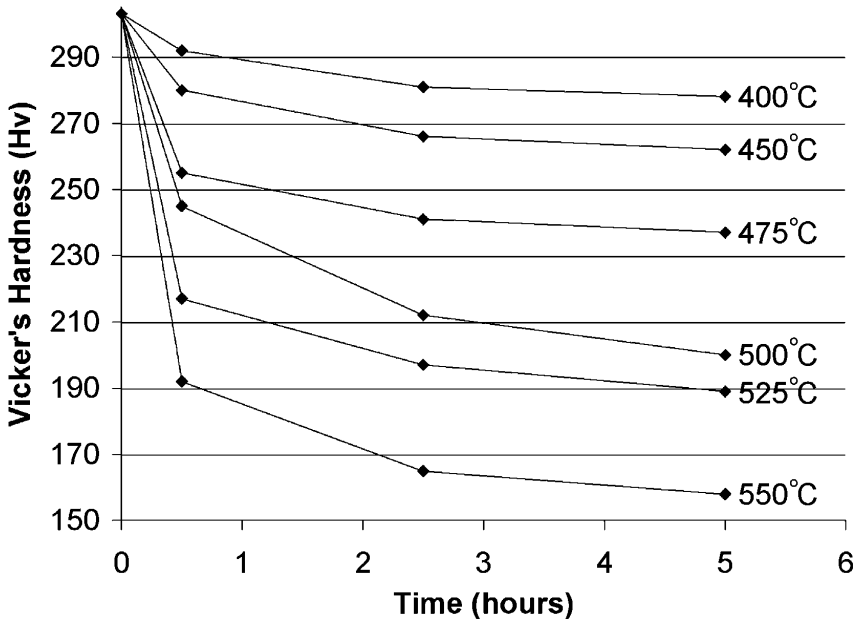

Figure 2.38: Plots of the hardness taken from Al-3Y-3Gd-5Ni-1Fe-1Co (at%) alloys heat-treated at various temperatures and times. Reproduced from ref [32].

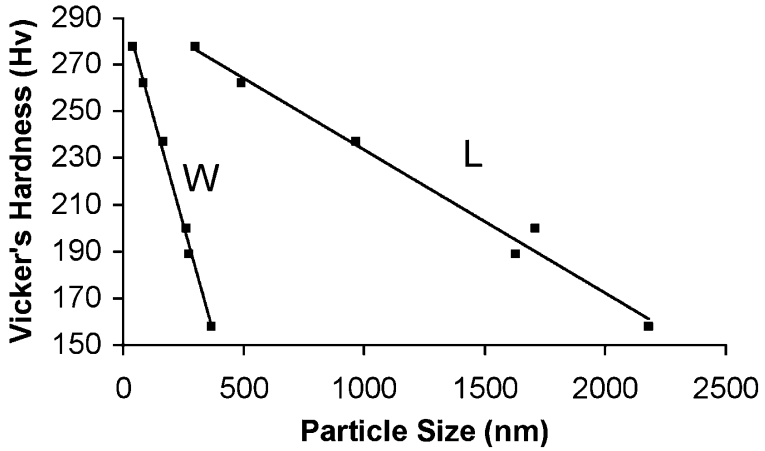

Figure 2.39: Plots of the variation in hardness with the length and width of the rod-like $Al_{19}(Ni,Fe)_5(Y,Gd)_3$ particles in an Al-3Y-3Gd-5Ni-1Fe-1Co (at%) alloy. Reproduced from ref [32].

and Hall-Petch strengthening, the material hardness should be inversely proportional to λ and λ^2, respectively. Recall that the data in Figure 2.39 shows a linear relationship between hardness and particle size. Since these results are not consistent with those expected from Orowan and Hall-Petch strengthening, it implies that dislocation/particle interactions are not the controlling factor, especially in systems where the particle sizes are on the same order of magnitude as the Al grains. Further work is being done to analyze these alloys as short fiber reinforced metal matrix composite [32].

Chapter 3: Materials and Experimental Methods

3.1 Materials

3.2 Experimental Methods and Characterization

3.2.1 *X-Ray Diffraction (XRD)*

3.2.2 *Scanning electron microscopy (SEM)*

3.2.3 *Transmission electron microscopy (TEM)*

3.2.4 *Focused Ion Beam (FIB) and Serial sectioning*

3.2.5 *Amira 3D reconstruction*

Chapter 3: Materials and Experimental Methods

For this study, electron microscopy techniques were used to characterize the microstructural changes that occurred after different levels of forging upset on an extruded Al-Ni-Y-Co alloy. High-resolution characterization was performed by scanning electron microscopy (SEM) and transmission electron microscopy (TEM). Focused ion beam techniques were used for serial sectioning, while SEM was used to collect the series of cross section images. The software package used for the three-dimensional reconstructions of the image stacks was the Resolve RT 5 – FEI edition of Amira.

3.1 Materials

The gas turbine engine company, Pratt & Whitney, provided the Al alloy used in this study, which had a nominal composition of Al – 11Ni – 13Y – 1Co (in wt%). Powder metallurgy techniques were used in the production of this alloy. A schematic of the sequence of processing techniques used to produce this alloy is shown in Figure 3.1. For the gas atomization process, a master alloy is cast with the appropriate composition. The master alloy is melted in a vacuum furnace that lies above an atomization chamber. The melt is then gravity fed through a nozzle where at the nozzle's exit high-pressure jets of inert gas spray the melt into the chamber. The high-pressure jets of gas force the liquid metal stream to break up into small droplets that cool rapidly into powder particles. The cooling rates achieved in gas atomization can be high enough to give a fully amorphous structure in the powder. The particles fall and are collected at the bottom of the chamber. The powder particles were then compacted and sealed inside pure Al cans. The sealed Al cans are then ram extruded at elevated temperature, which provides the

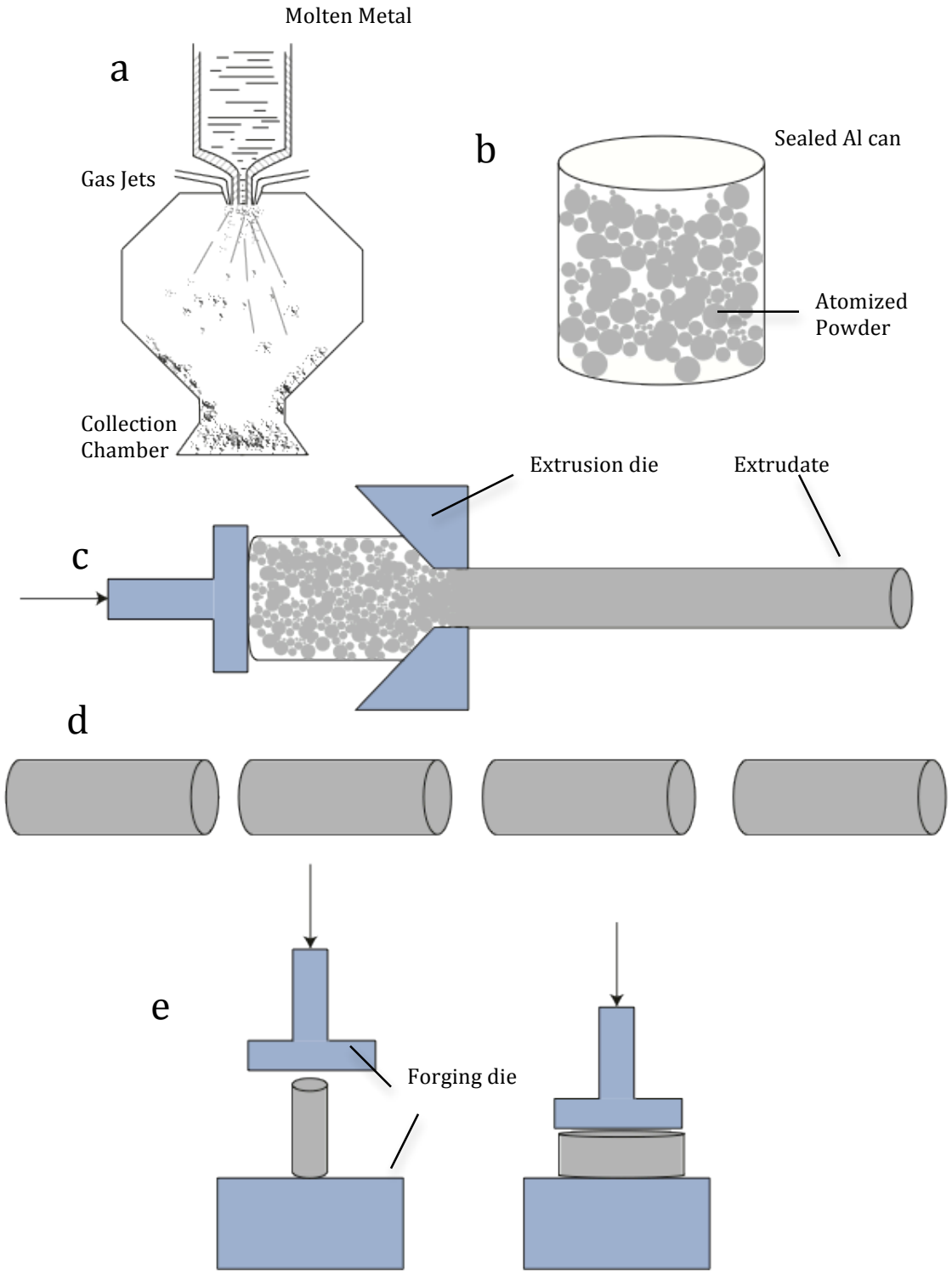

Figure 3.1: Schematic of the sequence of processing techniques used to produce the Al-Ni-Y-Co alloy. (a) Gas atomization of master alloy into amorphous powders. (b) Powders compacted and sealed into Al cans. (c) Cans are then ram extruded at high pressure and temperature to consolidate and devitrify the amorphous powders. (d) Bar is cut perpendicular to the extrusion direction into smaller sections. (e) Smaller sections are forged parallel to the extrusion direction.

final processing conditions to consolidate and fully devitrify the amorphous powder. The extruded bars were then de-canned to remove the outer Al can layer. The bar was then cut into smaller sections perpendicular to the extrusion direction. These smaller sections were forged parallel to the extrusion direction to three different upsets: 43%, 64%, and 84%. The microstructure of the as extruded alloy and the alloy samples forged to upsets of 43%, 64%, and 84% were analyzed.

3.2 **Experimental Methods and Characterization**

3.2.1 *X-Ray Diffraction (XRD)*

X-ray diffraction patterns were obtained from sections cut perpendicular to the extrusion direction using a Bruker D5005 X-ray diffractometer. The specimens were scanned over a 2θ range of 20 - 80° with a step size of 0.02° for 4 hours. The peaks from FCC Al were identified and the remaining peaks were assigned to the $Al_{19}Ni_5Y_3$ phase. Since there is no JCPDS standard for this latter phase, the peaks were indexed as follows. Firstly the software EVA was used to tabulate the d-spacings corresponding to each of the peaks observed in the spectrum apart from those belonging to FCC Al. These d-spacings were then compared to those expected from an orthorhombic $Al_{19}Ni_5Y_3$ crystal with the structure defined by Vasiliev et al and labeled accordingly [30].

3.2.2 *Scanning electron microscopy (SEM)*

Samples for SEM were prepared using standard metallographic techniques. Thin slices were cut parallel to the extrusion direction of the material. These slices were ground mechanically starting with 240 grit paper and working down to 1200 grit paper

using only distilled water as a lubricant. Final polishing was performed using a 0.3 μm Alumina suspension. During preliminary experiments, severe sample drift was observed. Therefore, holes were drilled through the samples and the SEM stubs, the holes were tapped, and the samples were mechanically clamped to the stubs by small screws. A sample mounted in this manner is shown in Figure 3.2. Furthermore, the orientation of the clamped slice relative to the bar is shown in Figure 3.2, in which the vertical axis is parallel to the extrusion direction.

SEM images were acquired using the electron column on a FEI Dual Beam Strata 400S system, which has a Schottky field emission gun and was operated at an accelerating voltage of 3 kV for optimum resolution. The detector used was the high-resolution through-the-lens detector (TLD) in either free-field or immersion mode, for secondary electron (SE) or backscattered electron (BSE) imaging.

3.2.3 *Transmission electron microscopy (TEM)*

TEM samples were initially prepared by cutting thin slices of material in two different orientations: parallel and perpendicular to the extrusion direction. These slices were further thinned by mechanically grinding to below 0.1 mm in thickness. A disk punch was then used to extract 3 mm diameter disks from these thin sheets. The disks were then thinned to perforation in a Struers Tenupol-5 twin jet electropolisher using an electrolyte consisting of 70% Butanol, 20% Perchloric Acid, 10% at approximately -20°C and 20 V.

TEM analysis was performed using a FEI T12 Tecnai S/TEM operated at 120 kV. This instrument is equipped with an ultra-thin window EDAX energy dispersive X-ray

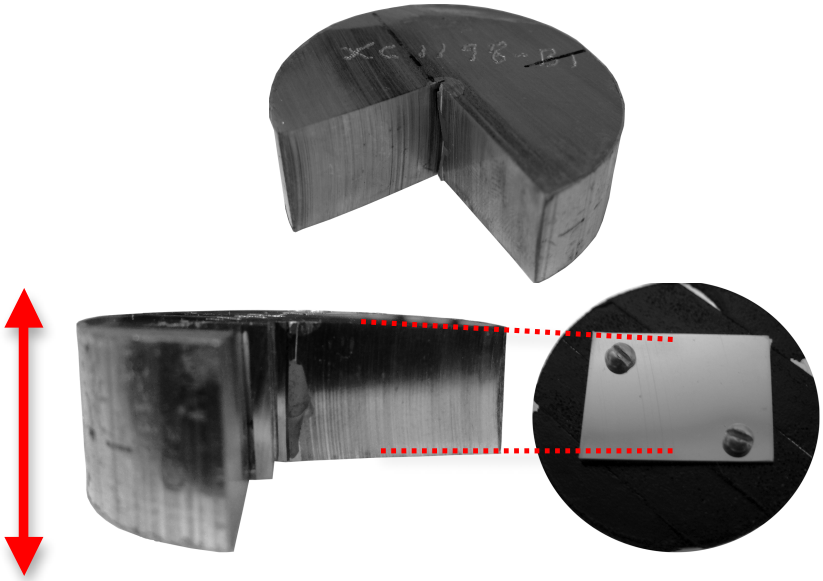

Figure 3.2: Orientation of specimens with respect to the extruded bar. Top image: Inclined view of a section through the bar; Bottom Left image: View of the section perpendicular to extrusion direction; Bottom Right image: Example of an SEM specimen. The red arrow indicates the extrusion direction.

spectrometer (EDXS). For higher resolution analysis a JEOL JEM-2010 TEM was used operating at 200 kV. This microscope is equipped with a UHR objective lens polepiece ($C_s \approx 0.5$ mm), which gives a point-to-point resolution of <0.19 nm at Scherzer defocus, and an EDAX Phoenix EDXS detector that has a super-ultrathin polymer window.

3.2.4 *Focused Ion Beam (FIB) and Serial sectioning*

The FIB serial sectioning experiments were performed on the same samples that were described in section 3.2.1 for SEM imaging. Serial sectioning was performed using a FEI Dual Beam Strata 400S system, which consists of a vertical electron column, a FIB column tilted at 52° to the electron column, and a Gas Injection System (GIS) that is used for depositing Pt onto the sample. A schematic diagram of this dual beam system is shown in Figure 3.3. The SEM was used to acquire electron images using the high-resolution TLD detector in free-field mode during the preparation stage, and the TLD detector was switched to the UHR immersion mode during the serial sectioning. The FIB was used for preparation and serial sectioning of the volume of interest. The ion source on the FIB emits Ga^+ ions and the ion column was operated at an accelerating voltage of 30 kV and various currents depending on the process being performed (e.g. Pt deposition, imaging, milling, serial sectioning). However, very limited imaging was performed using the ion beam because even very short exposure times and low ion beam currents led to sputtering of the material. Therefore, when ion beam imaging was necessary an ion beam current of 9.7 pA was used for general surveying.

Since the ion beam column on the FIB is tilted 52° away from the SEM column, it is necessary to tilt the sample stage in the FIB so that the sample surface is perpendicular

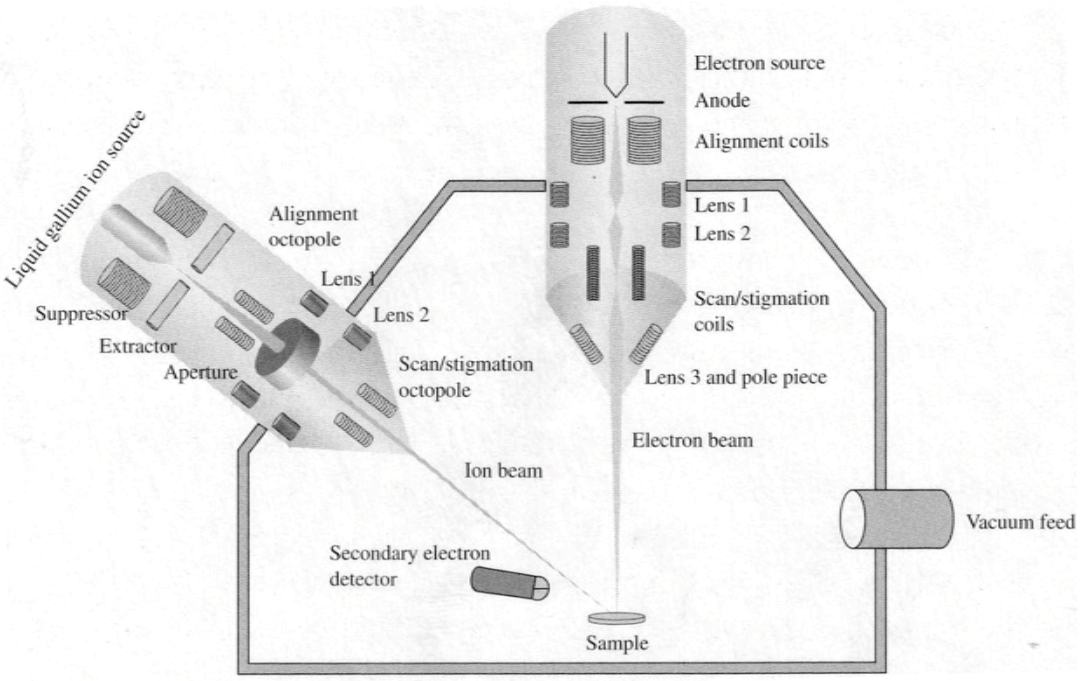

Figure 3.3: Schematic diagram of a Dual Beam FIB/SEM system showing the relative orientations of the electron column, ion column, and the sample. Reproduced from ref [26].

to the ion beam. This arrangement is shown schematically in Figures 3.4 and 3.5. This orientation gives the maximum sputtering rate when using the ion beam. However, a consequence of this orientation is that the SEM images will be foreshortened. The cause of this distortion is that the electron beam is "seeing" a projection of the cross section surface, causing microstructural features in the images to appear compressed in the vertical direction. This distortion is illustrated in Figure 3.6 for a circular shaped feature. Correction for the foreshortening effect will be discussed later.

The first step in the preparation process was to deposit a strip of Pt to protect the volume of interest from unnecessary milling by the ion beam during the preparation and sectioning stages; this also helps to prevent Ga^+ implantation. A Pt layer with dimensions of 2 μm wide × 3 μm long × 1 μm in thickness is deposited using the GIS and the ion beam in the FIB. An illustration of the Pt deposition using the GIS and ion beam is shown in Figure 3.7. A needle is inserted to about 100 μm above the sample surface. A precursor compound paste consisting of $(CH_3)_3$ Pt (C_pCH_3) is heated into a gas and injected through the needle forming a cloud on the sample surface. The ion beam is then scanned across the region of the surface where the deposition is desired. The Ga^+ ions interact with the gas molecules causing them to decompose leaving behind the Pt, which is deposited, on the surface. This Pt deposition process is performed with an ion beam current of 48 pA. An example of a Pt strip is shown in Figure 3.8a.

The next step is to mill out a trench around the Pt layer. The trench geometry chosen was the "U" shape depicted in Figures 3.8b and 3.8c. After milling of this "U" shaped trench, the remaining material, called the pier, will be the volume of interest. This trench geometry is desired because some of the material that is sputtered away

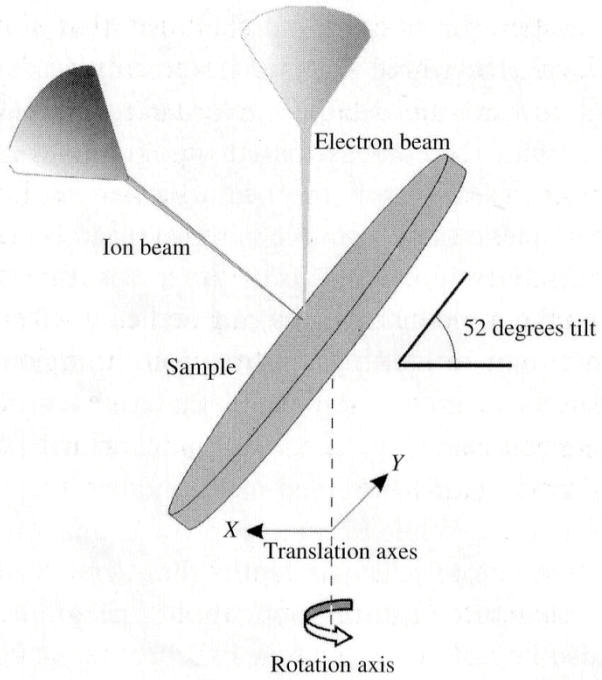

Figure 3.4: Schematic diagram showing the orientation of the sample surface relative to the electron and ion beams during the serial sectioning process. Reproduced from ref [26].

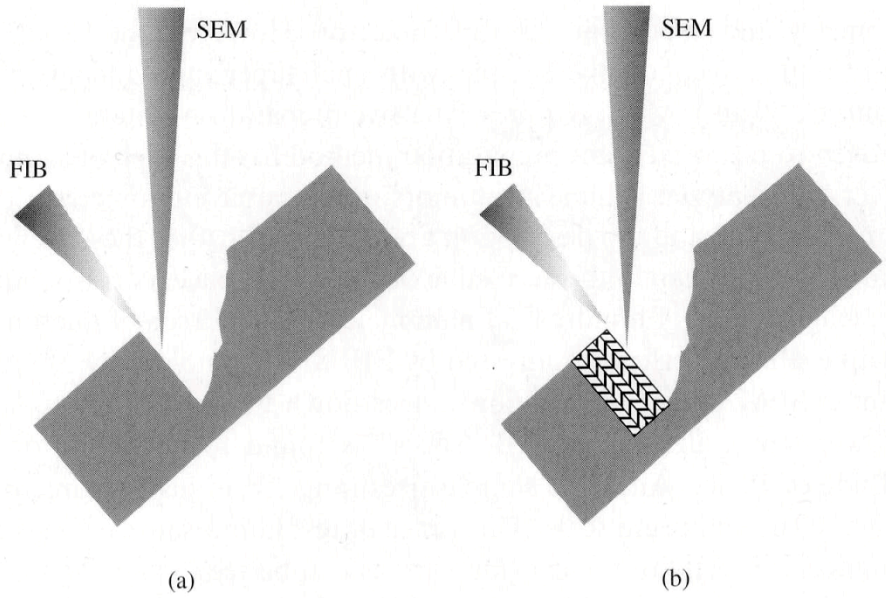

Figure 3.5: Schematic diagrams (a) illustrating the orientation of the pier's front face relative to the electron and ion beams and (b) illustrating the serial sectioning process in which thin slices are milled using the ion beam and images are acquired using the electron beam. Reproduced from ref [26].

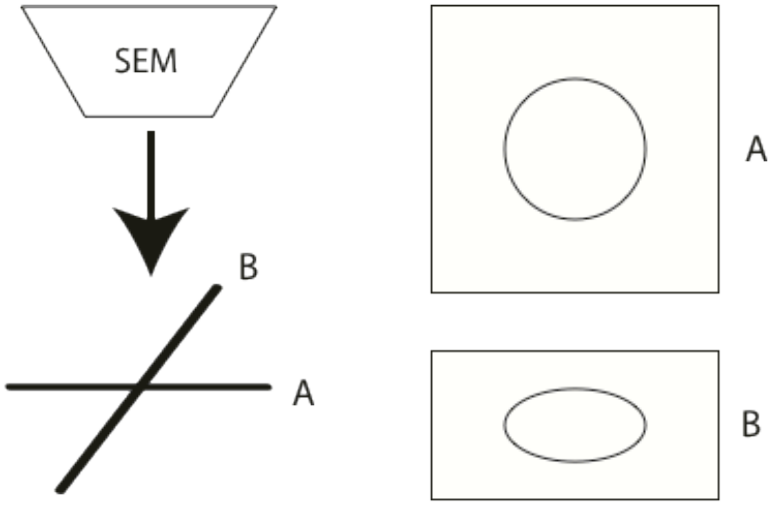

Figure 3.6: Schematic diagram illustrating the vertical compression of a circular feature because of foreshortening. In position A, the sample surface is perpendicular to the electron beam, and the feature is observed as a circle. In position B, the sample surface is inclined to the electron beam, which causes the circle to appear as an ellipse.

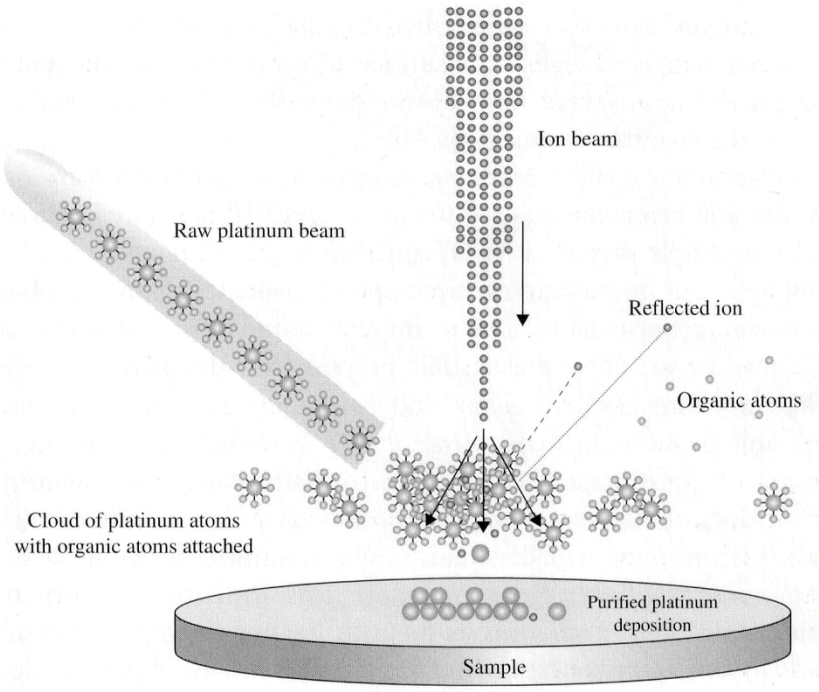

Figure 3.7: Schematic of GIS process. Ion beam interacts with GIS gas molecules causing them to decompose. The volatile component is taken away while the Pt is deposited as a layer on the sample surface. Reproduced from ref [26].

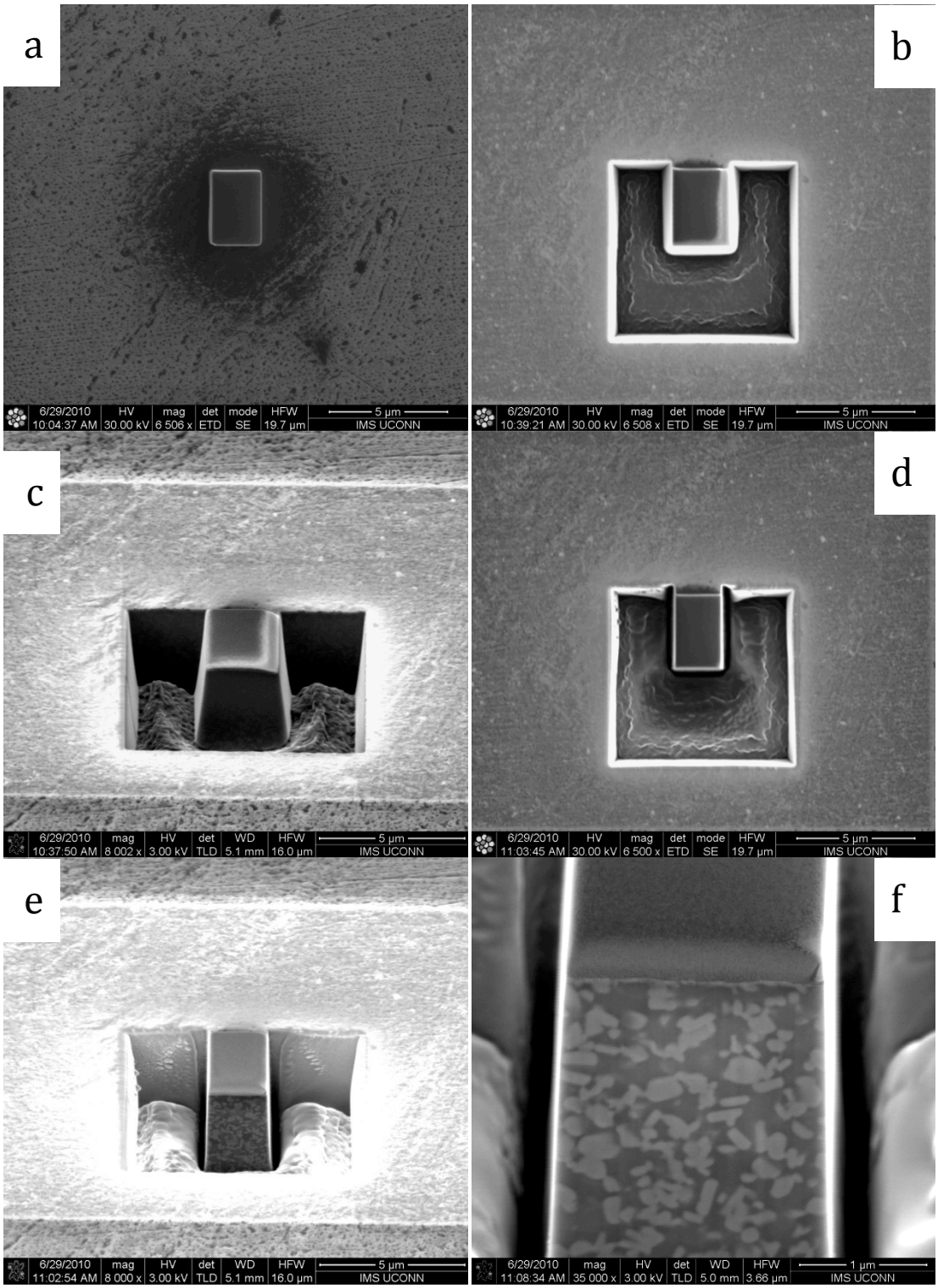

Figure 3.8: Example SEM images of the different preparation steps before serial sectioning. (a) Pt deposited layer (Ion beam image), (b-c) Front and side trenches milled using FIB, images taken with (b) ion beam and (c) electron beam, (d-e) After Cleaning Cross Section procedure to straighten walls of pier and to clean the cross section surface of redeposit, (d) ion beam image and (e) electron beam image, (f) High magnification image of cross section using electron beam showing the material's microstructure.

during the serial sectioning process will redeposit on any near-by surfaces. Therefore, this U-trench geometry allows plenty of space for the accumulation of redeposited material, which keeps the field of view clear of any obstructions that could lead to degradation of image quality. Since the trench contained the largest volume of material to be removed, a higher ion beam current of 210 pA was used in order to mill the trench within a reasonable amount of time.

After milling of the trench is complete, the pier does not have completely vertical sides. This is evident from the taper to the pier faces in Figure 3.8c. These faces are squared off by performing a routine on the FIB called Cleaning Cross Section (CCS). This method essentially "cleans" the surface by slowly milling thin layers of material line by line in a moving front. Once the pier faces are straightened, the last preparation step is to clean the front face of all the redeposited material using the same CCS routine. The results of the CCS routine applied to clean the pier faces are shown in Figures 3.8d and 3.8e. The CCS routines are done using an ion beam current of 48 pA. After performing the CCS routine on the front face, it can be seen in Figures 3.8e and 3.8f that the microstructure of the material is now visible and the volume is ready for the serial sectioning procedure.

For the serial sectioning process, a script provided by FEI called Auto Slice & View (AS&V) is used which controls the FIB automatically. This script allows the user to input parameters such as the ion and electron beam image scan speeds, number of slices, and slice thickness. Once the inputs are inserted the script is activated, which will automatically run the FIB to mill slices of the given thickness and to acquire an image after each fresh front face of the pier is exposed. The serial sectioning procedure is

shown schematically in Figure 3.5b. The results are stacks of two-dimensional images of the sub-surface microstructure of the material. In this study, image stacks consisting of 200 slices were acquired with each slice being approximately 10 nm thick.

3.2.5 *Amira 3D reconstruction*

The software used for the three-dimensional reconstruction of the microstructure was the Resolve RT 5 – FEI edition of Amira. This program was provided with the Dual Beam system.

After importing the images into Amira, the first step was to correct for the foreshortening effect described previously using Figure 3.6. The inclination of the front face of the pier with respect to the electron beam will cause images taken at this orientation to have their vertical axis compressed. Increasing the vertical dimension of the images by approximately 27% compensates for this foreshortening effect.

The next step was alignment of the images. This step corrects for small shifts in the electron beam, drift due to stage movement, and the removal of material during the sectioning process. As each slice is milled, the front face of the pier will physically recede towards the rear of the trench. Therefore, this movement coupled with the inclination of sample with the electron beam will cause the pier images to drift in the vertical direction. This effect can be seen in Figure 3.9, which shows four representative images (image 1, image 30, image 70, and image 100) from a serial sectioning experiment. The alignment process was done using the alignment module in Amira. In this mode, alignment of the images can be done using a variety of manual and automatic tools. However, the best results were obtained doing a manual alignment using the least

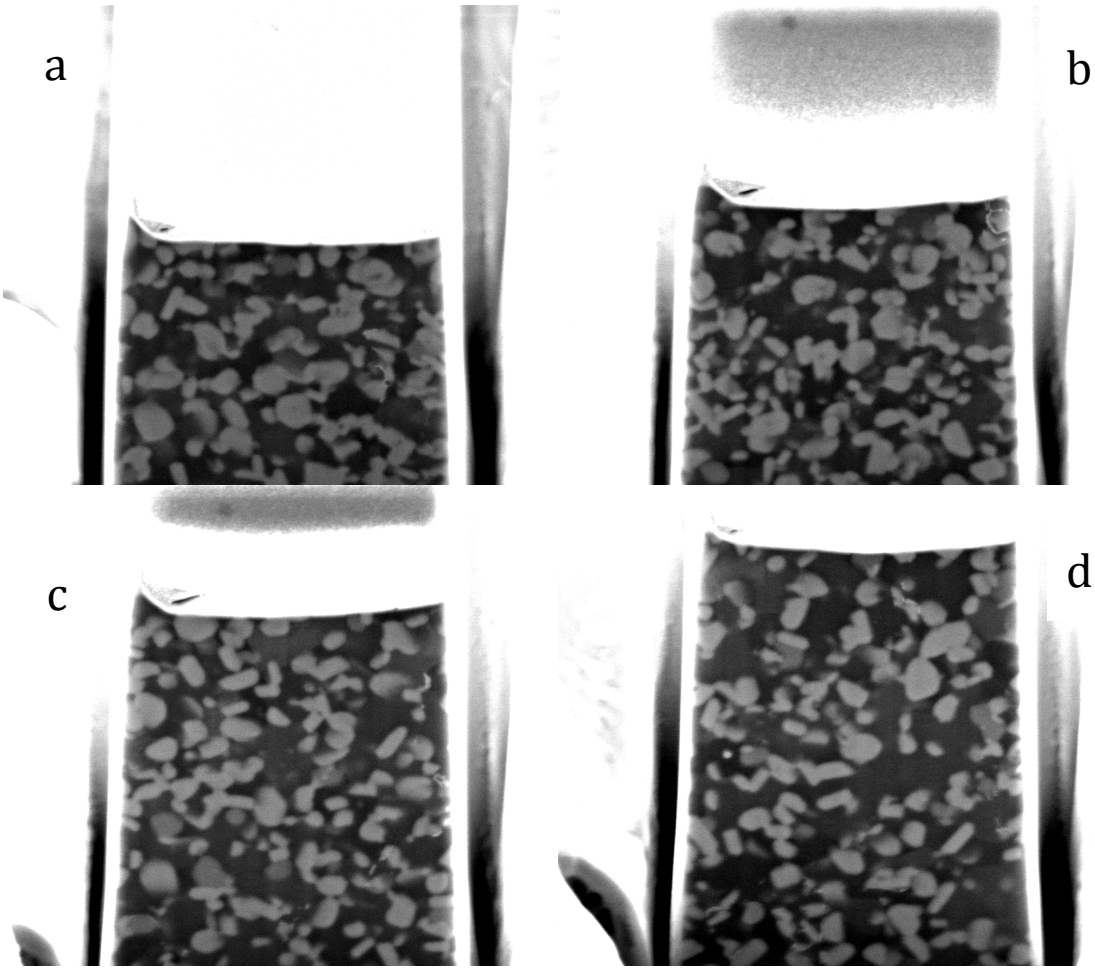

Figure 3.9: Example of receding cross section with progression of serial sectioning which causes each slice to be misaligned. (a) Image 1, (b) Image 30, (c) Image 70, and (d) Image 100.

squares alignment mode. A simple schematic showing this alignment process is shown in Figure 3.10. The least squares alignment mode shows two sequential, slightly transparent images on the user interface. A comparison of the pixels in the images is performed and a percentage of quality is reported. A higher value of quality indicates a better match between the images. At the maximum quality value, the contrast between the two images is minimized because all the microstructure features are lying on top of one another. During this alignment process one image is selected to be the stationary reference. The other image is moved until the two images are well aligned (based on quality value and minimum observed contrast) as shown in Figures 3.10b and 3.10c. Afterwards the second image becomes the reference, the next image in the stack is superimposed on this one, and the process is repeated until all the images are aligned. After the alignment process, the images are cropped to remove any unnecessary regions such as the trench area and top of the sample surface.

The final step before three-dimensional reconstruction was segmentation of the microstructural features. However, typical image processing and thresholding to isolate the precipitates from the matrix could not be utilized, so manual selection of particles was performed. The high volume fraction of precipitates in the alloy causes too many of the precipitates to overlap and become indistinguishable; this overlap masks individual morphologies of the precipitates and the orientation changes after the forging upsets, which are the key elements in this study.

The first step in the manual segmentation process was to identify well-defined, continuous features in the microstructure by scrolling through the image stack. Once a suitable precipitate was found, the pixels in each slice associated with this feature were

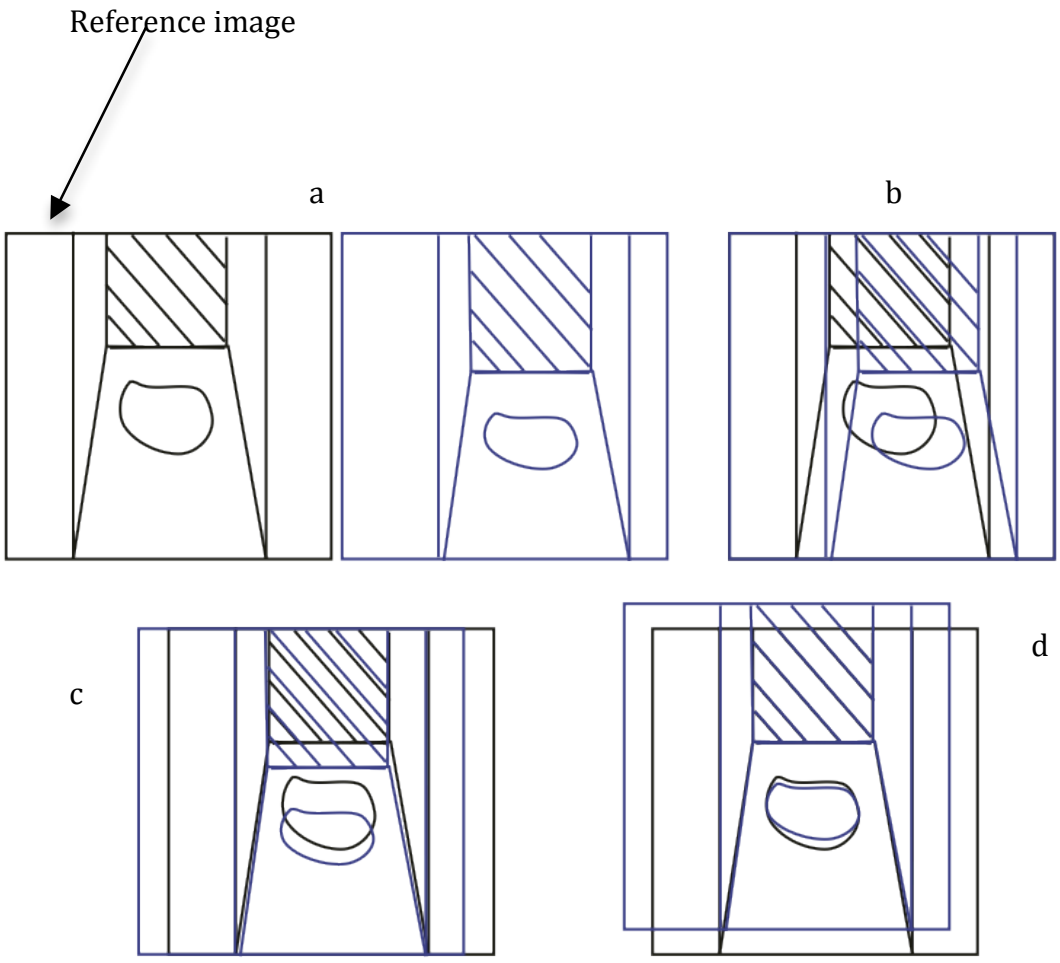

Figure 3.10: Schematic diagram showing the manual alignment of images using the Least Squares Tool in Amira. (a) Two sequential raw images shown side by side. (b) Overlay of the two images in (a) showing a mismatch. (c) Displacement of the second image with respect to the reference image. A better match between the features is obtained. (d) Further shift of the second image relative to the reference is performed to obtain the best possible percentage fit.

then selected and saved. This selection process isolates that particular feature's volume from the rest of the material. These selected areas are then combined with the appropriate slice thickness to convert them into slabs of volume. Lastly, Amira performs the final three-dimensional reconstruction by stacking these slabs together. This process is shown schematically in Figure 3.11, in which the filled circles are the selected pixels corresponding to a feature of interest. The final result is a surface representation of the segmented feature.

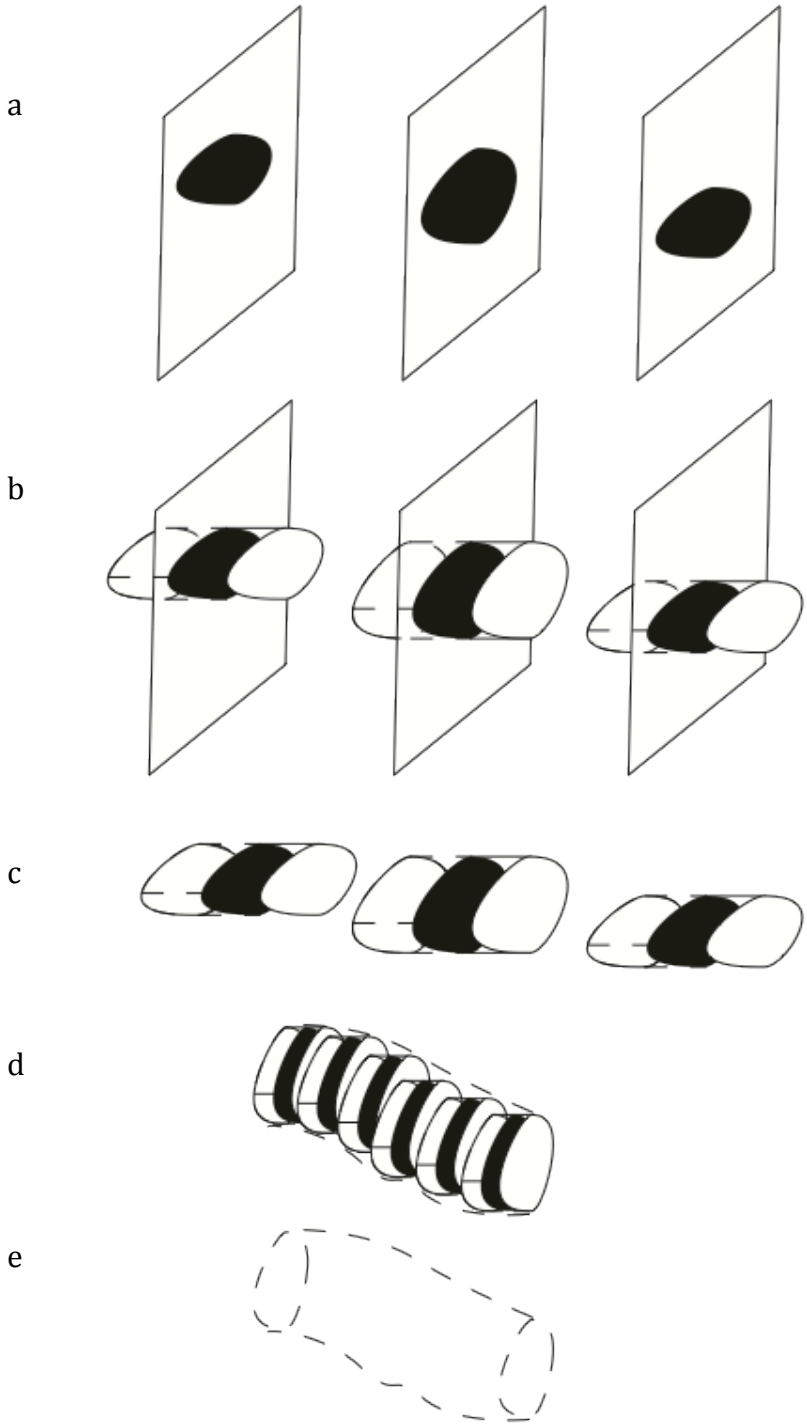

Figure 3.11: Schematic diagram showing how Amira generates a three-dimensional volume from selected pixels on slices. (a) The shaded shapes represent segmented pixels on each slice. (b-c) The segmented pixels on each slice are given the appropriate input slice thickness to create a local slab of the volume. (d-e) The adjacent slabs are stacked together generating the final volume.

Chapter 4: Experimental Results

4.1 **Initial Microstructure**

4.2 **Comparison of As-Extruded and Forged Microstructures**

4.3 **Three-dimensional Tomography**

4.4 **Challenges with FIB Tomography**

Chapter 4: Experimental Results

The main emphasis of this study was the characterization of the microstructural evolution in forged Al-Ni-Y-Co alloys using three-dimensional tomographic techniques. The data in this study was obtained using XRD, SEM, TEM and FIB, and is presented in this chapter in three sections. The starting microstructure of the as-extruded material, as revealed using XRD, SEM and TEM, is described in the first section. A comparison of data obtained from the as-extruded and forged materials using XRD, SEM and TEM is presented in the second section. The final section contains the results from the tomographic experiments performed on the FIB. These FIB results were used to build three-dimensional reconstructions of the microstructures. In addition, examples of results showing the challenges encountered during serial sectioning are presented.

4.1 Initial Microstructure

The starting microstructure in the Al-Ni-Y-Co alloy studied in this thesis is very similar to those observed in other fully devitrified Al-RE-TM systems as described in section 2.2.4. A typical X-ray diffraction spectrum taken from a section parallel to the extrusion direction of the as-received material is shown in Figure 4.1. The spectrum contains very strong peaks that correspond to those expected for a fcc metal with lattice parameter of 0.405 nm, which is characteristic of Al. All of the remaining weaker peaks in the spectrum correspond to those expected from the strongly diffracting planes in the $Al_{19}Ni_5Y_3$ phase described by Vasiliev et al [30-33]. However, the relative intensities of these weaker peaks are not equal to those expected, which may suggest that the particles are not oriented randomly within the extrudate.

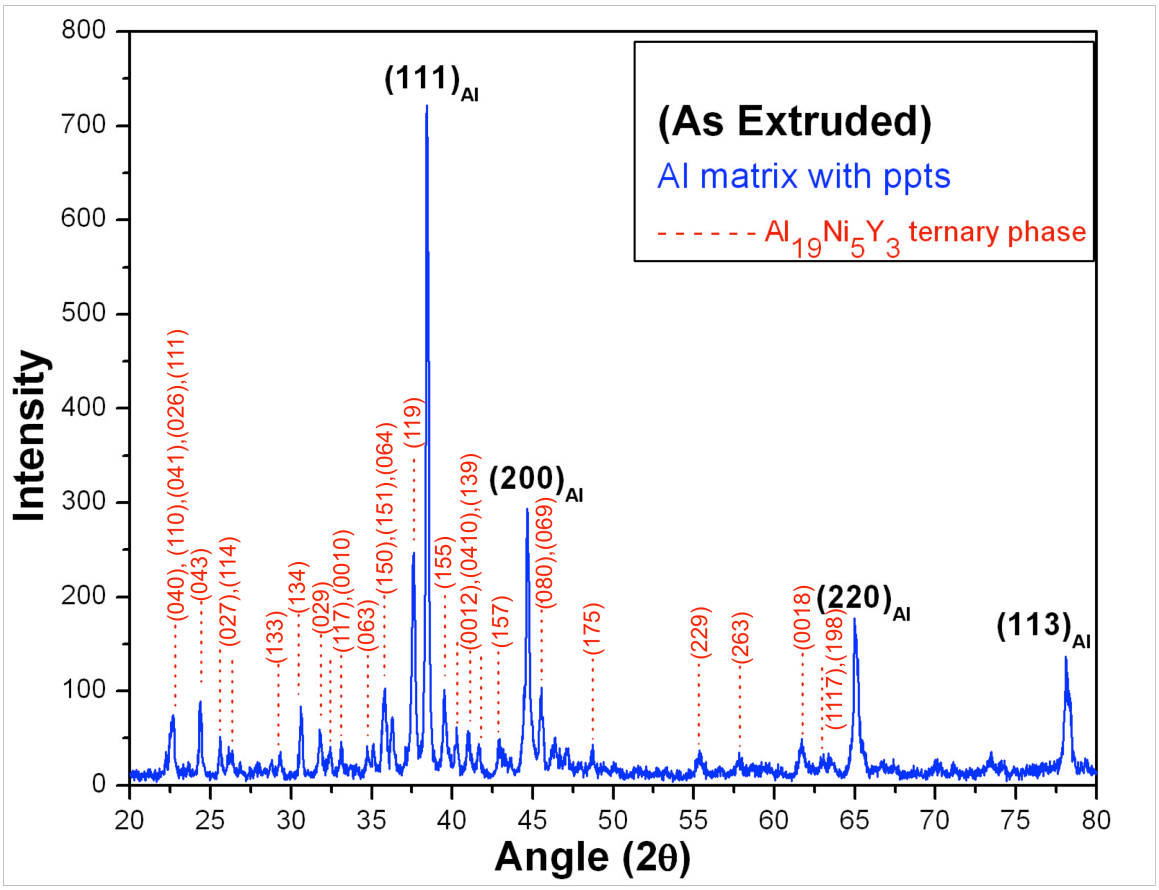

Figure 4.1: X-ray diffraction spectrum taken from the as-extruded Al-Ni-Y-Co alloy. The spectrum contains very strong Al peaks, while the weaker peaks all correspond to those expected from the $Al_{19}Ni_5Y_3$ phase.

Electron microscopy techniques were used to further characterize the size, distribution, and morphology of the phases present in the microstructure. SEM backscattered electron images taken from a section parallel to the extrusion direction of the as-received material is shown in Figure 4.2. The electron beam is perpendicular to the section surface, and the images are aligned with the extrusion direction parallel to the vertical axes. Since there is a large difference in density between fcc Al (2700 kg m^{-3}) and the $Al_{19}Ni_5Y_3$ phase (4116 kg m^{-3}) in addition to the atomic number differences, it is expected that the ternary phase will yield more backscattered electrons and appear brighter. This is consistent with the contrast in the SEM BSE images, which reveal bright $Al_{19}Ni_5Y_3$ particles surrounded by the darker gray Al matrix. Examination of the high magnification image in Figure 4.2 shows that there is an apparent variation in the morphology of the $Al_{19}Ni_5Y_3$ phase from rod-shaped to ellipsoidal particles. Extensive TEM experiments performed by Vasiliev et al on other fully devitrified Al-RE-TM alloys revealed that the $Al_{19}Ni_5Y_3$ phase exhibits a plate morphology [30-33]. It is possible that the apparent morphological variation in the $Al_{19}Ni_5Y_3$ phase from BSE SEM images is actually due to sectioning effects through such plates. Therefore, if the plates are viewed edge-on they will appear as rods, and if the section viewed is at some other rotation along the vertical axis (extrusion direction) of the image the plates will appear ellipsoidal as seen in Figure 4.2. Also, many of the particles seem to be aligned vertically in the images (i.e. parallel to the extrusion direction). The rod shaped particles have lengths ranging from 120 nm to 420 nm with thicknesses ranging from 50 nm to 120 nm. The ellipsoidal particles have lengths ranging from 250 to 440 nm.

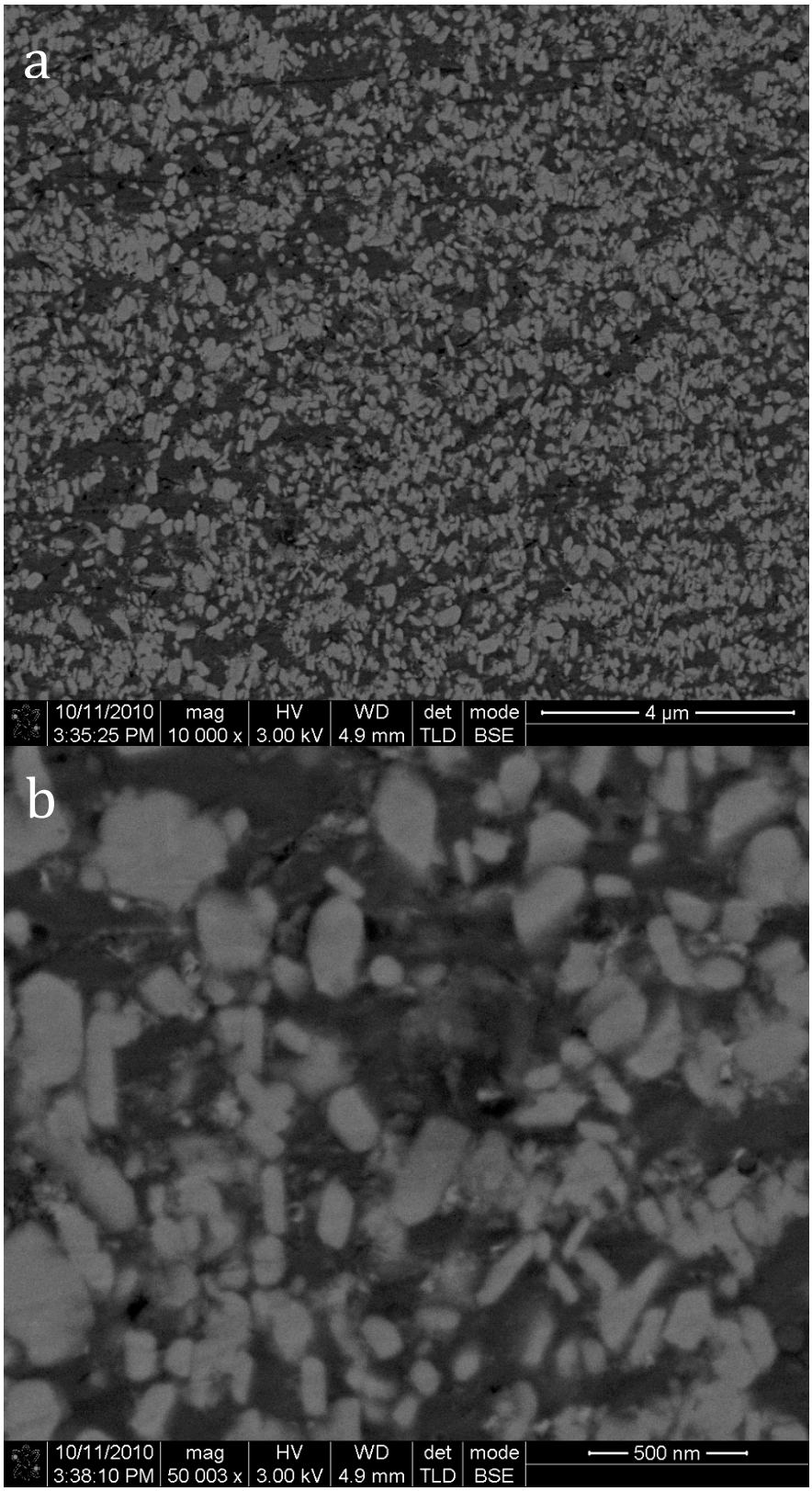

Figure 4.2: Low (a) and high (b) magnification backscattered electron SEM images obtained from sections cut parallel to the extrusion direction of the initial (as-extruded) microstructure for the Al-Ni-Y-Co alloy. The vertical axes of the images are aligned with the extrusion direction.

TEM experiments were also performed to characterize the starting microstructure. A typical bright field TEM image obtained with the electron beam parallel to the extrusion direction is shown in Figure 4.3. The microstructure consists of dark features, which are the $Al_{19}Ni_5Y_3$ plates surrounded by an Al matrix. A typical EDXS spectrum obtained from the $Al_{19}Ni_5Y_3$ phase and the Al matrix are shown in Figures 4.4 and 4.5, respectively. Quantification of the EDXS spectrum of the $Al_{19}Ni_5Y_3$ phase (Figure 4.4) results in a composition of 69.7% Al, 18.3% Ni, 10.4% Y and 1.6% Co (in atomic percent), which matches very closely to that expected from stoichiometry: 70.4% Al, 18.5% Ni 11.1% Y (atomic percent). The particles also exhibit an apparent variation in morphology due to projection effects. However, the majority of the particles appear as rods (i.e. they are viewed edge-on), which suggests that the plates are aligned along the extrusion direction of the material. The particle sizes are also consistent with the SEM results where the rod-shaped particles have lengths ranging from 100 to 400 nm and thicknesses ranging from 60 to 120 nm. The equiaxed and ellipsoidal particles have diameters ranging from 100 to 350 nm.

In other devitrified Al-RE-TM systems, such as those described in section 2.2.4, the microstructures consisted of three phases: an fcc Al matrix, the $Al_{19}Ni_5Y_3$ plates, and an Al_3X binary phase, such as Al_3Ni, Al_3Y, and Al_3Gd, which formed depending on the composition of the overall alloy [30-33]. However, SEM and TEM experiments on the Al-Ni-Y-Co alloy in this study did not reveal any binary phases. Therefore, the alloy in this study can be considered as a two phase system: $Al_{19}Ni_5Y_3$ plates within a fcc Al matrix.

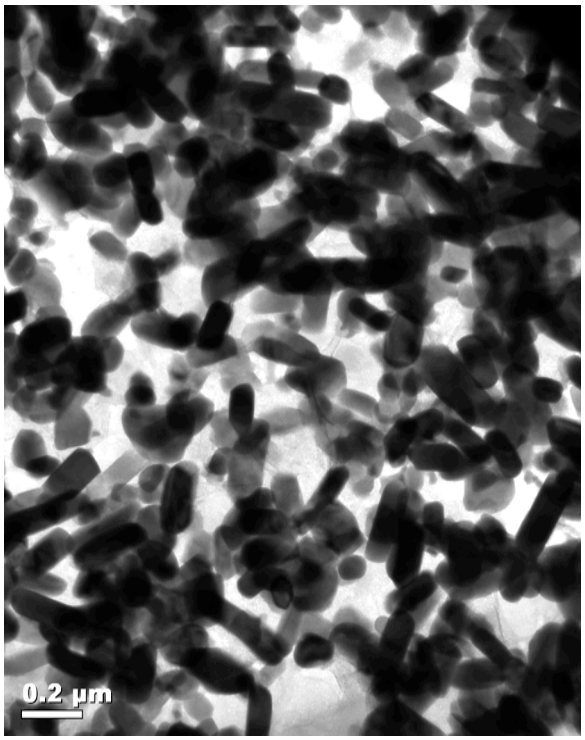

Figure 4.3: Bright field TEM image of the microstructure in the as-extruded Al-Ni-Y-Co alloy consisting of $Al_{19}Ni_5Y_3$ plates in an Al matrix. Electron beam is parallel to the extrusion direction.

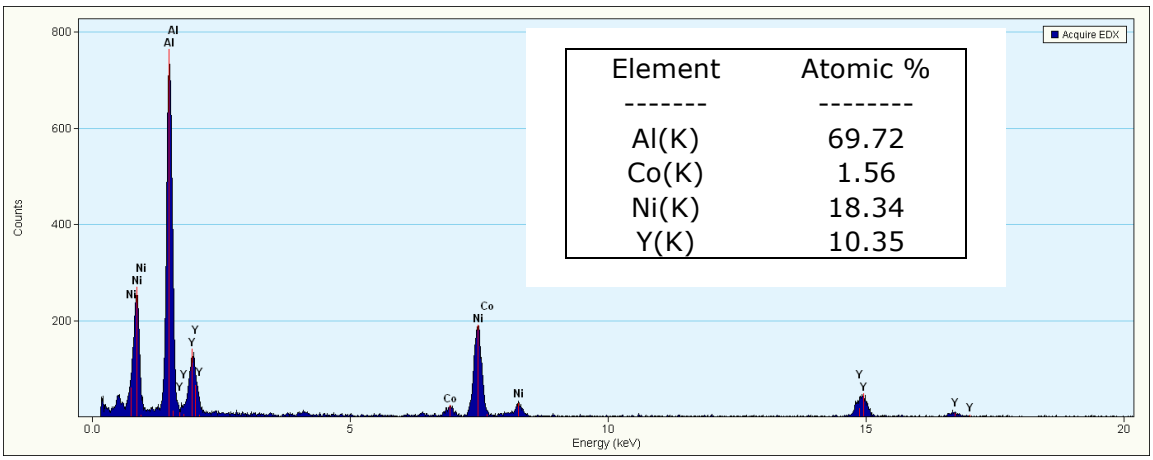

Figure 4.4: Typical EDXS spectrum obtained from the $Al_{19}Ni_5Y_3$ phase.

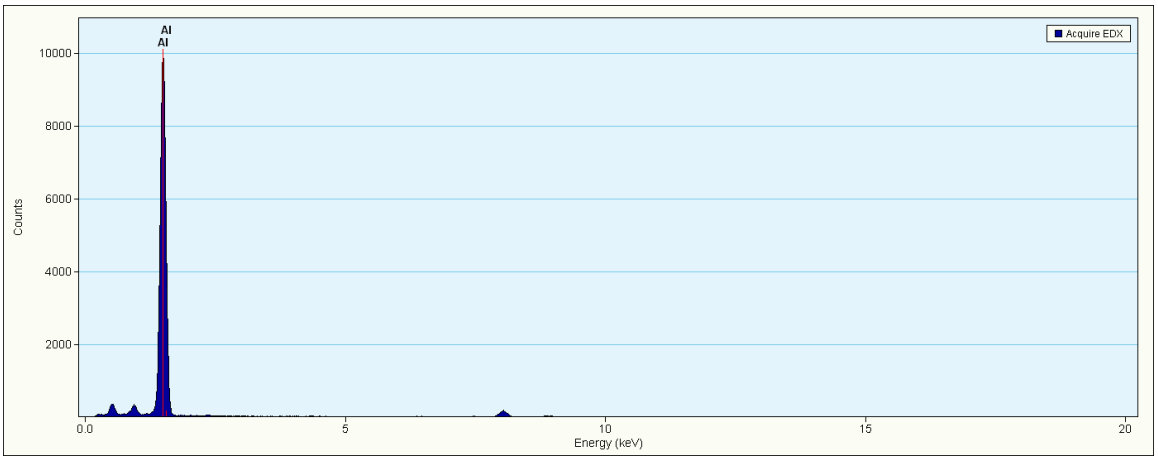

Figure 4.5: Typical EDXS spectrum obtained from the Al matrix.

4.2 Comparison of As-Extruded and Forged Microstructures

As described in section 3.1, the as-extruded material was sectioned perpendicular to the extrusion direction, and the smaller pieces were forged parallel to the extrusion direction at different upsets: 43%, 64% and 84%. Typical XRD spectra taken from sections cut perpendicular to the extrusion direction are shown in Figure 4.6 for the as-extruded and forged materials. The very strong peaks in the spectra correspond to those for fcc Al. The remaining weaker peaks correspond to those expected from the strongly diffracting planes in the $Al_{19}Ni_5Y_3$ phase. However, similar to the as-extruded material, the relative peak intensities of these weaker peaks in the forged alloys are not equal to those expected from particles oriented randomly. In addition, the relative intensities of the $Al_{19}Ni_5Y_3$ peaks change after each forging upset, which suggest that some crystallographic texturing of the $Al_{19}Ni_5Y_3$ plates is occurring.

Electron microscopy techniques were also used to characterize the as-extruded and forged microstructures. SEM backscattered electron images taken from sections parallel to the extrusion direction of the as-extruded, 43%, 64% and 84% upset forged materials are shown at low magnification in Figures 4.7 – 4.10, respectively and at high magnification in Figures 4.11 – 4.14, respectively. The electron beam is perpendicular to the section surface, and the images are aligned with the extrusion direction parallel to the vertical axes. As described in section 4.1, the large difference in density and atomic number will result in strong contrast between the Al matrix and $Al_{19}Ni_5Y_3$ phase. This is consistent with the contrast seen in the BSE SEM images in Figures 4.7 – 4.14, where the microstructure consists of the bright $Al_{19}Ni_5Y_3$ phase surrounded by the darker gray Al matrix. Since there is a strong contrast between the Al matrix and the $Al_{19}Ni_5Y_3$ phase,

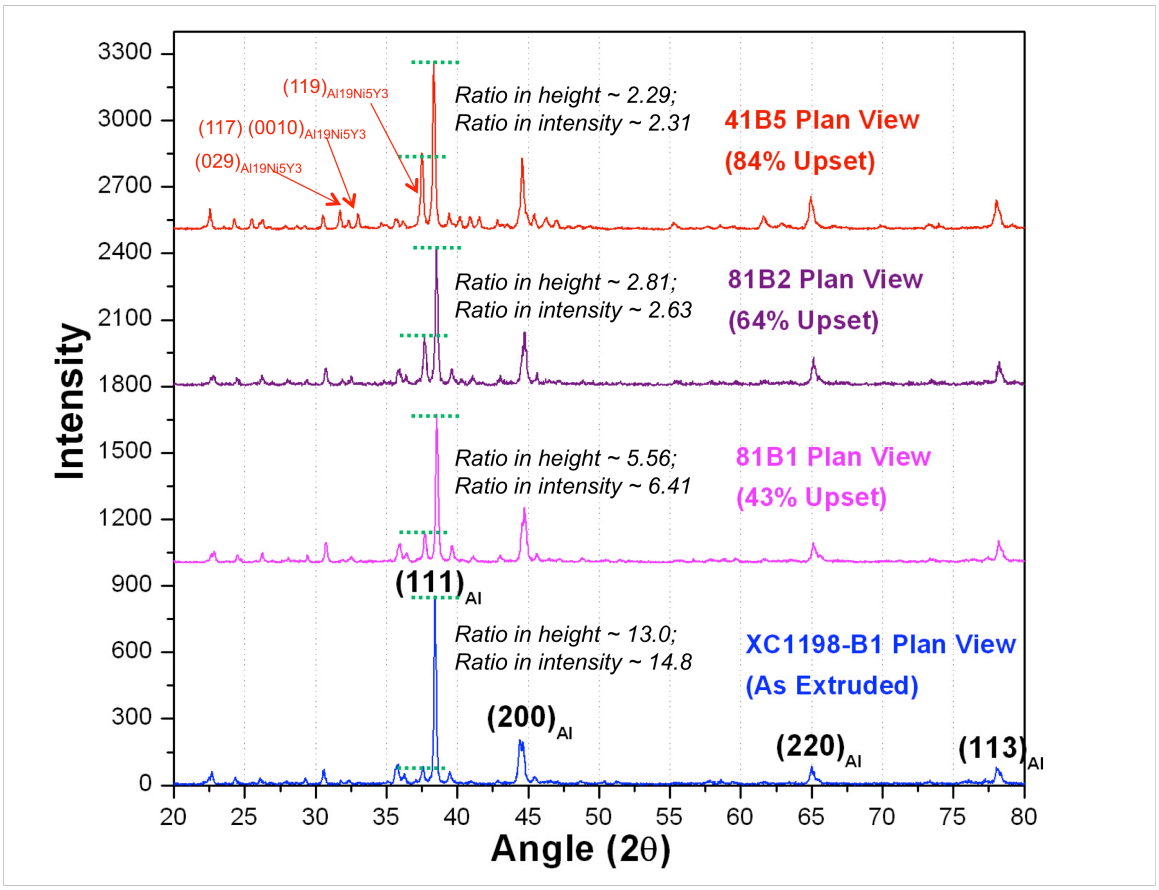

Figure 4.6: X-ray diffraction spectrum acquired from sections cut perpendicular to the extrusion direction of the as-extruded and forged Al-Ni-Y-Co materials.

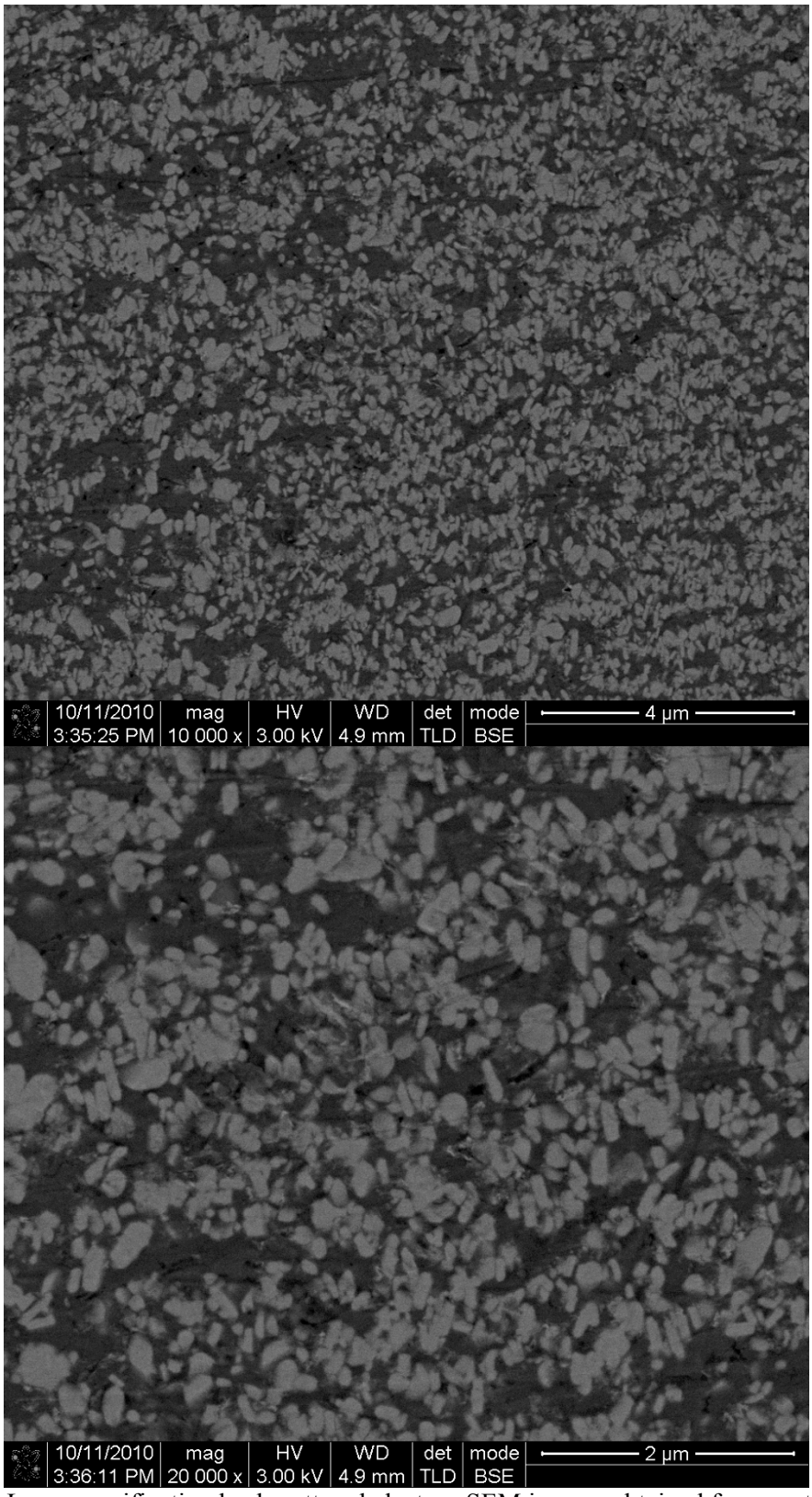

Figure 4.7: Low magnification backscattered electron SEM images obtained from sections cut parallel to the extrusion direction of the initial (as-extruded) microstructure for the Al-Ni-Y-Co alloy. The vertical axes of the images are aligned with the extrusion direction.

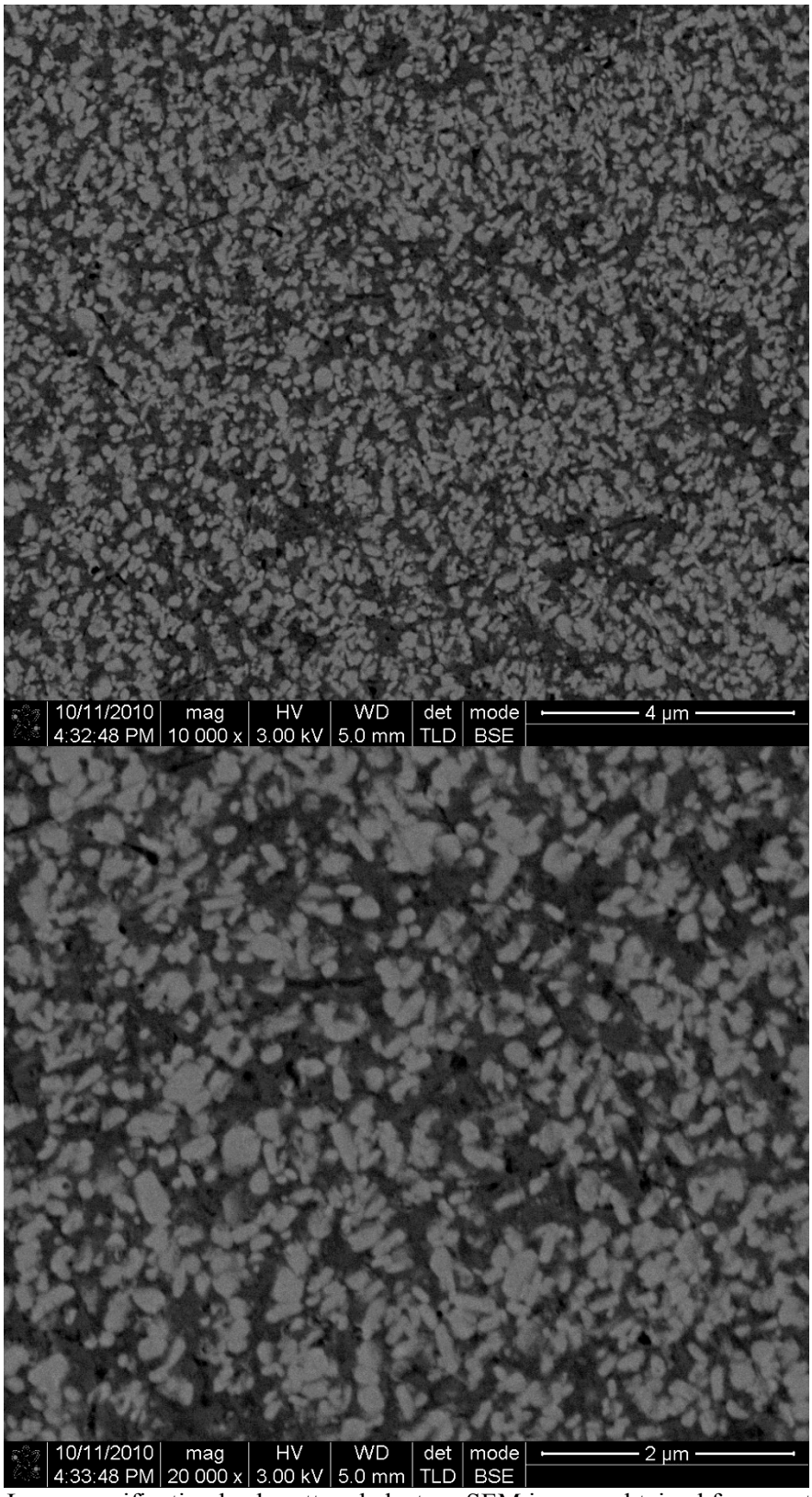

Figure 4.8: Low magnification backscattered electron SEM images obtained from sections cut parallel to the extrusion direction of the 43% upset forged microstructure for the Al-Ni-Y-Co alloy. The vertical axes of the images are aligned with the extrusion direction.

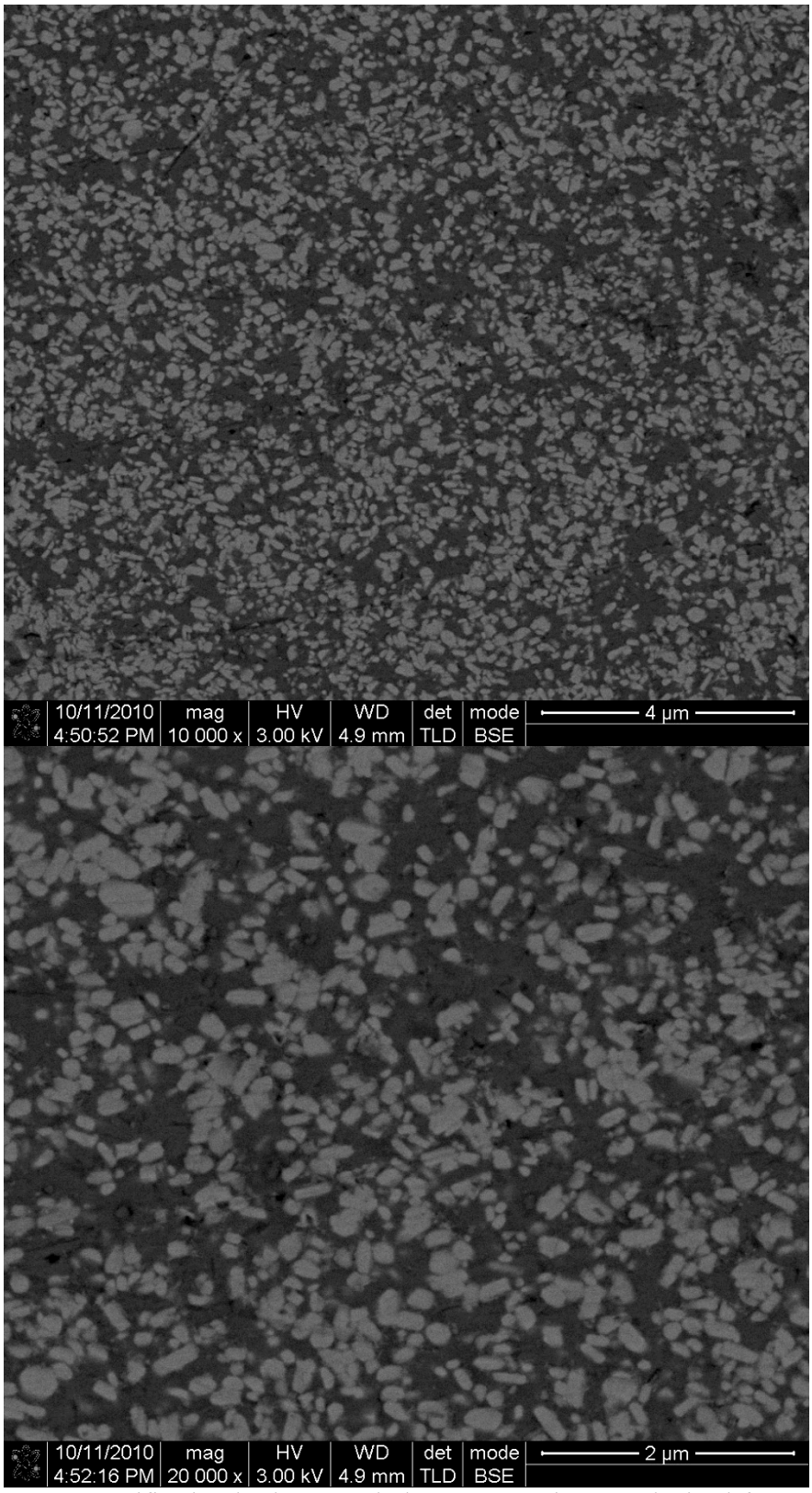

Figure 4.9: Low magnification backscattered electron SEM images obtained from sections cut parallel to the extrusion direction of the 64% upset forged microstructure for the Al-Ni-Y-Co alloy. The vertical axes of the images are aligned with the extrusion direction.

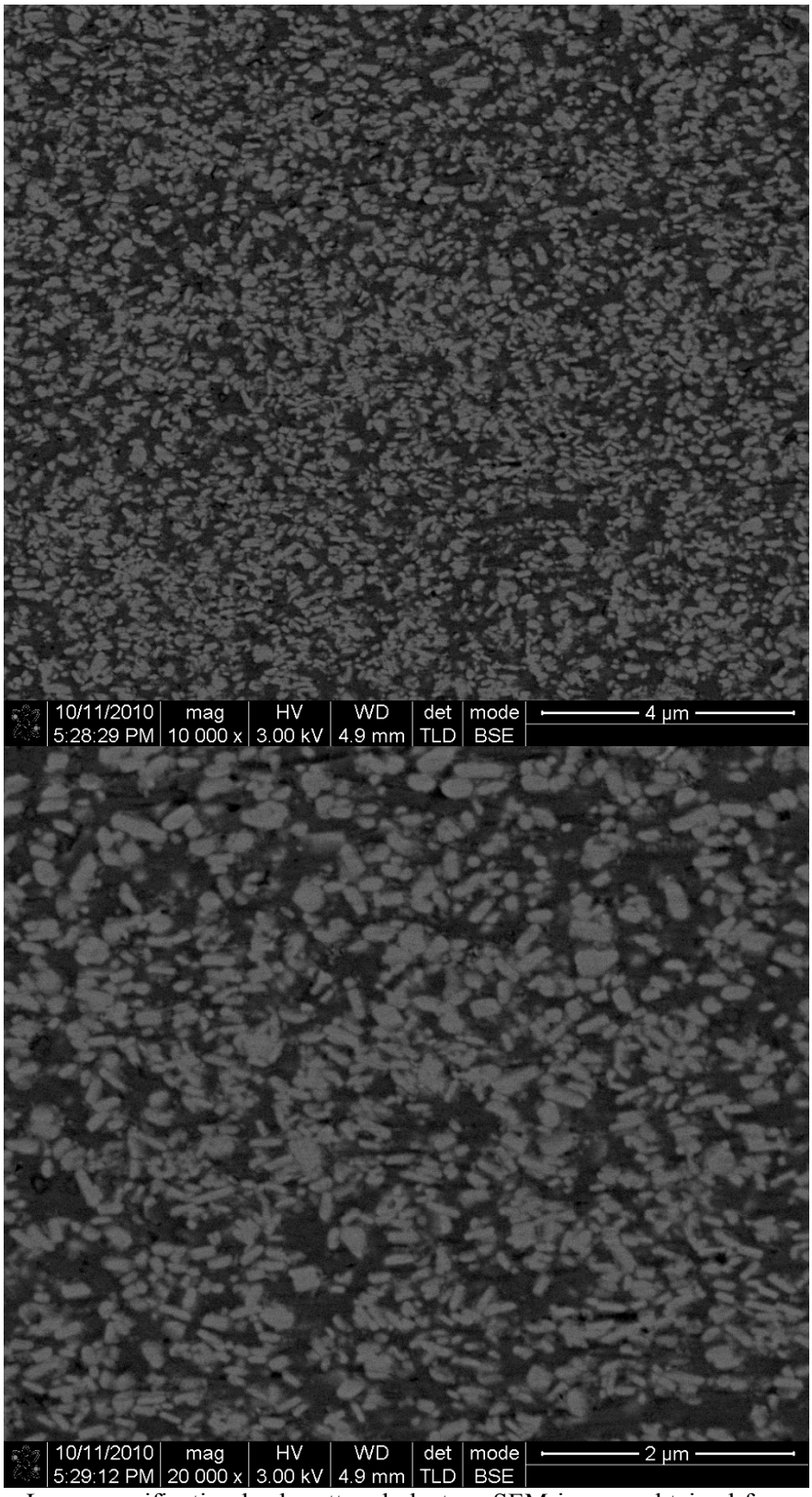

Figure 4.10: Low magnification backscattered electron SEM images obtained from sections cut parallel to the extrusion direction of the 84% upset forged microstructure for the Al-Ni-Y-Co alloy. The vertical axes of the images are aligned with the extrusion direction.

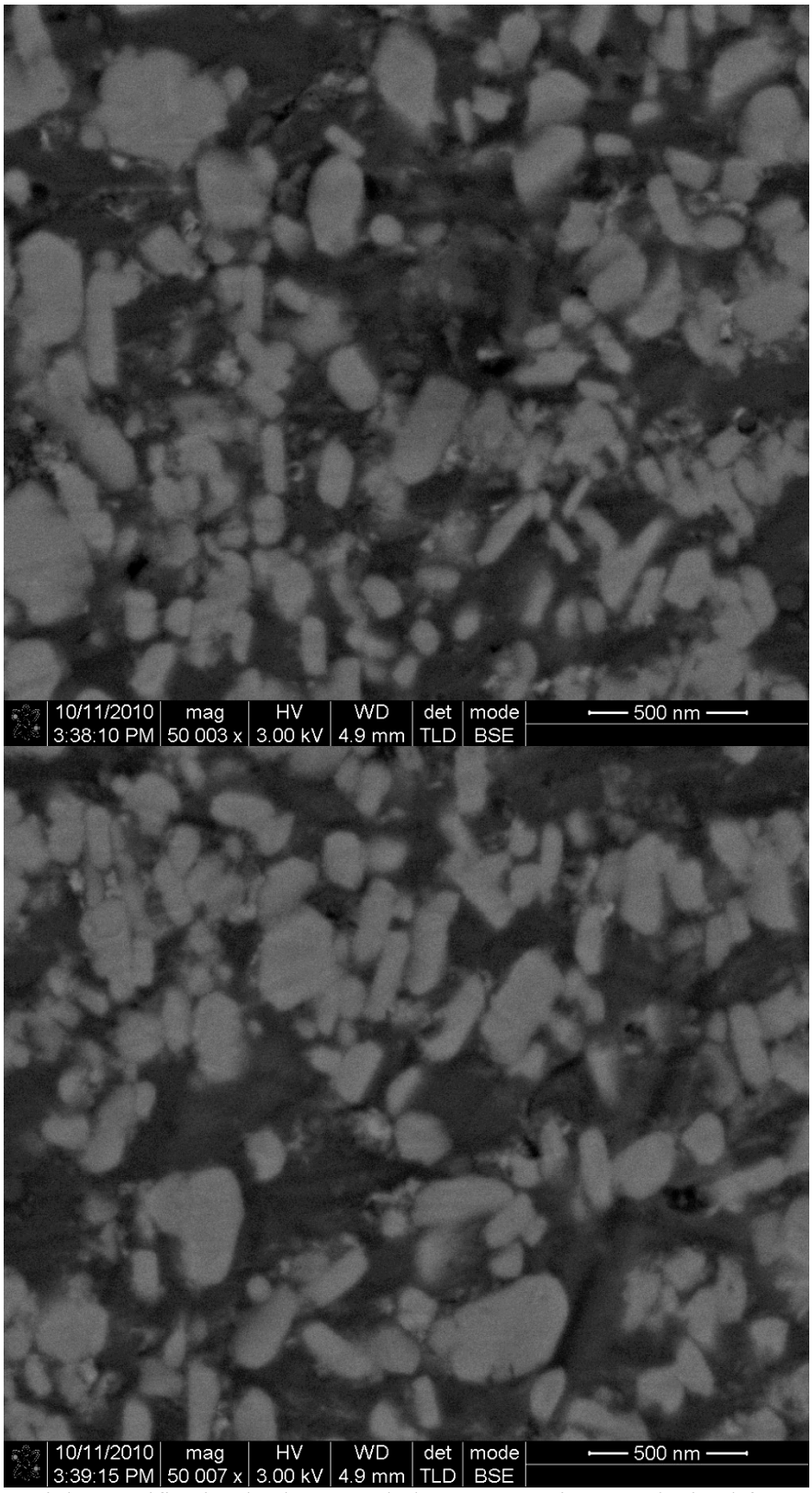

Figure 4.11: High magnification backscattered electron SEM images obtained from sections cut parallel to the extrusion direction of the initial (as-extruded) microstructure for the Al-Ni-Y-Co alloy. The vertical axes of the images are aligned with the extrusion direction.

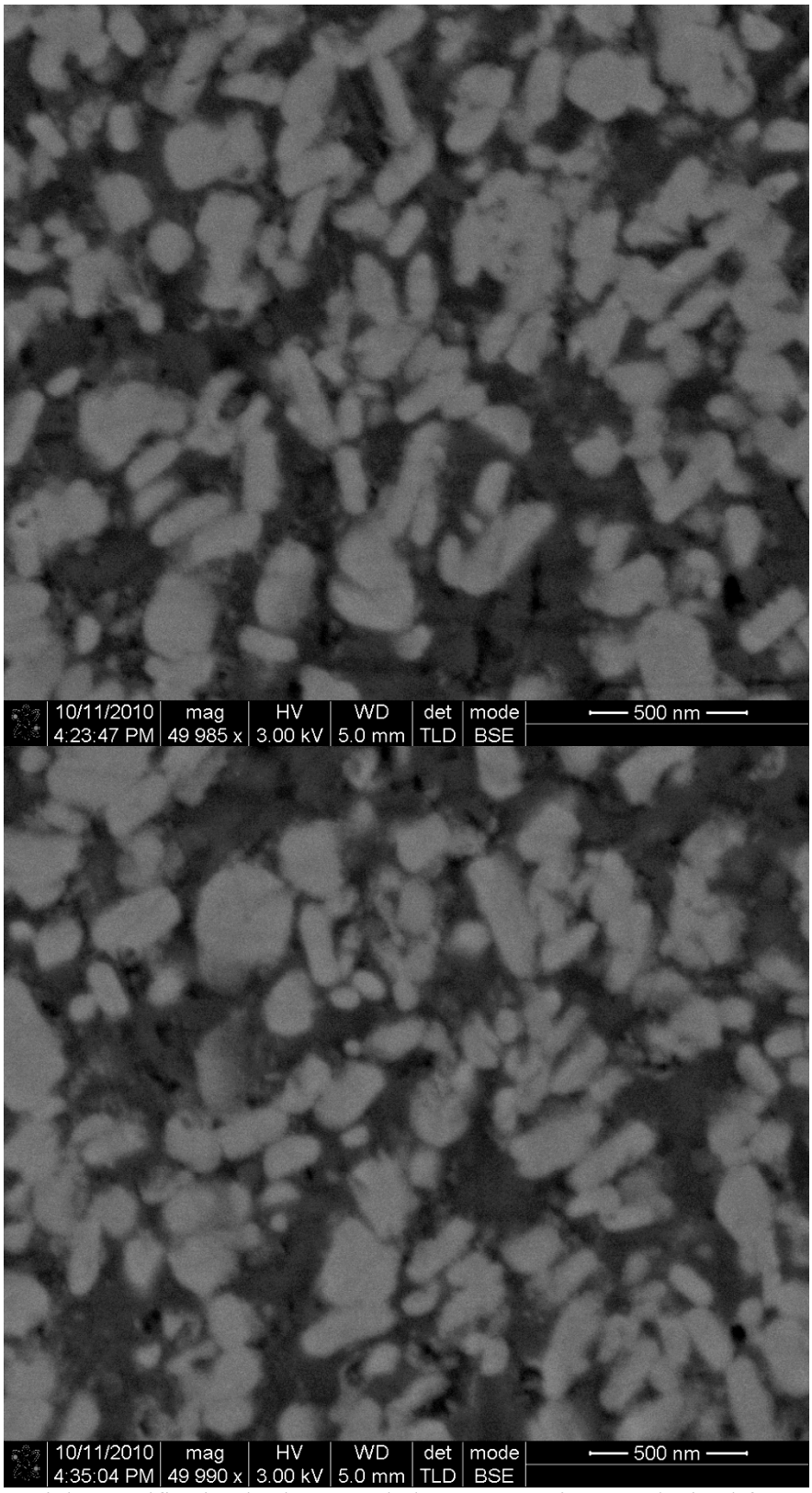

Figure 4.12: High magnification backscattered electron SEM images obtained from sections cut parallel to the extrusion direction of the 43% upset forged microstructure for the Al-Ni-Y-Co alloy. The vertical axes of the images are aligned with the extrusion direction.

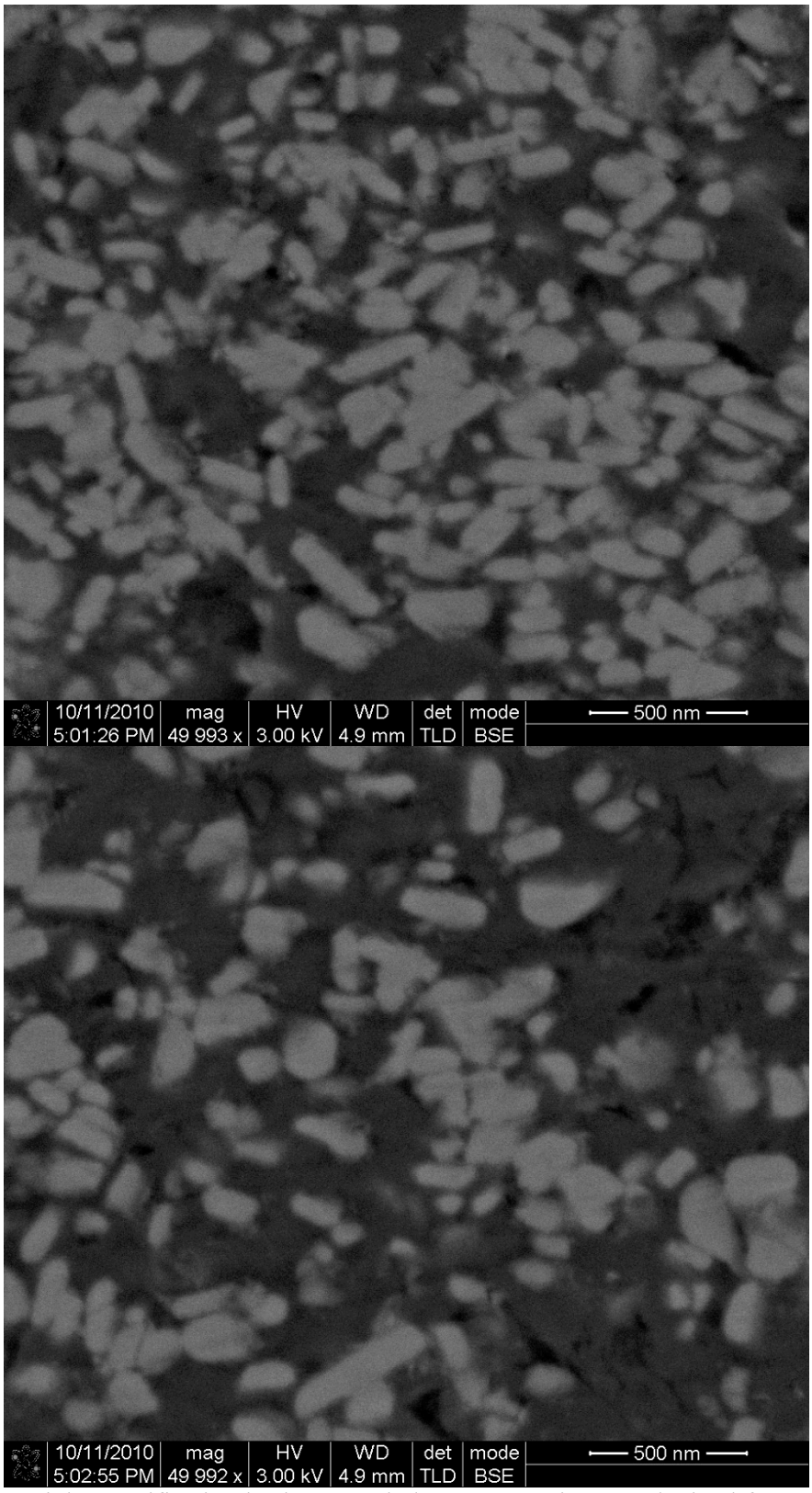

Figure 4.13: High magnification backscattered electron SEM images obtained from sections cut parallel to the extrusion direction of the 64% upset forged microstructure for the Al-Ni-Y-Co alloy. The vertical axes of the images are aligned with the extrusion direction.

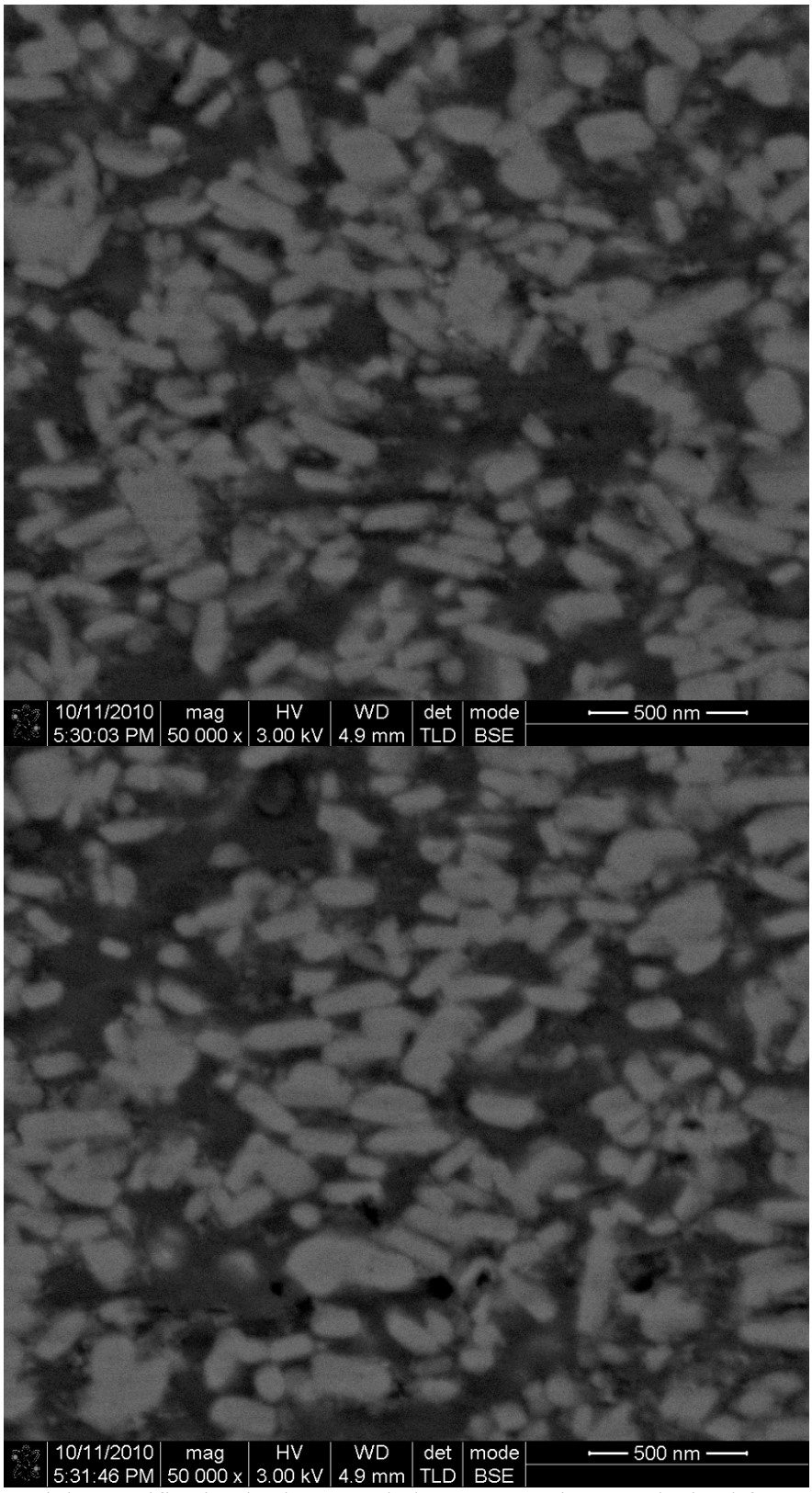

Figure 4.14: High magnification backscattered electron SEM images obtained from sections cut parallel to the extrusion direction of the 84% upset forged microstructure for the Al-Ni-Y-Co alloy. The vertical axes of the images are aligned with the extrusion direction.

simple thresholding was performed using the free software, ImageJ, to calculate the volume fraction. The measured volume faction of the $Al_{19}Ni_5Y_3$ phase was 44%.

The high magnification images in Figures 4.11 – 4.14 reveal some very interesting changes in the microstructure after each processing step. The starting (as-extruded) microstructure is shown in Figure 4.11, which consists of the $Al_{19}Ni_5Y_3$ plates surrounded by the Al matrix. These images reveal that the $Al_{19}Ni_5Y_3$ phase has a tendency to orientate itself along the vertical axis of the images. As discussed in the previous section, the apparent variation in morphology of the $Al_{19}Ni_5Y_3$ phase is due to sectioning effects. The microstructure of the 43% upset forged material, shown in Figure 4.12, reveals no significant change in the $Al_{19}Ni_5Y_3$ particles. The particles still exhibit the apparent variation in morphology of rod-shaped to ellipsoidal. In addition, the orientation of the rod-shaped particles is similar to that observed in the as-extruded material shown in Figure 4.11. Many of the particles in the 43% upset forged material have a tendency towards alignment along the vertical axis with some exhibiting a slight rotation along the image's normal. Rod particles in the 43% upset alloy had lengths and thicknesses ranging from 150 to 400 nm and 75 to 135 nm respectively, while ellipsoidal particles had lengths ranging from 250 to 430 nm. However, changes in the microstructure are observed in the 64% upset forged material, which are shown in Figure 4.13. The general characteristics of the microstructure are similar to those observed in the as-extruded material: rod-shaped to ellipsoidal particles surrounded by an Al matrix. The difference, however, is that many of the $Al_{19}Ni_5Y_3$ particles do not share the same tendency towards alignment with vertical axis as seen in the as-extruded and 43% upset forged materials. Many of the rod-shaped particles exhibit a rotation towards the

horizontal plane of the images suggesting that the $Al_{19}Ni_5Y_3$ plates may have rotated during forging. The rod-shaped particles in the 64% upset alloy had lengths and thicknesses ranging from 190 to 380 nm and 70 to 120 nm respectively (a rod with a length of 475 nm was observed), and ellipsoidal particles had lengths ranging from 200 to 400 nm. Further changes of the $Al_{19}Ni_5Y_3$ phase is observed in the microstructure of the 84% upset forged material shown in Figure 4.14. The majority of the $Al_{19}Ni_5Y_3$ particles are aligned along the horizontal axes of the images. The rod-shaped particles in the 84% upset forged material exhibited lengths and thickness of 200 to 390 nm and 70 to 120 nm, respectively (a rod with a length of 475 nm was observed), and ellipsoidal particles had lengths ranging from 150 to 500 nm. Thus, there is no significant change in particle size even after the large forging upset.

Typical bright field TEM images taken from these materials are shown in Figure 4.15 where the electron beam is parallel to the extrusion direction. Recall that for the as-extruded material, shown in Figure 4.15a, there is an apparent variation in the morphology of the $Al_{19}Ni_5Y_3$ phase from rod-shaped to ellipsoidal which is caused by projection effects in the TEM. However, the majority of the $Al_{19}Ni_5Y_3$ phase exhibits a rod-shaped morphology, which means they are being viewed edge-on and suggests that the plates are aligned with the extrusion direction. After a forging upset of 43%, there is no significant change in the microstructure shown in Figure 4.15b. The particles still exhibit a distribution of morphologies. The rod-shaped particles have lengths ranging from 150 to 350 nm and thicknesses ranging from 50 to 110 nm, while the ellipsoidal particles have lengths ranging from 130 to 280 nm. However, a forging upset of 64% results in a significant change in the $Al_{19}Ni_5Y_3$ phase as shown in Figure 4.15c. Many of

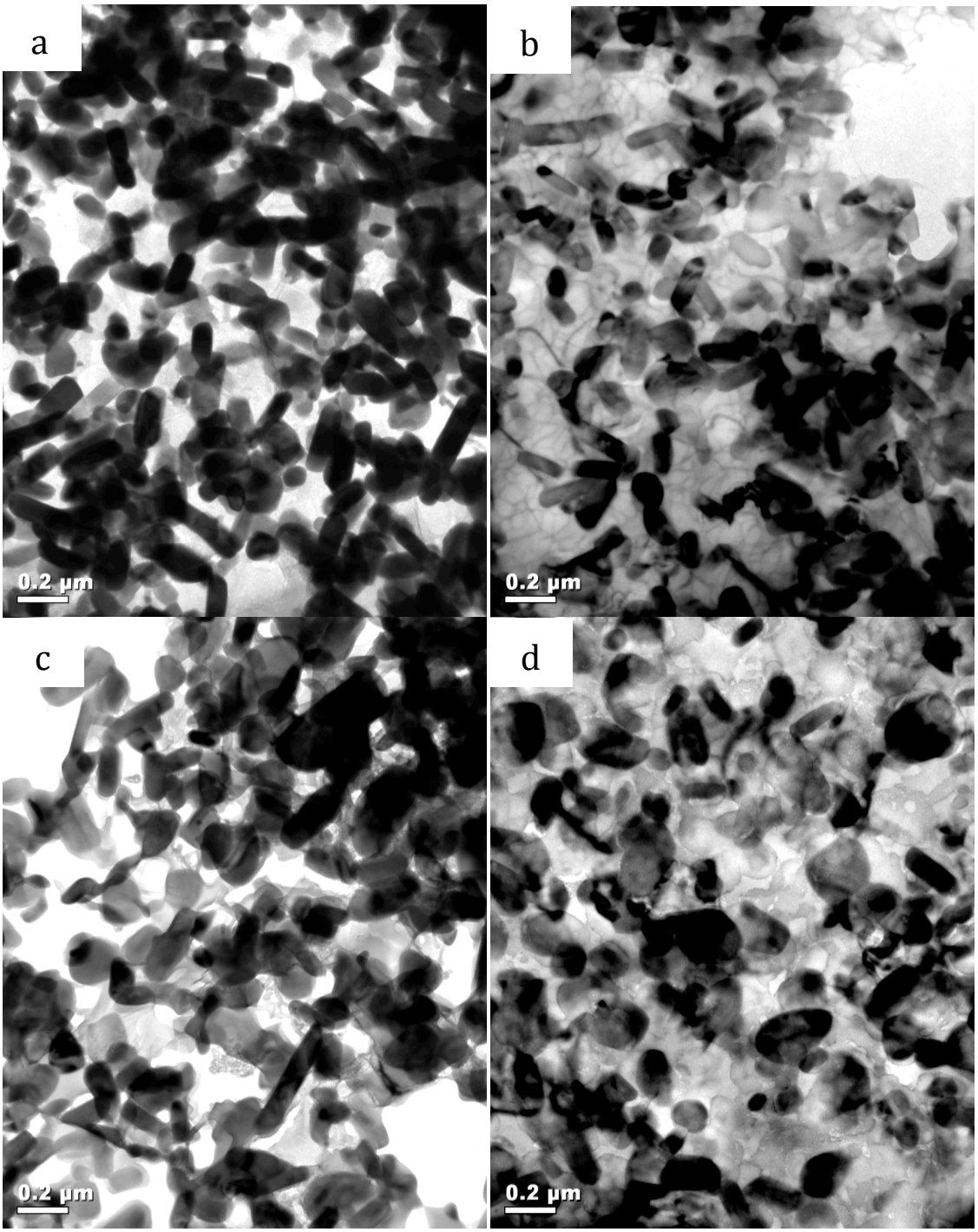

Figure 4.15: Typical bright field TEM images of the microstructures observed in the Al-Ni-Y-Co alloys in the: (a) As-extruded, (b) 43%, (c) 64% and (d) 84% upset forged condition. The electron beam is parallel to the extrusion direction.

the particles now exhibit an ellipsoidal morphology with lengths ranging from 120 to 380 nm. Only a few particles exhibit the rod-shaped morphology with lengths ranging from 150 to 400 nm and thicknesses ranging from 60 to 130 nm. The apparent change in morphology is consistent with that expected after a rotation of the particles because projection effects will take place in the TEM. Finally, after a forging upset of 84%, the majority of the $Al_{19}Ni_5Y_3$ particles have an equiaxed or ellipsoidal morphology as revealed in Figure 4.15d. The ellipsoidal particles have lengths ranging from 150 to 380 nm, and the rod-shaped particles have lengths ranging form 120 to 400 nm and thickness ranging from 50 to 130 nm. The particle size and morphology trends observed in these TEM results are fairly consistent with those observed in the BSE SEM images.

Tracking the change in orientation of the $Al_{19}Ni_5Y_3$ phase from the as-extruded to the 84% upset forged condition suggests that close to a 90 degree rotation of the plates has occurred during processing. However, this rotation can only be inferred from the results of SEM and TEM imaging because the particles are being viewed either in section or projection. As a result, three-dimensional tomography using the FIB was performed to reconstruct the microstructure in three-dimensions to better analyze the changes that occur to the $Al_{19}Ni_5Y_3$ phase after forging.

4.3 **Three-dimensional Tomography**

Three-dimensional tomographic techniques were used to analyze the sub-surface microstructure of the Al-Ni-Y-Co alloys after extrusion and forging. Serial sectioning using the FIB, which consisted of milling thin layers of material from the region of interest and using the SEM to acquire an image of each freshly milled surface, was used

to generate stacks of images revealing the sub-surface microstructure of the material. The FIB was set to mill 10 nm thick slices and each image stack contained 200 images. The orientation of the front cross section is such that it is being viewed parallel to the extrusion direction (i.e. the extrusion direction is normal to the plane of the image coming towards the viewer). This orientation is similar to the TEM images in Figure 4.15 in which the direct beam is parallel to the extrusion direction.

The raw secondary electron SEM images acquired during serial sectioning of the as-extruded, 43%, 64% and 84% upset forged materials are shown in Figures 4.16 – 4.19, respectively. Since there are 200 images in each data set, six representative images were selected for each material: slice numbers 1, 40, 80, 120, 160 and 200 are shown. These are images of the milled front face of the pier during serial sectioning. These images also include the Pt strap at the top of the pier and a portion of the trench to left and right sides of the pier. All of the images in Figures 4.16 – 4.19 were acquired at the same magnification and electron beam conditions, and they have not been aligned nor corrected for foreshortening. There were three main reasons for using this particular magnification for these images: to include as much of the pier's front face in the field of view (FOV) as possible, to include part of the edges of the pier to assist in the alignment procedure, and to give sufficient space for the pier to move within the FOV in-case there was any drift during serial sectioning.

The contrast in the microstructure is consistent with that observed in the BSE SEM images in Figures 4.7 – 4.14: bright $Al_{19}Ni_5Y_3$ plates surrounded by the darker gray Al matrix. Although the contrast in SE SEM images is mainly attributed to topographical effects, that cannot be the case here because the front face of the pier is

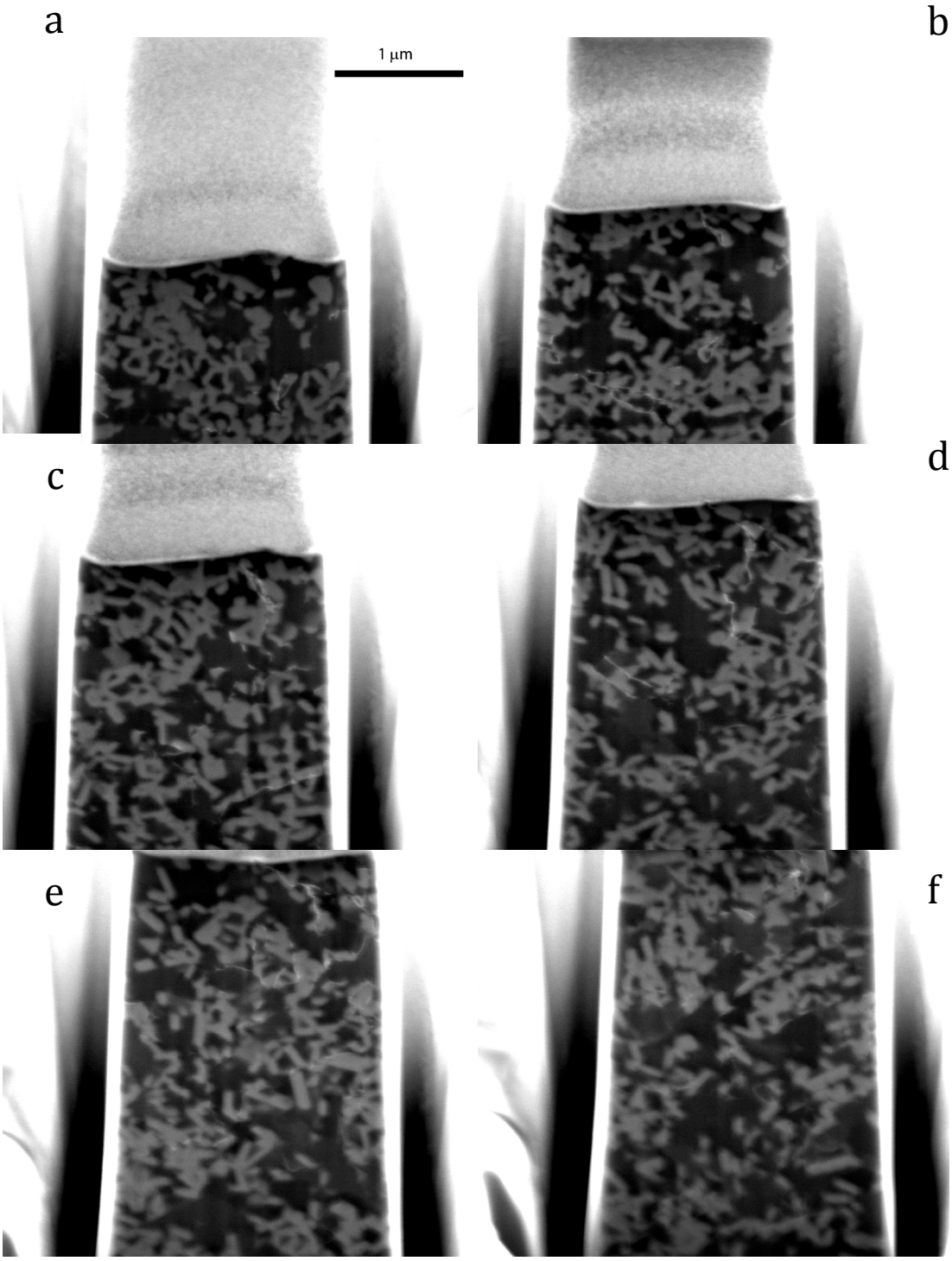

Figure 4.16: Electron beam images acquired of the pier's front face during serial sectioning of the as-extruded Al-Ni-Y-Co alloy. (a) Image 1, (b) Image 40, (c) Image 80, (d) Image 120, (e) Image 160, (f) Image 200.

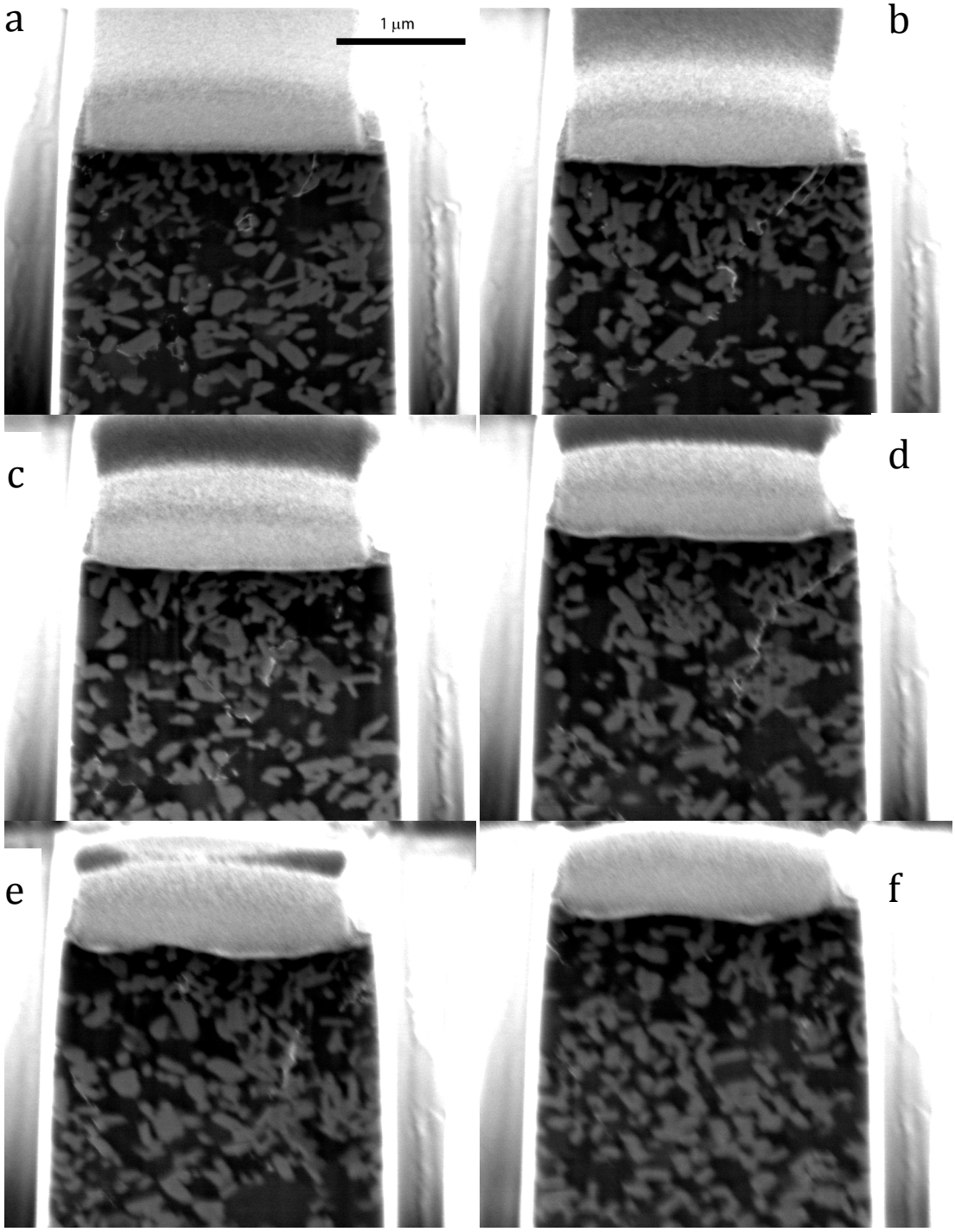

Figure 4.17: Electron beam images acquired of the pier's front face during serial sectioning of the 43% upset forged Al-Ni-Y-Co alloy. (a) Image 1, (b) Image 40, (c) Image 80, (d) Image 120, (e) Image 160, (f) Image 200.

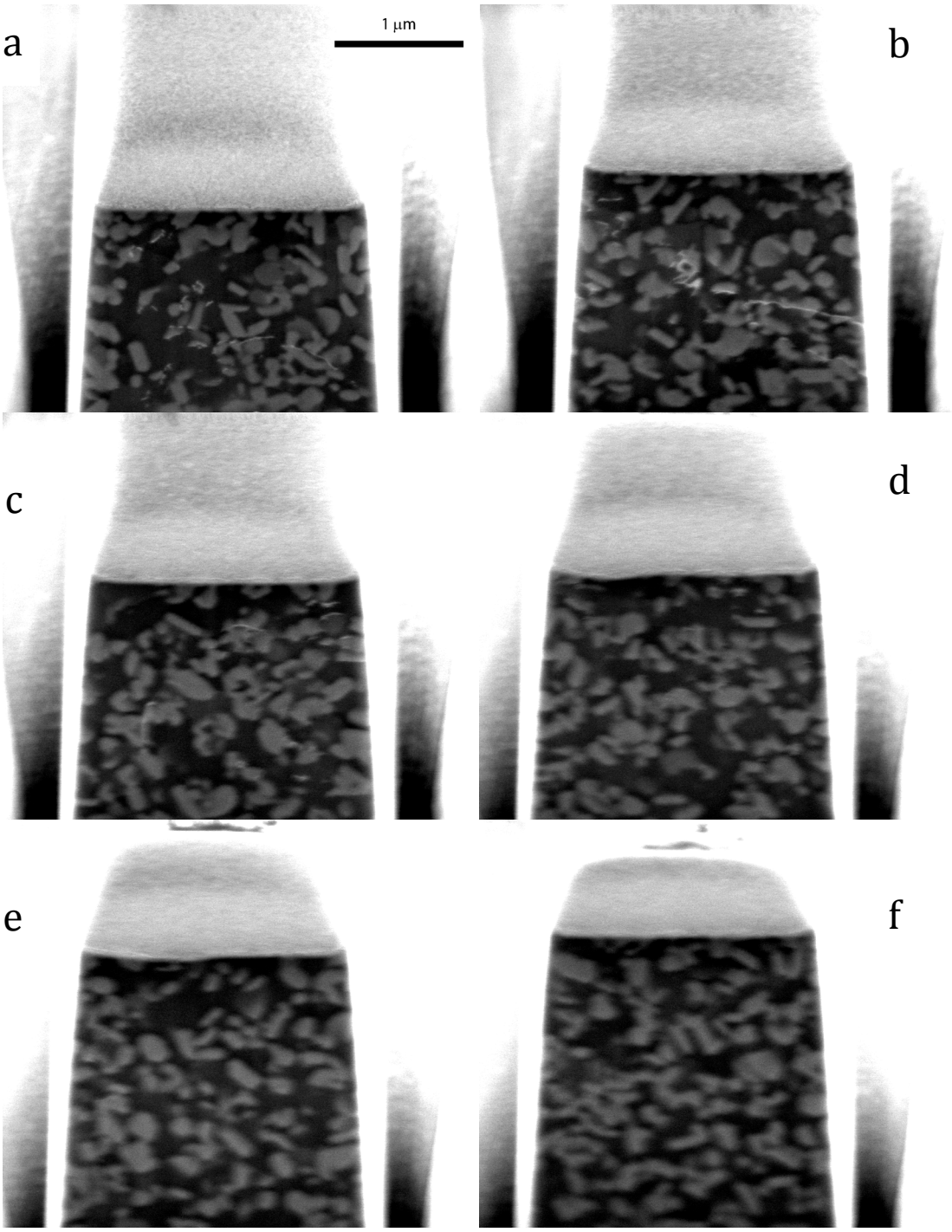

Figure 4.18: Electron beam images acquired of the pier's front face during serial sectioning of the 64% upset forged Al-Ni-Y-Co alloy. (a) Image 1, (b) Image 40, (c) Image 80, (d) Image 120, (e) Image 160, (f) Image 200.

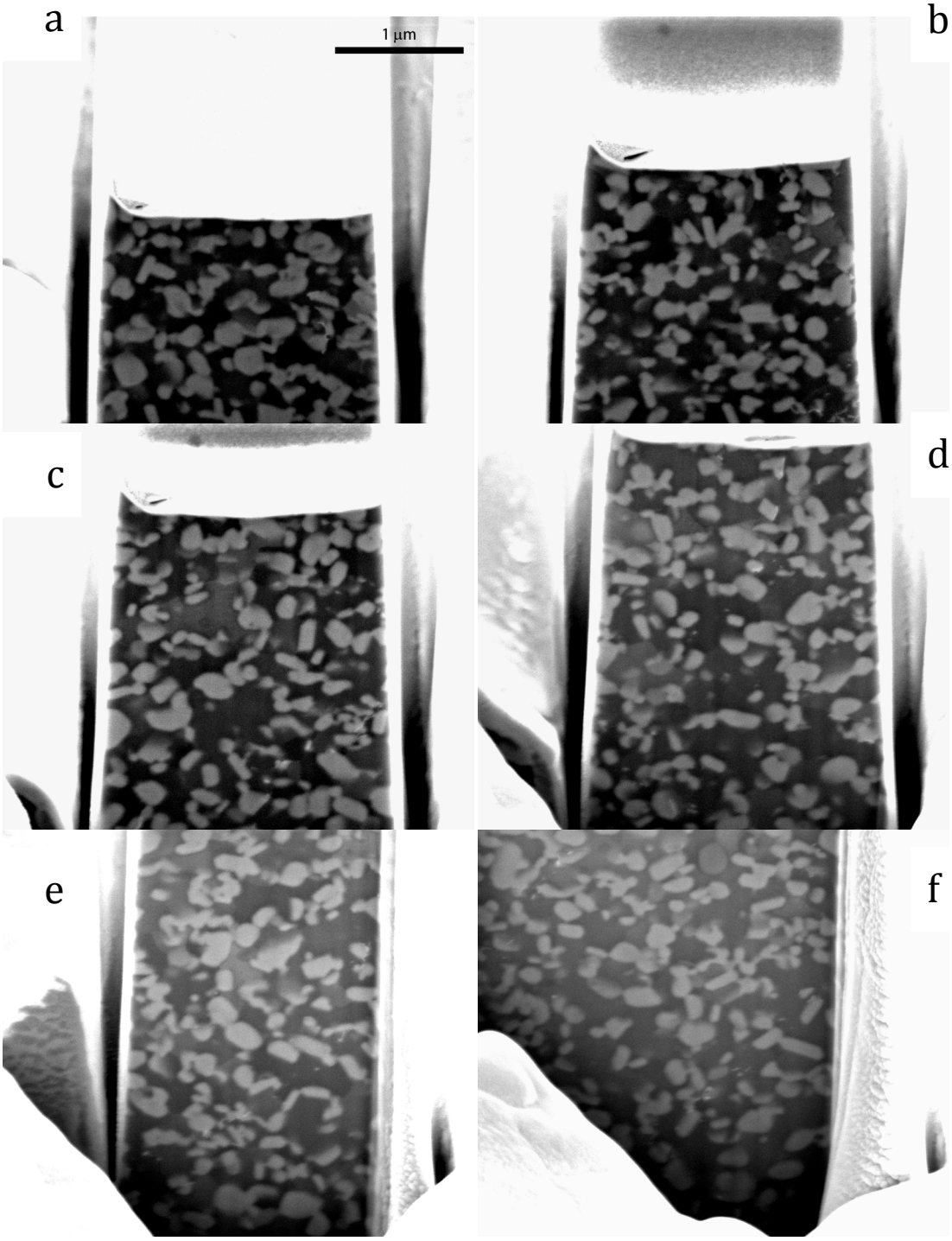

Figure 4.19: Electron beam images acquired of the pier's front face during serial sectioning of the 84% upset forged Al-Ni-Y-Co alloy. (a) Image 1, (b) Image 40, (c) Image 80, (d) Image 120, (e) Image 160, (f) Image 200.

flat. The Pt strap provides protection to the pier from ion beam damage during sectioning. The strap also planarizes the pier allowing for a smooth, straight cut down the front cross section. Therefore, the contrast must be attributed to work function effects in which the bonding in the two phases (Al and $Al_{19}Ni_5Y_3$) much be significantly different allowing more secondary electrons to escape the $Al_{19}Ni_5Y_3$ phase causing it to appear brighter.

The front face of the pier was set to be near the center of the FOV as seen in Figure 4.16a. However, as the sectioning process continued the front face of the pier appears to shift towards the top of the images. This movement continues throughout the sectioning process as shown in Figures 4.16b – 4.16f, such that the last image of the stack has part of the original cross section out of the FOV. The same effect is seen in Figure 4.19 but to a greater extent where the top portion of the pier is no longer visible fewer sections. This upwards movement is caused by the removal of material in conjunction with the orientation of the front face with respect to the electron beam. As thin slices of material are removed during sectioning, the front face of the pier will recede into the trench. However, the electron beam is not perpendicular to the front face but is inclined at 52° with respect to it. Therefore, instead of the front face simply moving into the plane of the image it will slowly jog upwards as seen in Figures 4.16 and 4.19. Another notable movement in the cross section is a left/right shift in the pier. This lateral movement is obvious by comparing the pier's side edges in Figures 4.16a, 4.16c and 4.16e, where the successive images are not aligned with the previous ones. In Figure 4.16, the lateral movement is almost random and does not continue in any particular direction. A lateral movement is also observed in Figure 4.19; however, it is consistent such that the pier is

drifting slowly towards the right side. The challenges associated with these and other types of drifts will be discussed in more detail in section 4.4. These challenges were overcome during the acquisition of the data sets for Figures 4.17 and 4.18 by manually readjusting the electron beam shift during sectioning, which is the reason why there is little lateral shift and the top edge of the front face remains within the FOV.

The distribution and morphology of the $Al_{19}Ni_5Y_3$ phase in Figures 4.16 – 4.19 is complimentary to that observed in the TEM images in Figure 4.15. All of the microstructures consist of a high volume fraction of the $Al_{19}Ni_5Y_3$ phase in the Al matrix. In the as-extruded material the $Al_{19}Ni_5Y_3$ phase exhibits mainly a rod-shaped morphology throughout all of the images in the data set as shown in Figure 4.16. This constant morphology exhibited within the microstructure further suggests that the rods are aligned with the extrusion direction. After a forging upset of 43%, the microstructures shown in Figure 4.17 reveal that only a slight change in the morphology of the plates has occurred. The $Al_{19}Ni_5Y_3$ phase for the most part remains rod-shaped with a few exhibiting an ellipsoidal morphology. However, as seen in the BSE SEM and TEM images, the $Al_{19}Ni_5Y_3$ phase shows a significant change in morphology after the 64% upset forging. Throughout the microstructures shown in Figure 4.18 for the 64% upset forged material, the $Al_{19}Ni_5Y_3$ phase appears as ellipsoidal particles. This is consistent with the sectioning effects that would occur in viewing a portion of a rotated plate. Finally, the $Al_{19}Ni_5Y_3$ phase exhibits an equiaxed and ellipsoidal morphology after the largest upset forging of 84% as revealed in Figure 4.19.

It is important to note that the microstructures in Figure 4.16 – 4.19 have not been corrected for the foreshortening effects explained in Chapter 3. Therefore, these raw

images do not reveal the true morphology of the particles because the images are compressed along the vertical axis. Figure 4.20 contains a selected image from each of the four data sets after all processing and correction of foreshortening was performed. These four images are distorted representations of the microstructure, which is still consistent with that observed in all of the other data presented.

Three-dimensional reconstructions – The three-dimensional reconstructions of each data set were made using corrected images such as those shown in Figure 4.20. The volumes reconstructed represent a subset of the total $Al_{19}Ni_5Y_3$ particles in the region of interest. Stacking the selections made of individual particles appearing in successive images formed the surfaces seen in the reconstructions. During preliminary work it was found that the lengths and thicknesses of the $Al_{19}Ni_5Y_3$ phase were not consistent with those observed in the SEM and TEM. The size of the particles parallel to the sectioning direction appeared to be compressed. This foreshortening of particles means that the nominal slice thickness of 10 nm used during serial sectioning is not the correct value. As a result, the particle size data from SEM and TEM results were used to correct the slice thickness of the reconstructions so that the particle dimensions along the sectioning direction were correct. This gave a correction factor for the as-extruded, 43% and 64% upset forged reconstructions of approximately 1.5, while the correction factor for the 84% upset forged reconstruction was approximately 1.7.

The final three-dimensional reconstructions of the $Al_{19}Ni_5Y_3$ phase in the as-extruded, 43%, 64% and 84% upset forged materials are shown in Figures 4.21, 4.22, 4.23 and 4.24, respectively. The front view in Figures 4.21a, 4.22a, 4.23a and 4.24a are

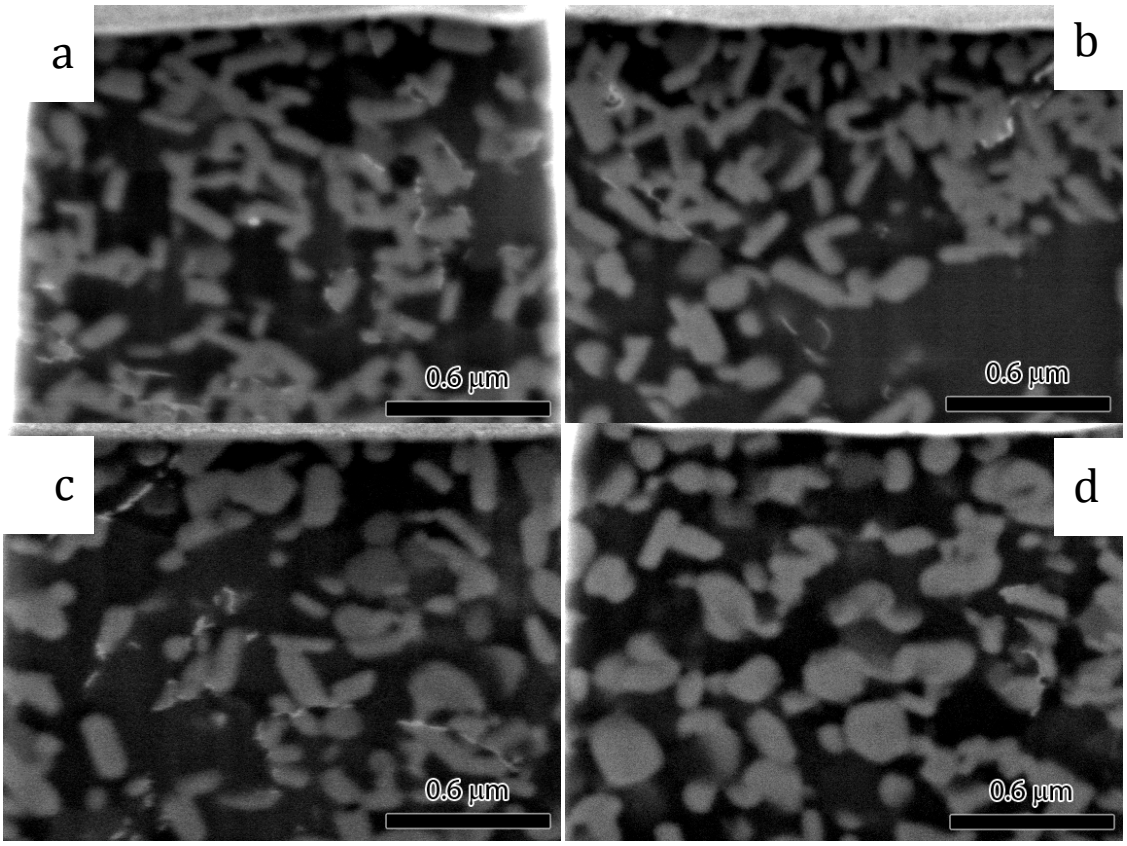

Figure 4.20: SE SEM images taken from the face of the FIB cut pier of the (a) as extruded, (b) 43%, (c) 64% and (d) 84% upset forged. The image boundaries enclose the region used for the three-dimensional reconstruction.

oriented such that the extrusion direction is normal to the page. The area surrounded by the box in these figures is approximately 2 μm by 2μm. The side views shown in Figures 4.21b, 4.22b, 4.23b and 4.24b were generated by rotating the front view along the vertical axis by 90-degrees towards the right. The top views shown in Figures 4.21c, 4.22c, 4.23c and 4.24c were generated by rotating the front view along the horizontal axis by 90-degrees towards the bottom of the page.

In the as-extruded material, the particles can be seen as thin rods from the front view in Figure 4.21a, which is consistent with observations made from SEM and TEM experiments, but it does not reveal anymore than what could have been inferred from SEM and TEM images. However, the orientation relationship becomes clear when viewing the model from other directions, such as the side and top views in Figures 4.21b and 4.21c, respectively. These two views reveal the sub-surface microstructure and morphology of the $Al_{19}Ni_5Y_3$ phase, which is not possible from SEM and TEM images. The combination of the front, side and top views clearly show that the $Al_{19}Ni_5Y_3$ phase is indeed aligned with the extrusion direction. The three-dimensional reconstruction in Figure 4.22 of the 43% upset forged microstructure show that there is no significant change to the $Al_{19}Ni_5Y_3$ phase. Some the particles in the front view are viewed edge-on and appear as thin rods, but there are others that exhibit ellipsoidal morphologies. However, when analyzing the particles from the side view in Figure 4.22b and the top view in Figure 4.22c, it becomes clear why there is a mixed morphology. The particles in Figures 4.22b and 4.22c are generally aligned with the extrusion direction, which is consistent with results obtained from SEM and TEM that showed no significant change in morphology. However, it can be seen that some of the particles exhibit a slight

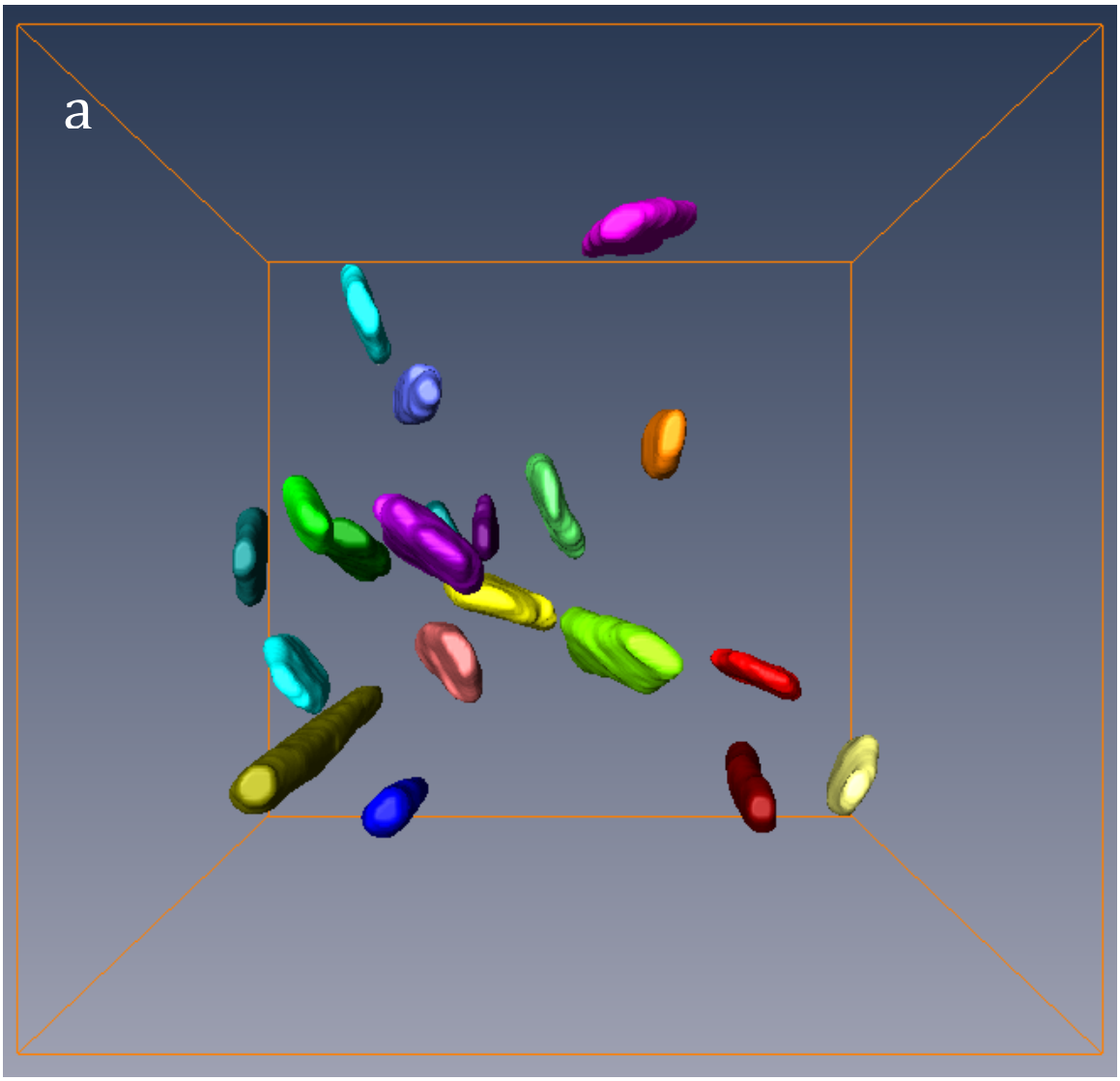

Figure 4.21: Three different views of the three-dimensional reconstruction of the $Al_{19}Ni_5Y_3$ plates in the as-extruded Al-Ni-Y-Co alloy using the images acquired during serial sectioning. a) Front View (The area of the box is approximately 2 μm by 2μm), b) Side View and c) Top View.

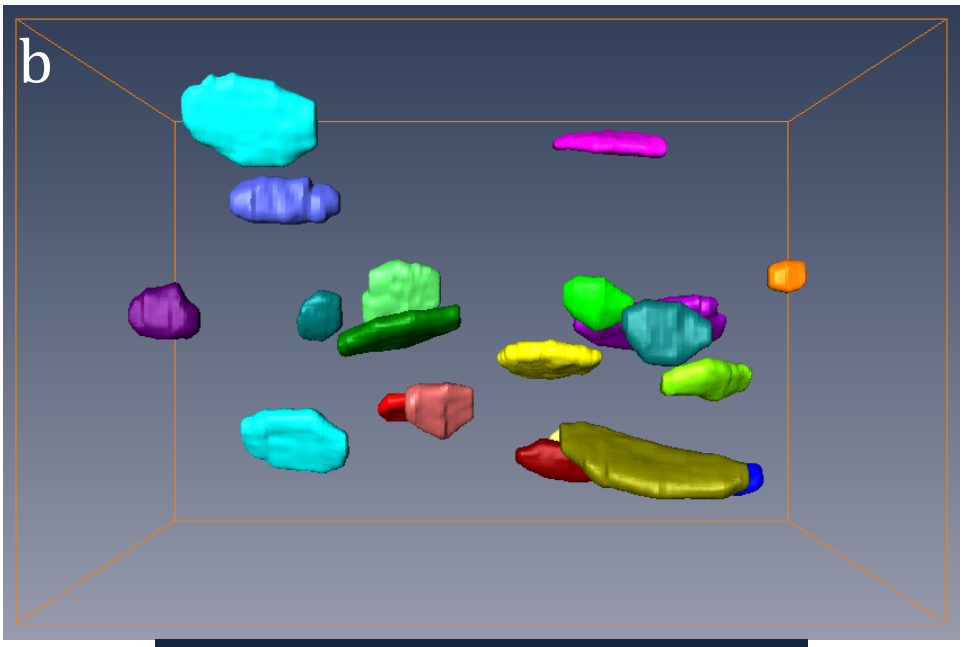

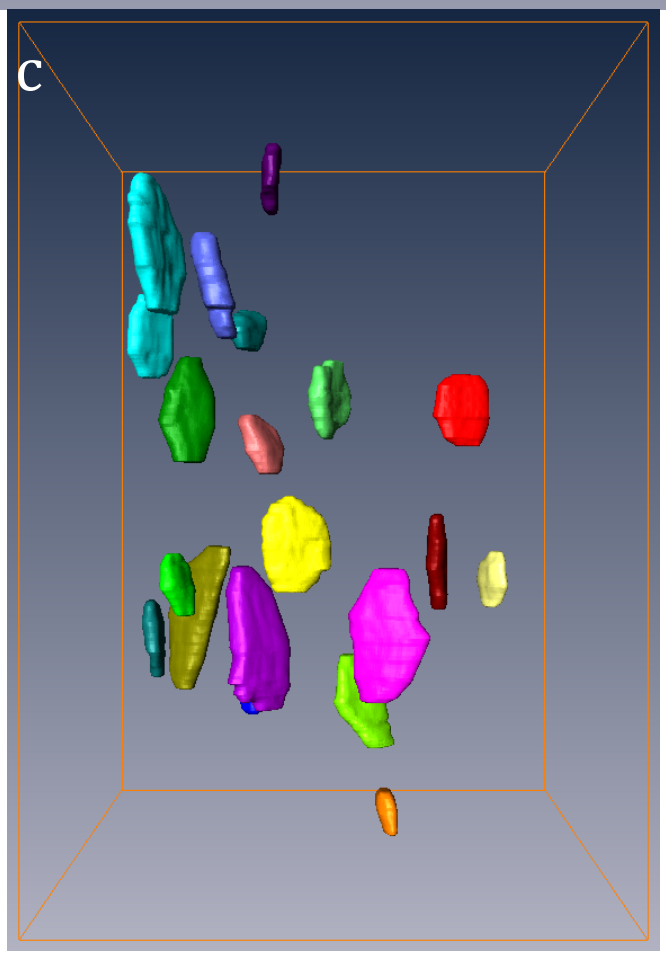

Figure 4.21: Three different views of the three-dimensional reconstruction of the $Al_{19}Ni_5Y_3$ plates in the as-extruded Al-Ni-Y-Co alloy using the images acquired during serial sectioning. a) Front View (The area of the box is approximately 2 μm by 2μm), b) Side View and c) Top View.

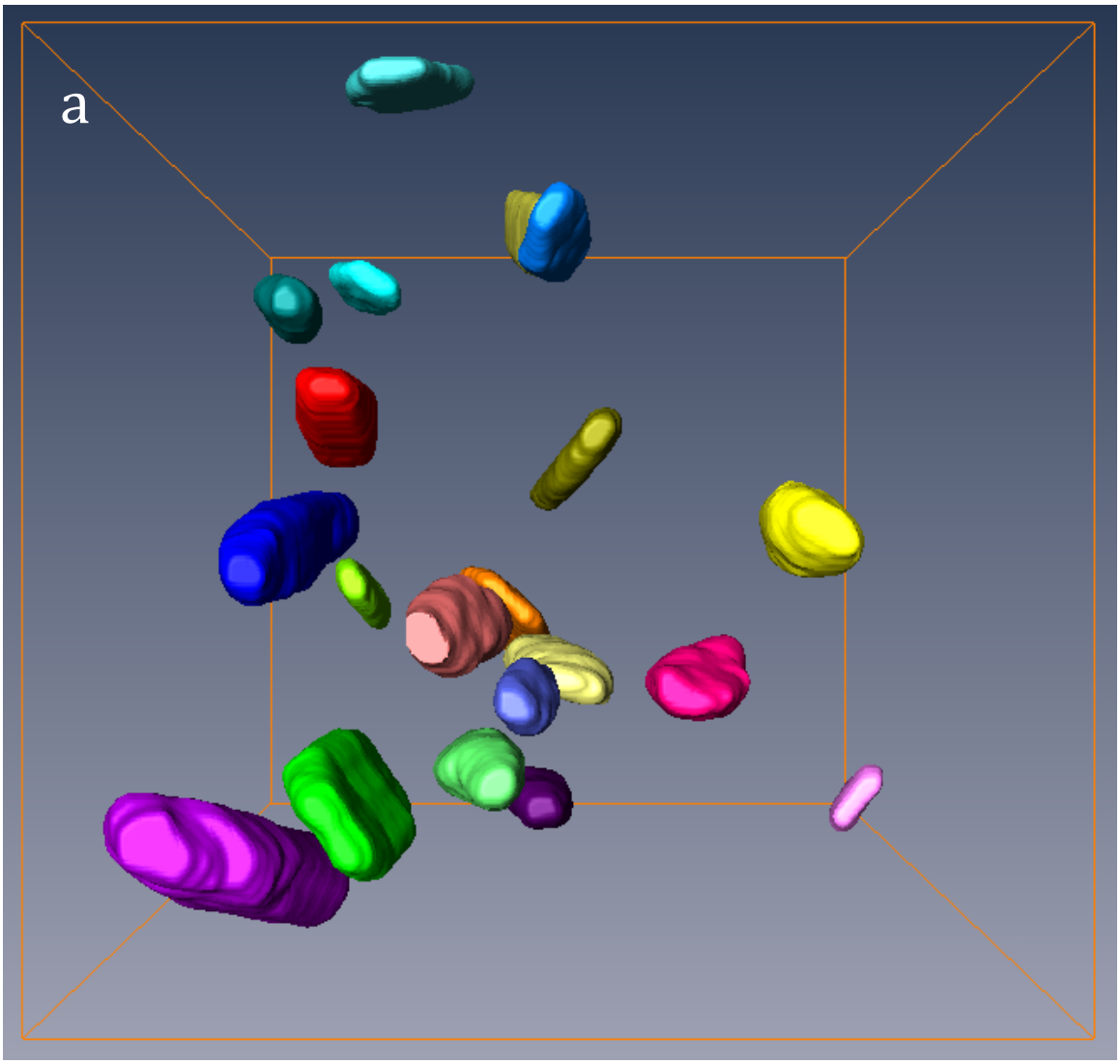

Figure 4.22: Three different views of the three-dimensional reconstruction of the $Al_{19}Ni_5Y_3$ plates in the 43% upset forged Al-Ni-Y-Co alloy using the images acquired during serial sectioning. a) Front View (The area of the box is approximately 2 μm by 2μm), b) Side View and c) Top View.

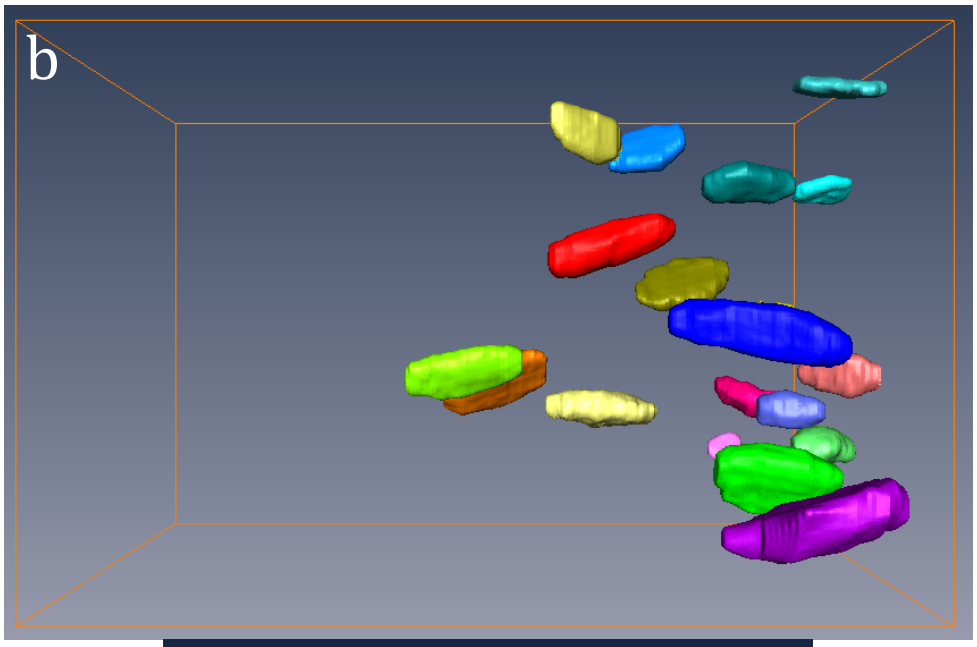

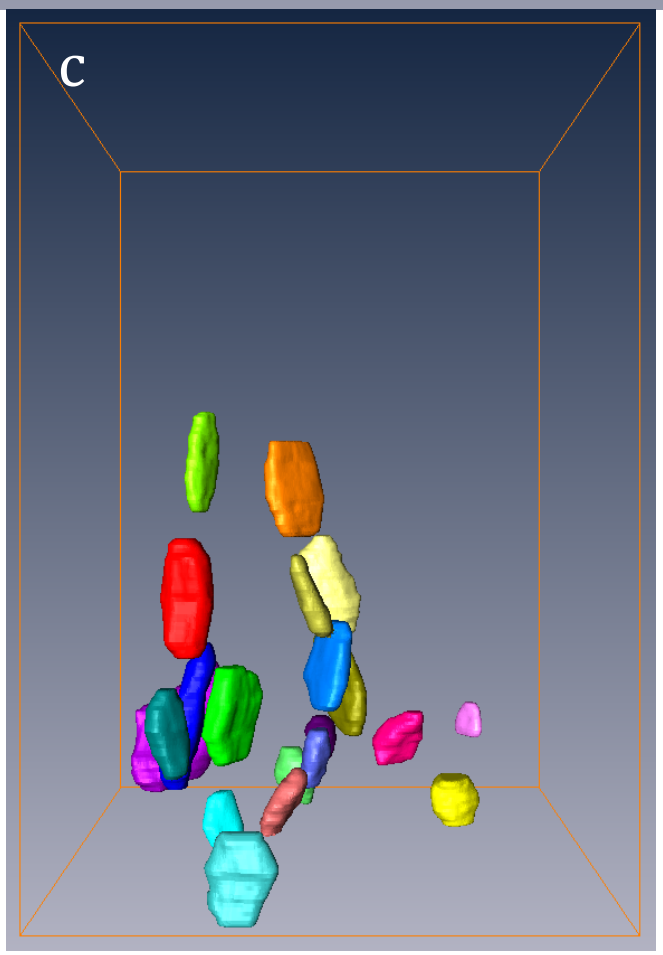

Figure 4.22: Three different views of the three-dimensional reconstruction of the $Al_{19}Ni_5Y_3$ plates in the 43% upset forged Al-Ni-Y-Co alloy using the images acquired during serial sectioning. a) Front View (The area of the box is approximately 2 μm by 2μm), b) Side View and c) Top View.

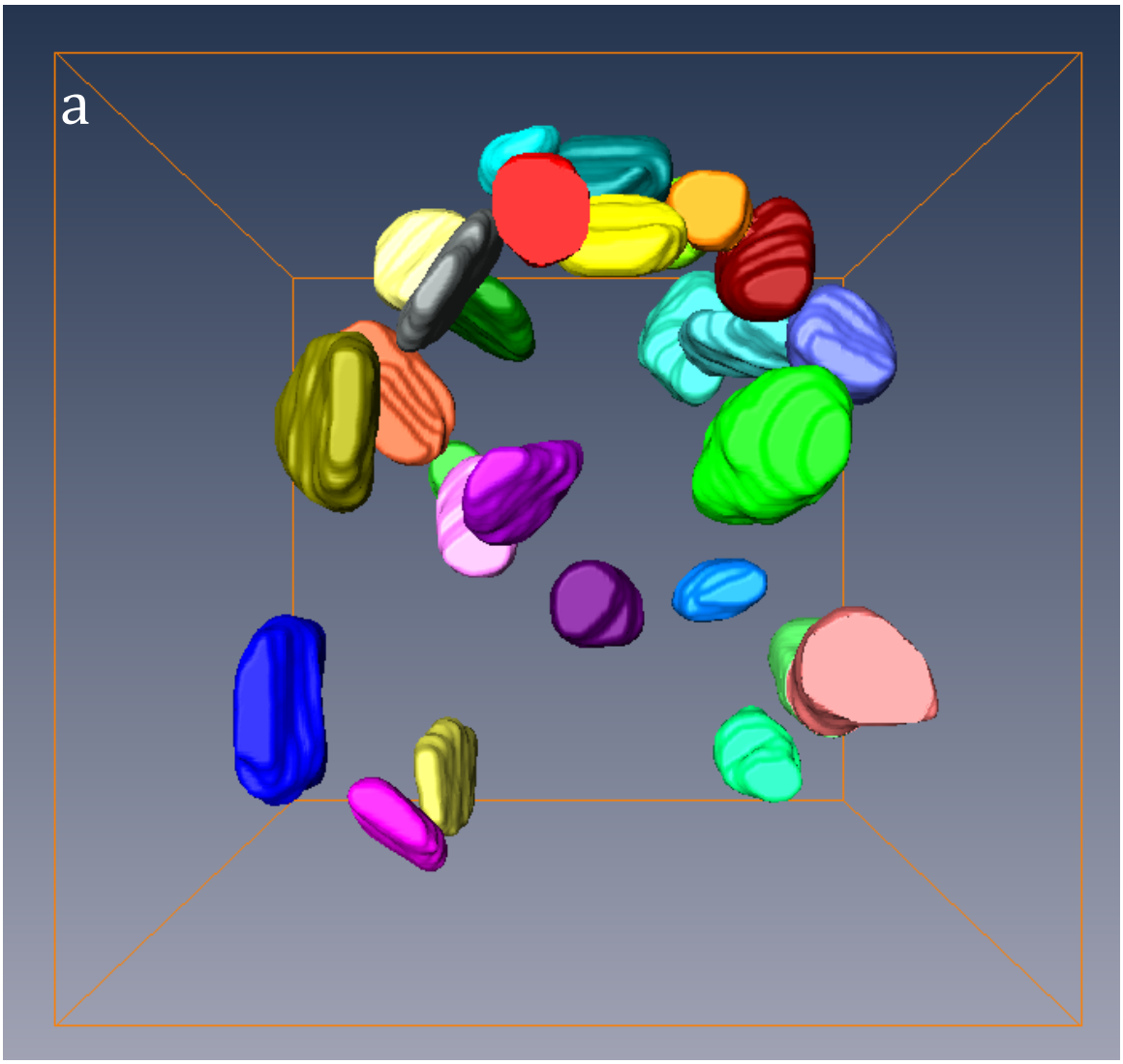

Figure 4.23: Three different views of the three-dimensional reconstruction of the $Al_{19}Ni_5Y_3$ plates in the 64% upset forged Al-Ni-Y-Co alloy using the images acquired during serial sectioning. a) Front View (The area of the box is approximately 2 μm by 2μm), b) Side View and c) Top View.

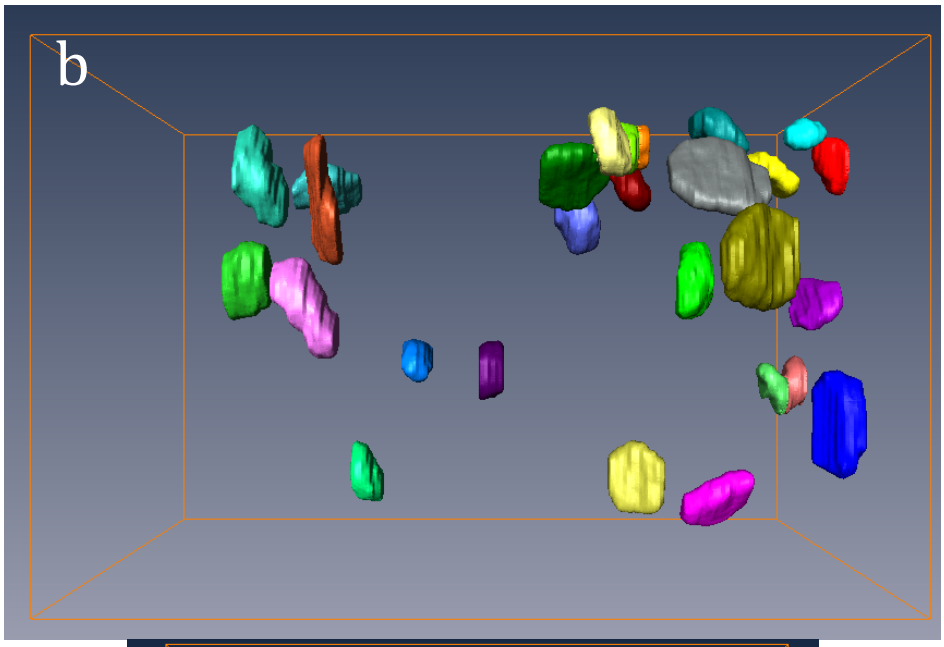

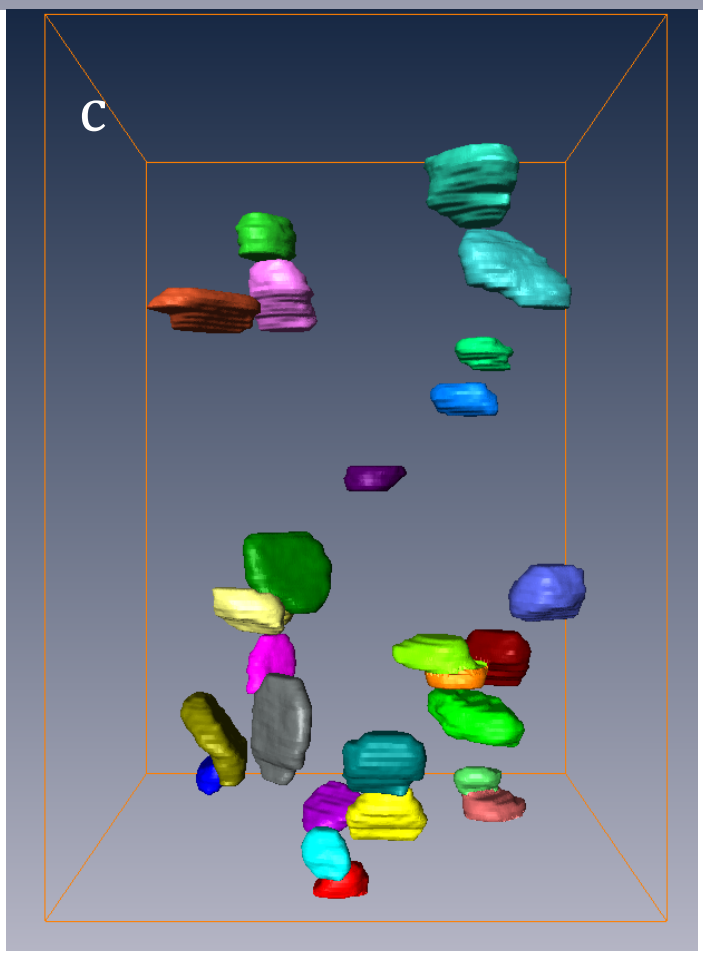

Figure 4.23: Three different views of the three-dimensional reconstruction of the $Al_{19}Ni_5Y_3$ plates in the 64% upset forged Al-Ni-Y-Co alloy using the images acquired during serial sectioning. a) Front View (The area of the box is approximately 2 μm by 2μm), b) Side View and c) Top View.

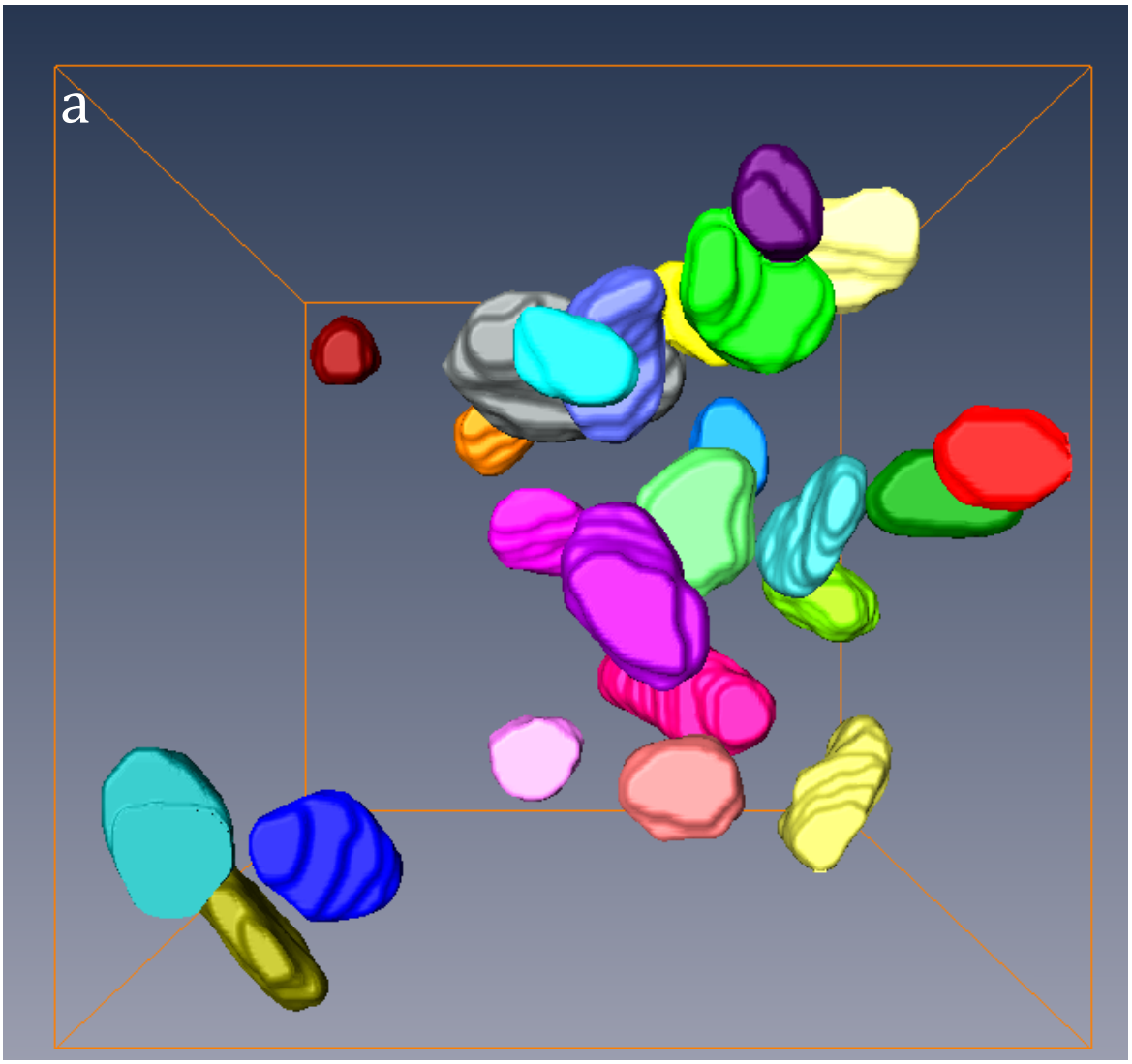

Figure 4.24: Three different views of the three-dimensional reconstruction of the $Al_{19}Ni_5Y_3$ plates in the 84% upset forged Al-Ni-Y-Co alloy using the images acquired during serial sectioning. a) Front View (The area of the box is approximately 2 μm by 2μm), b) Side View and c) Top View.

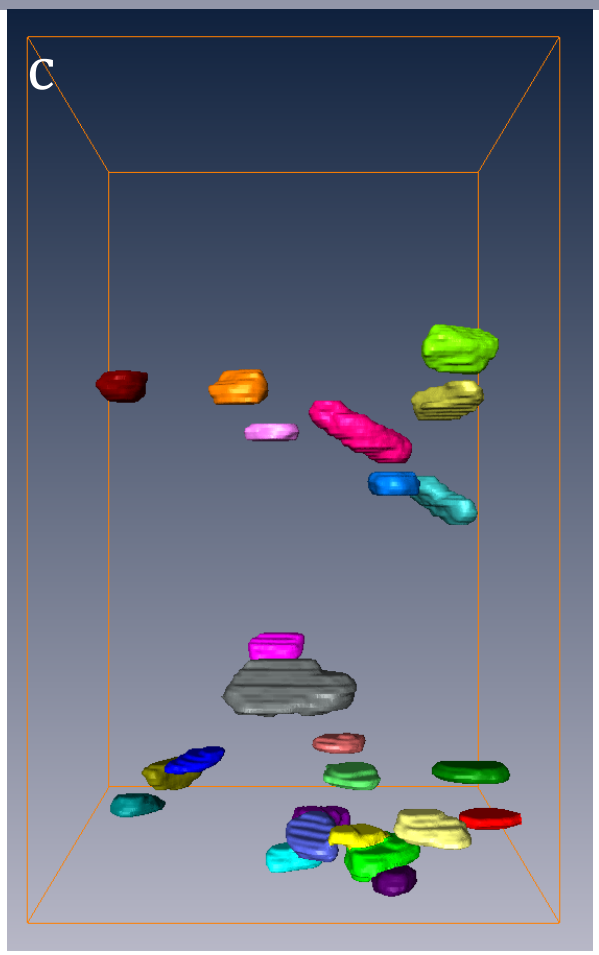

Figure 4.24: Three different views of the three-dimensional reconstruction of the $Al_{19}Ni_5Y_3$ plates in the 84% upset forged Al-Ni-Y-Co alloy using the images acquired during serial sectioning. a) Front View (The area of the box is approximately 2 μm by 2μm), b) Side View and c) Top View.

rotation relative to the extrusion direction, which explains why some appear to be thicker when viewed from the front.

In the reconstruction for the 64% upset forged material, it can be seen in Figure 4.23 that there has been a significant change in the orientation of the $Al_{19}Ni_5Y_3$ phase. The $Al_{19}Ni_5Y_3$ particles in the front view now exhibit more of an ellipsoidal and equiaxed morphology. Their orientation becomes much clearer from the side and top views in Figures 4.23b and 4.23c, respectively. The particles that were ellipsoidal in the front view are actually particles that have been rotated and exhibited the apparent ellipsoidal morphology because they were being viewed in projection. There are also a few examples of $Al_{19}Ni_5Y_3$ plates that have been rotated by approximately 90°, which is evident from particles that exhibit an equiaxed morphology in the front view but are rod-shaped in the side and top views. The most significant change in the particles orientation is observed after the 84% upset forging where the reconstruction is shown in Figure 4.24. Almost all of the particles exhibit an equiaxed morphology from the front view in Figure 4.24a implying that they have rotated 90-degrees during forging. Their orientation is further concluded from the side view in Figure 4.24b and the top view in Figure 4.24c, where the particles that were equiaxed in the front view now are viewed edge-on and show up as rods. The results from these three-dimensional reconstructions are consistent with those found in TEM and SEM images, and reveal conclusively that the particles do indeed rotate after forging.

4.4 Challenges with FIB Tomography

As mentioned in section 4.3, there were some challenges with FIB based tomography. Recall in the description of Figures 4.16 and 4.19 that there was a lateral movement of the pier during sectioning. This lateral movement is obvious by comparing the edges of the pier from one image to another and noticing that they do not match. Fortunately, the random movement was minimal and did not persist in any one direction so that the pier was always within the FOV. The lateral movement in Figure 4.19 was not random between each slice but persisted such that the pier drifted towards the right. It can be seen that part of the trench on the left side was beginning to be milled in Figure 4.19c. In addition, after some time the right side of the pier is no longer being milled because it has moved outside of the ion beam's milling zone as seen in Figure 4.19e. This edge then becomes a site for redeposition and continues to grow as seen in image 200 (Figure 4.19f). There is a large amount of redeposition on the lower left corner and right side of Figure 4.19f, which obscures the microstructure and degrades image quality. Although this drift caused some unwanted effects, there was still a lot of useful information in these data sets.

The drifting of the pier around the FOV posed some challenges as mentioned above, but there were occurrences where the pier would almost completely drift off of the FOV. One example of this is shown in Figure 4.25, which consists of four SE SEM images (Image 1, 8, 15 and 25) selected from a serial sectioning experiment. Image 1 in Figure 4.25a is in the desired position: centered in the FOV to reveal as much of the microstructure as possible while maintaining the pier edges in view for alignment assistance. Image 8 in Figure 4.25b shows a little bit of drift towards the bottom of the

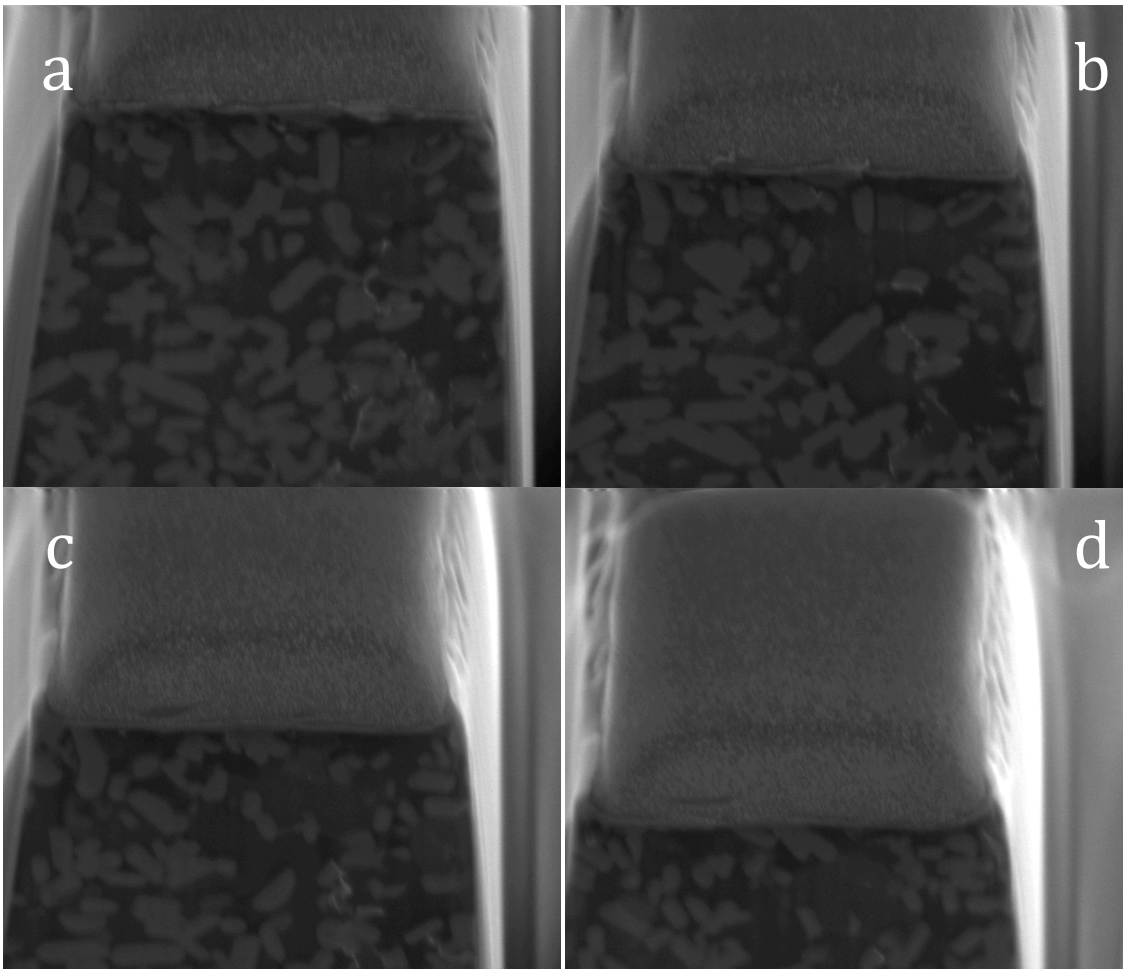

Figure 4.25: Electron beam images acquired of the pier's front face during serial sectioning illustrating the drift of the pier. (a) Image 1, (b) Image 8, (c) Image 15, (d) Image 25.

FOV, but it is of good quality since most of the microstructure is visible. However, this downward drift continues until almost the entire front face of the pier is out of the FOV as seen in Figures 4.25c and 4.25d. This is very problematic because it has occurred after 25 of the 200 slices desired for each data set. Whenever this occurs the serial sectioning routine is stopped and restarted over again. However, there are a limited number of times that this can be done because with every sectioning routine performed material from the pier is being removed. There have been instances where the pier was completely depleted, and the only way to restart is to begin the whole trench milling process from scratch. The specimen used for this experiment was held onto the Al stub by double-sided carbon tape, and after tilting the stage for FIB milling it was believed that the weight of the specimen was causing it to creep downward. This led to the idea of mechanically clamping the specimens to the Al stub as described in Chapter 3. However, after careful analysis of the relationship between the specimen, stage, and electron beam it was determined that gravitational creep cannot cause the movement shown in Figure 4.25. If gravity were really pulling the specimen away, then the movement would actually be in the upward direction, the opposite of that seen in Figure 4.25. The cause is then really due to electron beam or stage drift.

Another example of drift is shown in Figure 4.26, which consists of four SE SEM images selected from a serial sectioning experiment. The drift is towards the bottom left corner of the FOV, and after 32 slices half of the pier's cross section is no longer visible. Two causes for this movement could be either shift of the electron beam or drift in the stage towards the left. SE ion beam images of the pier before and after serial sectioning are shown in Figures 4.27a and 4.27b, respectively. Although it is difficult for the reader

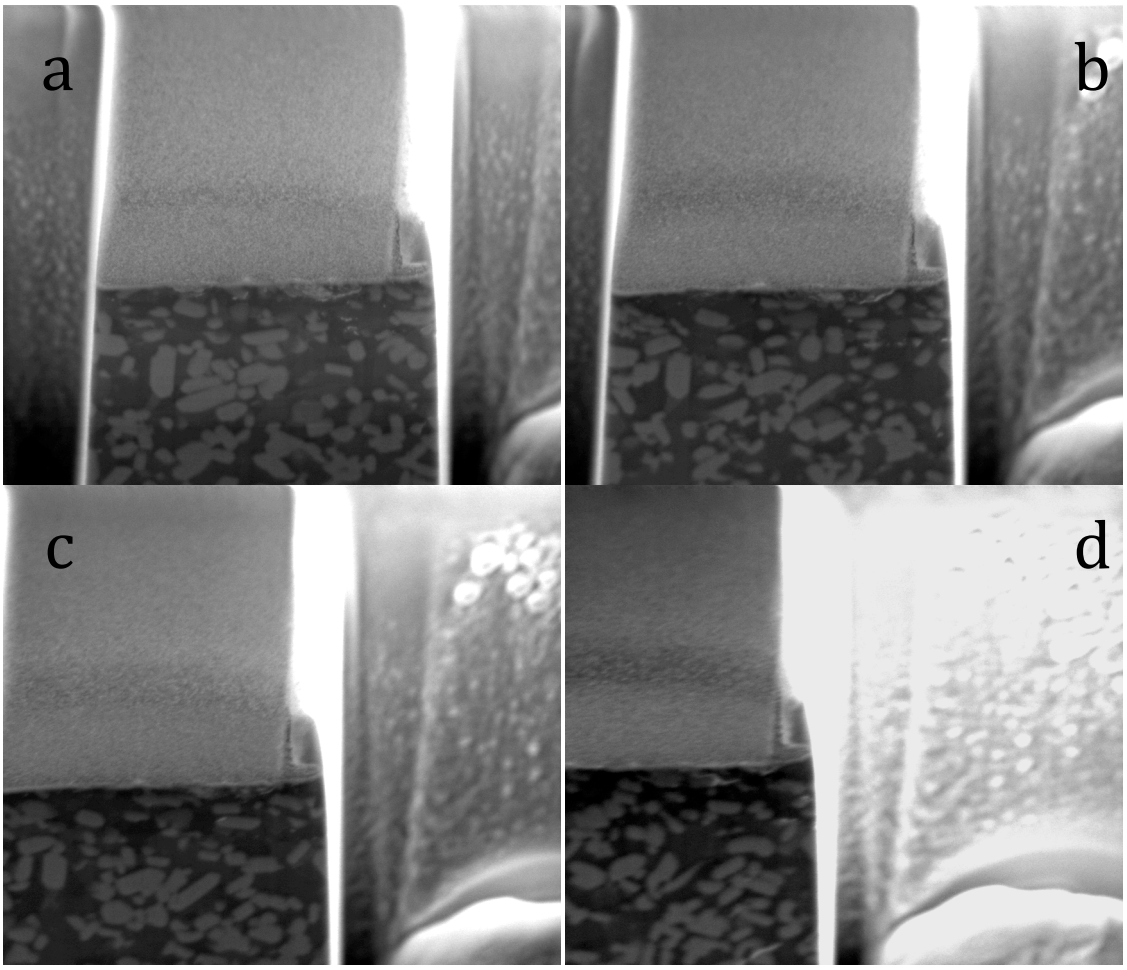

Figure 4.26: Electron beam images acquired of the pier's front face during serial sectioning illustrating the drift of the pier. (a) Image 1, (b) Image 7, (c) Image 14, (d) Image 32.

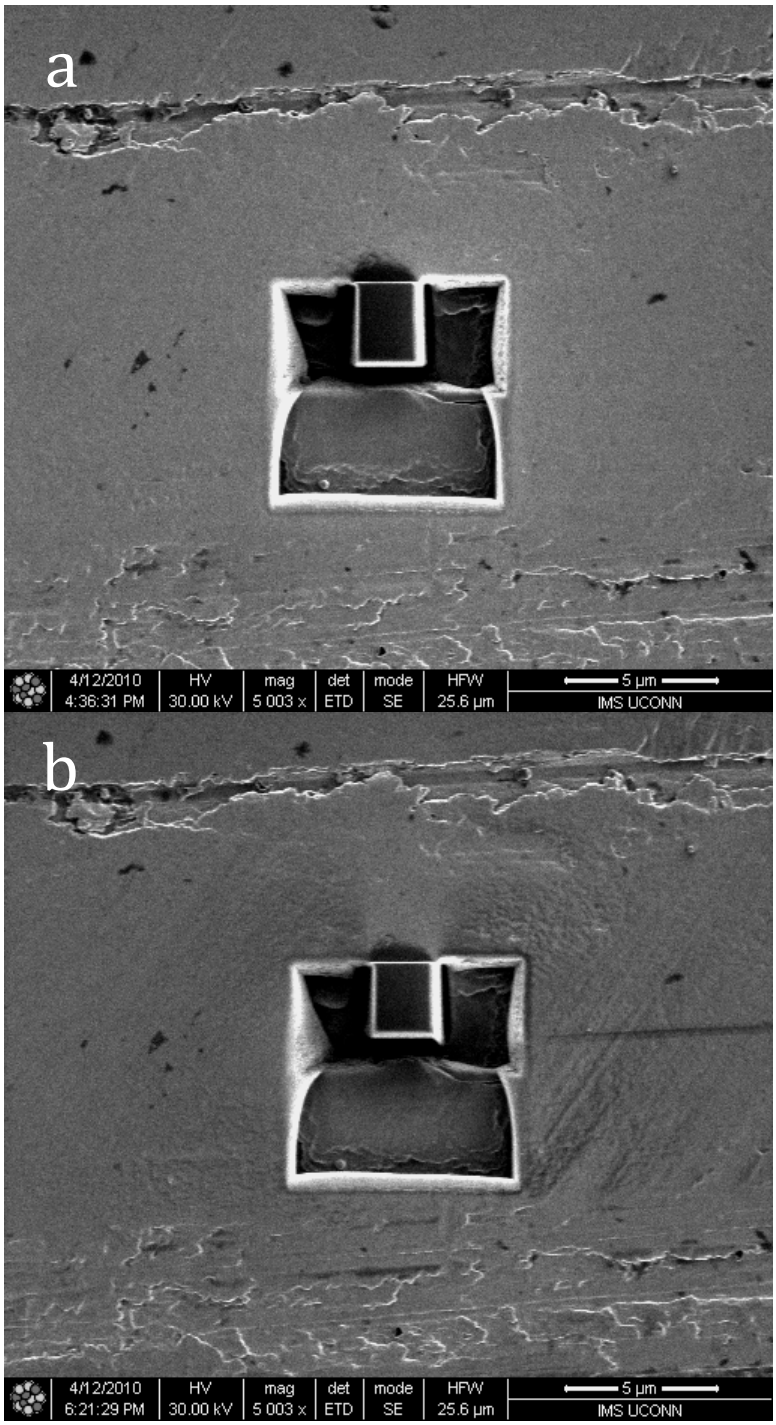

Figure 4.27: SE ion beam images of the pier before (a) and after (b) serial sectioning. Although difficult to see, after serial sectioning (b) the pier has drifted to the right.

to detect, the pier in Figure 4.27b has drifted to the right relative to Figure 4.27a. This is in the opposite direction that is observed in the SE SEM images in Figure 4.26. In addition, redeposition can be seen to develop on the bottom right edge of the pier in Figure 4.27b. If the sectioning process was allowed to continue then the result would have been similar to that in Figure 4.19f.

The final example is shown in Figure 4.28, which is composed of 6 images selected from a serial sectioning data set: image 1, 40, 80, 120, 160 and 200 are shown. Initial results looked very promising: the milled surface was very clean, image quality was very good, and there was very little lateral drift. However, at image 80 shown in Figure 4.28c there is a small lip developing on the right edge of the pier. As the sectioning process continued, the lip swells due to redeposition and continues to grow throughout the remainder of the sectioning. In addition, redeposition is also occurring on the bottom edge of the pier, which is first observed in Figure 4.28d and continues to buildup till the end. The consequence of the redeposition is degradation of image quality.

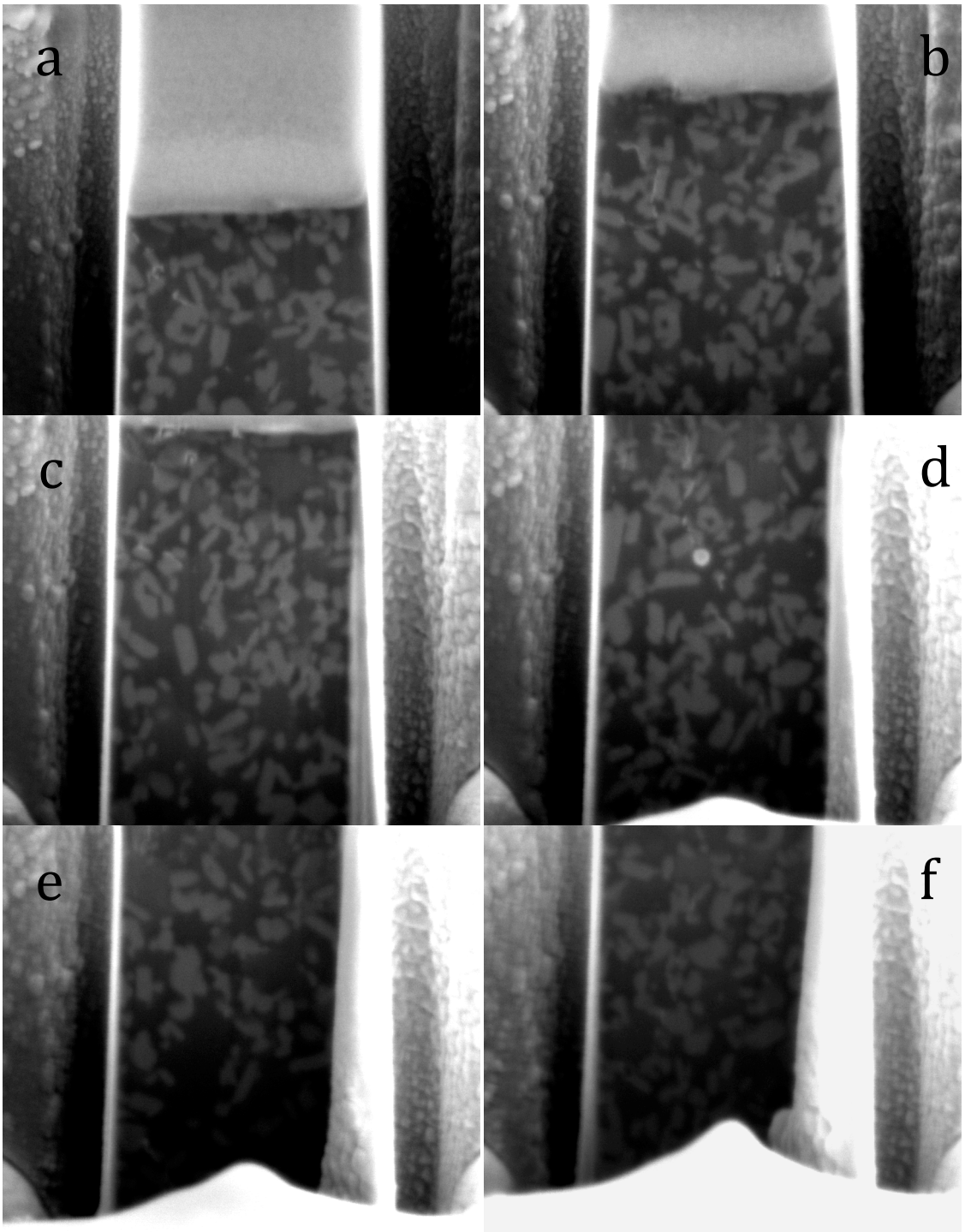

Figure 4.28: Electron beam images acquired of the pier's front face during serial sectioning showing the effect of drift and redeposition on the quality of images. (a) Image 1, (b) Image 40, (c) Image 80, (d) Image 120, (e) Image 160, (f) Image 200.

Chapter 5: Discussion

5.1 **Starting Microstructure**

5.2 **Forged Microstructure**

5.3 **FIB Tomography**

Chapter 5: Discussion

The objective of this thesis was to study the microstructural evolution in forged Al-11Ni-13Y-1Co wt% (Al-6.0Ni-4.7Y-0.5Co at%) alloys. The main emphasis was on the characterization of the orientation adopted by the precipitates with respect to the external axes of the extrudate after different forging upsets. It is very important to investigate the formability of these devitrified alloys because their microstructures cannot be modified like other Al alloys. Traditional Al alloys can have their microstructures "reset" by solution heat treatment and re-precipitation. This allows for much more flexibility in manufacturing of components and provides a wide range of mechanical properties. However, these kinds of heat treatments cannot be applied to devitrified Al-RE-TM alloys because the RE and TM contents in these alloys far exceed the corresponding solubility limits. The main consequence of this is that the volume fraction of each of the phases formed after devitrification is essentially fixed.

5.1 Starting Microstructure

As discussed in section 2.2.4, the microstructures in previously studied devitrified Al alloys typically consisted of three phases: Al grains, the ternary $Al_{19}Ni_5Y_3$ phase, and a binary phase, such as Al_3Ni or Al_3Y, depending on the alloy composition. The starting microstructure (as-extruded condition) of the material in this study consisted only of two phases: particles of the $Al_{19}Ni_5Y_3$ phase surrounded by an Al matrix, as described in section 4.1. No binary Al_3X phase was observed in these materials. The measured volume fraction of the $Al_{19}Ni_5Y_3$ phase was 0.44. The $Al_{19}Ni_5Y_3$ particles had a strong tendency to be aligned along the extrusion direction, which is clear from the three-

dimensional reconstructions shown in section 4.3. This orientation is to be expected from a material that has been extruded. As the material is being extruded, the softer Al matrix will flow plastically through the extrusion die while the harder $Al_{19}Ni_5Y_3$ particles will tend to rotate and align themselves along the extrusion direction.

The volume fraction of the phases in this material was calculated from the composition in atomic percent by partitioning the elements according to the stoichiometry of the phases. Then, using the lattice parameter of these phases, and the number of formula units in each unit cell, the volume fractions can be calculated. There were four assumptions made for this calculation:

1) No solubility of Ni, Y and Co into Al.
2) Co atoms were assumed to act like Ni atoms.
3) All of the Ni atoms would be preferentially exhausted to form the $Al_{19}Ni_5Y_3$ phase.
4) The remaining Y atoms would then form the binary phase, Al_3Y.

Al has a face centered cubic structure with lattice parameter of 0.4049 nm. The $Al_{19}Ni_5Y_3$ phase has an orthorhombic crystal structure with lattice parameters a, b and c of 0.403 nm, 1.598 nm and 2.689 nm, respectively, and the unit cell contains four formula units. The Al_3Y phase has an hexagonal crystal structure with lattice parameters a and c of 0.6204 nm and 2.1184 nm, respectively and the unit cell contains nine formula units. Thus, the calculated volume fractions of the Al, $Al_{19}Ni_5Y_3$, and Al_3Y phases are 0.62, 0.34, and 0.038, respectively. There is a significant difference between the measured and calculated values of the volume fraction for the $Al_{19}Ni_5Y_3$ phase, with the

measured volume fraction being 10 vol.% greater than the calculated value. There are two possible explanations for this difference.

One possible reason is that there are random and/or systematic errors in the measured volume fraction. The measured value was obtained using SEM images under the assumption that the area fraction of the precipitates is equal to the volume fraction. However, there is an inherent variability in the microstructure of these materials. This means that the volume fraction measured in one image will be different from that measured in another because the micrographs contain a different number visible particles. This causes random errors in the measurement. On the other hand, systematic errors can be introduced during the thresholding procedure. The thresholding process consists of the user setting limits in the image's histogram such that the pixels corresponding only to the $Al_{19}Ni_5Y_3$ particles are selected and used in the measurement. However, if the limits set include pixels that actually do not belong to the particles, then the measured values will be inaccurate. In the case of measurements from images containing bright particles on a dark background, there will be an over estimation of the volume fraction. The electron beam has a Gaussian distribution and, when coupled with other blurring effects, this will cause the particles to appear larger than their true size. Thus, if the threshold limit does not exclude the proper pixels, then the measured value will be greater.

Another possible reason is that the assumptions made for the volume fraction calculation may not be completely valid. If the assumptions made, such as no solubility of Ni, Y and Co into Al, are not true; there will be some solubility. Therefore, the calculated value of volume fraction will contain errors due to these simplifications. A calculation based off of the phase diagram would not be any better because the phase

fields in the ternary phase diagrams for these types of alloys are not well known. Furthermore, it is not clear whether those diagrams are even valid for devitrified Al alloys. Those equilibrium phase diagrams are constructed using data from casting experiments, while the microstructures in the alloys in this study are produced from a devitrified amorphous state. It is important to note that all of the assumptions made will give a maximum value for the volume fraction of the $Al_{19}Ni_5Y_3$ phase. Any invalidity in those assumptions would actually give a lower estimated value for the volume fraction. As such, the observed discrepancy between the calculated and measured volume fractions must be associated with errors in the measured values.

5.2 **Forged Microstructure**

The initial hypothesis in this study was that since the major axes of the $Al_{19}Ni_5Y_3$ particles are of comparable sizes to the diameters of the Al grains, their high volume fraction, and the small inter-particle spacing would result in the fragmentation of the particles during forging, especially at the high upsets used for these materials. However, this is not the case because, as shown in section 4.2, similar values of $Al_{19}Ni_5Y_3$ particle size were measured for each of the different processing conditions. Thus, the particles are not breaking up into smaller fragments.

Instead, the SEM and TEM data shown in section 4.2 suggest that the particles were rotating during forging. However, such images give limited information because sectioning and projection effects distort the morphology of the particles, thereby complicating any interpretation of particle orientation. Therefore, serial-section FIB tomography was used to further analyze these materials because this technique is capable

of revealing the sub-surface microstructure that is not seen clearly in typical 2D images. The three-dimensional tomographic reconstructions (section 4.3) show very clearly that there is 90-degree rotation of the $Al_{19}Ni_5Y_3$ particles from the as-extruded to the 84% upset forged materials.

It is interesting to note that there was no measureable rotation of the $Al_{19}Ni_5Y_3$ particles in the 43% upset forged material. This was noted in both SEM and TEM images and is clearly observed in the tomographic reconstruction, which shows that there is no significant change to the particle orientation (whereas significant rotation is observed in the subsequent forgings). If the particles were inclined to the stress axis, then during forging the particles would experience a torque, which would tend to cause them to rotate. However, it is clear from the tomographic experiments that the particles are well aligned with the extrusion direction. As such, when the material is forged the magnitude of this torque will be very small due to the orientation of the particles, and the softer Al matrix will simply flow plastically around the particles. This situation will persist until the particle orientation is perturbed due to end effects and/or particle/particle interactions. Once the particles are inclined to the forging stress axis, they will tend to rotate under the applied net torque until they lie perpendicular to the forging axis. The most remarkable feature of the observations presented here is that no significant rotation was observed after an upset of 43%. This represents a very high plastic strain without particle rotation and is an artifact of the degree of particle alignment in the extrudate and the choice of forging axis.

Mechanical properties – In a separate study on these materials Pratt and Whitney conducted a set of tensile tests to measure the mechanical properties of the alloys. Standard tensile specimens with a 2 inch gage length and 1/8 inch gage diameter were machined from the materials and tested to determine the 0.2% off-set yield strength (ksi) and the elongation to fracture. The values obtained are plotted against the percentage upset in Figure 5.1. It is important to note that the data points for the as-extruded (0% upset forged) material in Figure 5.1 were obtained at a different specimen orientation from the other points; the tensile samples were machined from the as-extruded material so that the tensile axis was parallel to the extrusion direction. On the other hand, the tensile specimens for the 43%, 64% and 84% upset forged materials were machined so that the tensile axis was perpendicular to the extrusion direction. The yield strength data in Figure 5.1 exhibit an initial decrease from 98.0 ksi for the as-extruded alloy to 87.0 ksi for the 43% upset forged material. For higher forging upsets the trend appears to reverse with values of 99.0 ksi and 103.5 ksi for the 64% and 84% upset forged material, respectively. To obtain a more valid comparison between the as-extruded and the upset-forged materials, additional tensile samples were machined from the as-extruded material with the tensile axis perpendicular to the extrusion direction. There was a large spread in the data obtained from these latter samples, all of which exhibited very brittle failure. As such, only fracture stresses and fracture strains could be reported: the mean values (plus or minus 1 standard deviation) were 75.6 ± 11.0 ksi and 0.00616 ± 0.00114 %, respectively.

Since the volume fraction of the $Al_{19}Ni_5Y_3$ plates is so high and the sizes of these plates are similar to the dimensions of the Al grains, they can be described more

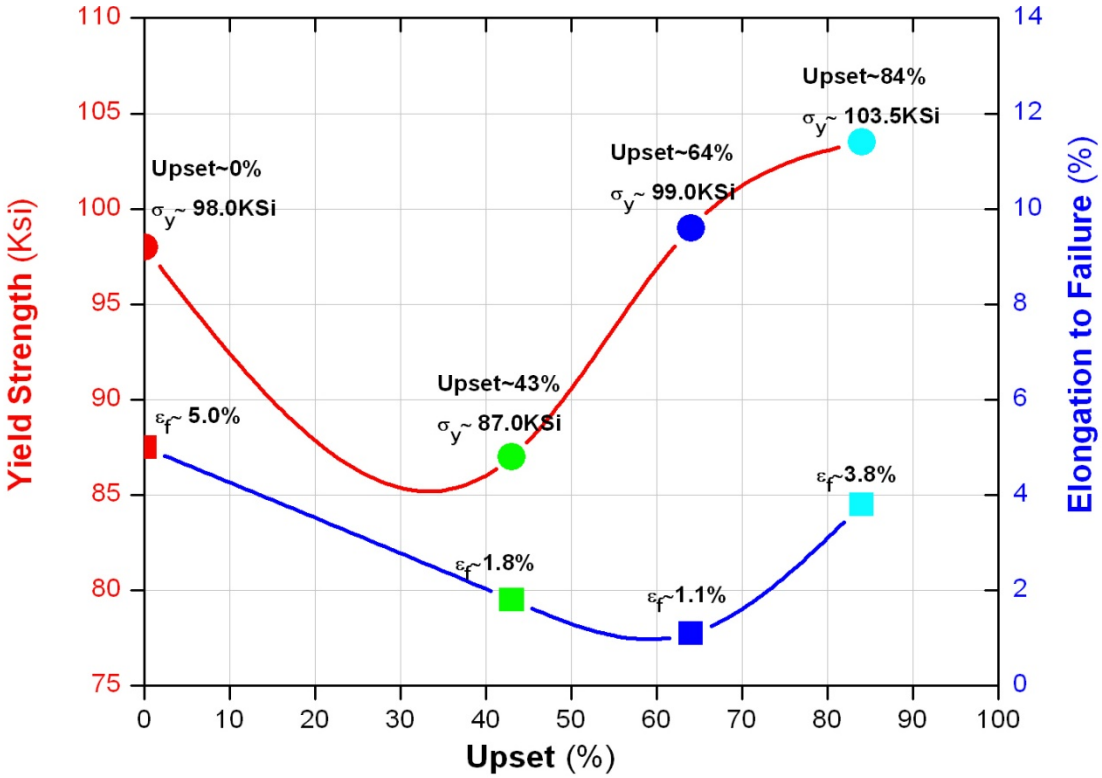

Figure 5.1: Values of yield strength (ksi) and elongation to failure (%) plotted against the percentage of upset. These data points were obtained from tensile tests. It is important to note that the data points for the as-extruded material were obtained at a different specimen orientation from the other points. Tensile specimens for the as-extruded material were machined such that the tensile axis was parallel to the extrusion direction, whereas the upset forged materials had their specimens orientated with the tensile axis perpendicular to the extrusion direction.

appropriately as metal-matrix composites than as precipitation-hardened alloys when considering the mechanical properties that they exhibit. Thus, the alloys behave as fiber-reinforced composite materials, in which the soft Al matrix is reinforced by the hard $Al_{19}Ni_5Y_3$ plates. Fiber-reinforced composites exhibit optimal properties when the fibers are aligned and the loading axis is parallel to the major axis of the reinforcing fibers: this occurs because the load is shared effectively between the two phases. However, strengths of aligned fiber-reinforced composites are severely compromised when the materials are loaded perpendicular to the major axis of the fibers. The main reason for this is that the load is no longer shared between the two phases; instead the matrix bears the entire load. Furthermore, there are stress concentrations at the fiber/matrix interfaces along the loading direction. Isolated microcracking can occur at these locations, and number of these microcracks will increase with loading until they coalesce causing a catastrophic failure. Also, in-plane shear stresses cause high shear stress concentrations at the fiber/matrix interfaces, which can lead to shear failure in the matrix. These types of mechanical behaviors are observed in the materials in this study. The as-extruded material exhibited brittle failure when it was tested perpendicular to the extrusion direction (i.e. when the loading axis was perpendicular to the major axis of the $Al_{19}Ni_5Y_3$ particles). However, when the as-extruded material was tested parallel to the extrusion direction (i.e. when the loading axis is parallel to the major axis of the $Al_{19}Ni_5Y_3$ particles), higher values of both strength and ductility were obtained. In the 43% upset forged material, the $Al_{19}Ni_5Y_3$ particles are still aligned with the extrusion direction, so it might be expected to exhibit similar properties to the as-extruded material tested in the same orientation. However, the 43% upset forged material exhibited a higher strength,

which is probably caused by work hardening of the Al phase during plastic deformation. It also exhibited much more ductility (1.8% compared to 0.00616%), but this is still lower than the value for the as-extruded material tested parallel to the $Al_{19}Ni_5Y_3$ particles. This lower ductility is probably caused by micro-void formation, as expected in a ductile matrix composite loaded perpendicular to the major axis of the fibers. The 64% upset forged material exhibits a higher strength, presumably due to further work hardening, and a lower elongation to failure than the 43% upset forged alloy. For components loaded in uniaxial tension, there will be a maximum shear stress at 45° to the loading axis. Since the $Al_{19}Ni_5Y_3$ particles in the 64% upset forged material are inclined to the loading axis, they would experience shear stress concentrations along the particle/matrix interfaces. Thus, the combined effects increased work hardening and this stress concentration could explain the overall reduction in ductility. Finally, the 84% upset forged material exhibits both an increase in strength and ductility. In this material, the $Al_{19}Ni_5Y_3$ particles are aligned with the loading axis, which is the ideal configuration for strength and ductility. Hence, this preferred alignment coupled with work hardening gives the highest strength value among all the test specimens and the highest elongation to failure among the forged materials [40].

5.3 **FIB Tomography**

The FIB tomography technique has proven to be very useful in the analysis of these materials. After processing of the data acquired during serial sectioning experiments, three-dimensional representations of the $Al_{19}Ni_5Y_3$ phase were constructed, which revealed details of the particles that could only be inferred from 2D SEM and

TEM images. However, as discussed in the previous chapter, there are many challenges associated with this characterization technique including instrumental complications due to drift in the beams and the stage during serial sectioning. Thus, the limiting factor is the amount of time necessary to run these types of experiments. The main steps in a serial-section FIB tomography experiment are:

1) Preparation of specimens, e.g. sectioning, mounting and polishing.
2) Preparation of region of interest, such as milling of trenches, and cleaning of pier.
3) Setting up and running serial sectioning routine.
4) Processing of image stacks, such as alignment, cropping, and image enhancement.
5) Segmentation of appropriate features in microstructures.

Many of these steps are trivial, but the challenge is the time needed to perform them. The preparation of the volume of interest (Step 2) can take an experienced user several hours to finish. The serial sectioning routine (Step 3) for this study took up to 8 hours to perform for each data set acquired, but the instrument was equipped with an automatic sectioning routine and (in theory) could be left to run overnight. The problem was that any complications (such as those mentioned) would severely prolong the total experiment time, and in the worst-case scenario, could force the user to start all over again. This occurred several times in the present work. Once an image stack is acquired, the processing and segmentation (Steps 4 & 5) can take up to several days to complete.

There is an inherent limitation in the analysis of particle morphology and orientation using two-dimensional images acquired from sectioned specimens. As shown

in this study, the orientation of the $Al_{19}Ni_5Y_3$ phase could only be inferred from SEM and TEM images. Therefore, this system was an appropriate candidate for FIB tomography, and the three-dimensional reconstructions clearly reveal that these kinds of analyses can really benefit from this technique. However, the basic steps for tomographic experiments require a substantial amount of time, and any complications will further prolong the experiments. Thus, FIB tomography will not become a routine characterization technique and will instead be limited to a few select studies of materials in which a true 3D representation of the microstructure is necessary to develop an understanding of the material properties.

Chapter 6: Conclusions

Chapter 6: Conclusions

The objective of this thesis was to investigate the microstructural changes that occurred after an extruded Al-Ni-Y-Co alloy was subjected to three forging upsets: 43%, 64% and 84%. A variety of different characterization tools were used to examine these materials, including: XRD, SEM, and TEM. Data obtained using these techniques revealed the phases present and their compositions, volume fractions, sizes and morphologies. A more complete understanding of the microstructural changes occurring after processing was accomplished through the use of FIB based tomography, which provided the means to build three-dimensional reconstructions of the microstructures. Based on the results from these techniques, the following conclusions have been drawn:

1. The microstructures in these alloys consisted of a FCC Al matrix surrounding a high volume fraction of elongated $Al_{19}Ni_5Y_3$ plates. No binary phase was observed.

2. In the initial as-extruded microstructure all of the $Al_{19}Ni_5Y_3$ plates are aligned with their major axes parallel to the extrusion direction.

3. The $Al_{19}Ni_5Y_3$ plates do not break up into smaller fragments during forging since the sizes of the plates are almost identical in all of the materials.

4. There is significant rotation of the $Al_{19}Ni_5Y_3$ plates during forging such that they lie approximately perpendicular to the forging axis after the 84% upset.

5. A substantial amount of deformation can be accommodated in these materials without any measureable changes to the $Al_{19}Ni_5Y_3$ particle orientation. However, this is probably an artifact caused by the particles being so well aligned with the extrusion direction in the initial microstructure.

6. The variation in the mechanical properties of these alloys with the plate orientation is consistent with what one would expect for a short fiber-reinforced metal matrix composite.

7. FIB tomography is a very powerful tool for the characterization of complex microstructures. However, there are many challenges are associated with this technique. Therefore, the use of FIB tomography will be limited only to appropriate material systems that can truly benefit from a three-dimensional representation of their microstructures.

References

1. Willey LA. U.S. Patent No. 3.619.181. November 9, 1971.
2. Norman AF, Prangnell PB, McEwen RS. *Acta mater*. **46** (1998) 5715-5732.
3. Royset J, and Ryum N. *International Materials Reviews* **50** (2005) 19-44.
4. Marquis EA, and Seidman DN. *Acta mater.* **49** (2001) 1909-1919.
5. Zakharov VV. *Metal Science and Heat Treatment* **45** (2003) 246-253.
6. Seidman DN, Marquis EA, Dunand DC. *Acta mater*. **50** (2002) 4021-4035.
7. Novotny GM, and Ardell AJ. *Materials Science and Engineering* **A318** (2001) 144-154.
8. Watanabe C, Kondo T, Monzen R. *Metallurgical and Materials Transactions A* **35** (2004) 3003-3008.
9. Ocenasek V, and Slamova M. *Materials Characterization* **47** (2001) 157– 162.
10. Vetrano, JS, Bruemmer SM, Pawlowski LM, Robertson, IM. *Materials Science and Engineering* **A238** (1997) 101- 107.
11. Blake N, and Hopkins MA. *Journal of Materials Science* **20** (1985) 2861–2867.
12. Parker BA, Zhou ZF, Nolle P. *Journal of Materials Science* (1993) 452-458.
13. Fuller, CB, Seidman DN, Dunand DC. *Acta Materialia* **51** (2003) 4803–4814.
14. Fuller, CB, Krause AR, Dunand DC, and Seidman DN. *Materials Science and Engineering* **A338** (2002) 8-16.
15. Singh V, Prasad KS, Gokhale AA. *Journal of Materials Science* **39** (2004) 2861–2864.
16. Yu K, Li W, Li S, Zhao J. *Materials Science and Engineering* **A368** (2004) 88–93.

17. Inoue A, Ohtera K, Tsai A, Masumoto T. *Japanese Journal of Applied Physics* **27** (1988) L479-L482.

18. Inoue A, and Kimura H. *Materials Science and Engineering* **A286** (2000) 1–10.

19. Inoue A, and Kimura H. *Current Opinion in Solid State & Materials Science* **2** (1997) 305-310.

20. Rizzi P, and Battezzati L. *Journal of Non-Crystalline Solids* **344** (2004) 94–100.

21. Choi GS et al. *Scripta Metallurgica et Materialia* **33** (1995) 1301-1306.

22. Greer AL. *Materials Science and Engineering* **A304–306** (2001) 68–72.

23. Kim HS, and Hong SI. *Acta mater*. **47** (1999) 2059 – 2066.

24. Inoue A, Horio Y, Kim YH, Masumoto T. *Materials Transactions JIM* **33** (1992) 669-674.

25. Inoue A. *Acta mater.* **48** (2000) 279-306.

26. Yao N. *Focused Ion Beam Systems*. Cambridge University Press. New York, New York, 2007.

27. Chen HS. *Journal of Chinese Physics* **28** (1990) 407-425.

28. Kalpakjian S, and Schmid S. *Manufacturing Processes for Engineering Materials.* Pearson Education, Inc. Upper Saddle River, New Jersey, 2003.

29. German RM. *Powder Metallurgy Science.* Metal Powder Industry Federation. Princeton, New Jersey, 1994.

30. Vasiliev AL et al. *Intermetallics* **12** (2004) 349-362.

31. Vasiliev AL et al. *Intermetallics* **13** (2005) 741–748.

32. Magdefrau NJ et al. *Scripta Materialia* **51** (2004) 485–489.

33. Vasiliev AL et al. *Scripta Materialia* **52** (2005) 699–704.

34. Rykhal RM, Zarechnyuk *OS Dopov Acad Nauk Ukr SSR* **A4** (1977) 375.

35. Latuch J, Matyja H, Fadeeva VI. *Materials Science and Engineering* **A179-180** (1994) 506.

36. Latuch J, Zielinski W, Matyja H. *J Appl Cryst* **17 (**1998) 152.

37. Kulik T, Latuch J. *J Metastable Nanocryst Mat* **10 (**2001) 194.

38. Raggio R, Borzone G, Ferro R. *Intermetallics* **8** (2000) 247-257.

39. Pictures taken from the Crystal Lattice Structures Web page, http://cst-www.nrl.navy.mil/lattice/, provided by the Center for Computational Materials Science of the United States Naval Research Laboratory.

40. Daniel IM, and Ishai O. *Engineering Mechanics of Composite Materials*. Oxford University Press. New York, New York, 2006.